Seismic reflection data reveal the 3D subsurface structure of pit craters

Craig Magee[1], Corbin L. Kling[2], Paul K. Byrne[3], and Christopher Jackson[4]

[1]University of Leeds
[2]Smithsonian Institution
[3]Washington University in St. Louis
[4]University of Manchester

November 22, 2022

Abstract

Pit craters are enigmatic, quasi-circular depressions observed on rocky (e.g., Earth and Mars) and icy (e.g., Enceladus) planetary bodies, and numerous asteroids. These depressions are not related to meteorite impacts. Instead pit craters are thought to be generated by overburden collapse into a subsurface cavity (e.g., created by dilatational faulting), or volumetrically depleted zone (e.g., an evacuated magma reservoir or conduit). The surface size and distribution of pit craters should thus provide an important record of otherwise inaccessible subsurface processes. Because we cannot access the subsurface structure of pit craters observed on planetary surfaces, we rely on physical and numerical models to infer the subsurface processes linked to their formation. Here, we use 3D seismic reflection data to quantify the palaeosurface and subsurface geometry of pit craters. These data enable us to identify whether pit craters connect to and their formation thus related to underlying structures. We map 59, Late Jurassic pit craters deeply buried within a sedimentary basin, offshore NW Australia. We demonstrate that some pit craters extend down and appear physically connected to igneous dykes, whereas others connect to dyke-induced and tectonic faults, seemingly where faults are steeply dipping and dilatational. There are no apparent relationships between pit crater geometries (e.g., palaeosurface expression or vertical extent) and the different magmatic and fault-related mechanisms we infer drove their formation. Reflection seismology is a powerful tool for understanding how pit craters form and whether their surface expression can be used to reconstruct subsurface structures and processes on other planetary bodies.

Seismic reflection data reveal the 3D subsurface structure of pit craters

Craig Magee[1], Corbin Kling[2], Paul Byrne[3], Christopher A-L Jackson[4]

[1]School of Earth Science and Environment, University of Leeds, Leeds, LS2 9JT, UK

[2]Center for Earth and Planetary Studies, Smithsonian Institution, Washington, D.C., 20560, USA

[3]Washington University in St. Louis, St. Louis, MO 63132, USA

[4]Department of Earth and Environmental Sciences, University of Manchester, Williamson Building, Oxford Road, Manchester, M13 9PL, UK

Key points

- We image and quantify the palaeosurface and subsurface 3D geometry of pit craters formed in the Late Jurassic
- Pit craters physically connected to upper tips of igneous dykes or steeply dipping, dilatational portions of normal faults
- No apparent relationship between pit crater geometry and formation mechanism

Abstract

Pit craters are enigmatic, quasi-circular depressions observed on rocky (e.g., Earth and Mars) and icy (e.g., Enceladus) planetary bodies, and numerous asteroids. These depressions are not related to meteorite impacts. Instead pit craters are thought to be generated by overburden collapse into a subsurface cavity (e.g., created by dilatational faulting), or volumetrically depleted zone (e.g., an evacuated magma reservoir or conduit). The surface size and distribution of pit craters should thus provide an important record of otherwise inaccessible subsurface processes. Because we cannot access the subsurface structure of pit craters observed on planetary surfaces, we rely on physical and numerical models to infer the subsurface processes linked to their formation. Here, we use 3D seismic reflection data to quantify the palaeosurface and subsurface geometry of pit craters. These data enable us to identify whether pit craters connect to and their formation thus related to underlying structures. We map 59, Late Jurassic pit craters deeply buried within a sedimentary basin, offshore NW Australia. We demonstrate that some pit craters extend down and appear physically connected to igneous dykes, whereas others connect to dyke-induced and tectonic faults, seemingly where faults are steeply dipping and dilatational. There are no apparent relationships between pit crater geometries (e.g., palaeosurface expression or vertical extent) and the different magmatic and fault-related mechanisms we infer drove their formation. Reflection seismology is a powerful tool for understanding how pit craters form and whether their surface expression can be used to reconstruct subsurface structures and processes on other planetary bodies.

Plain language summary

Linear chains of small craters are commonly observed on planetary bodies like Mars, Enceladus, or various asteroids. These craters, called pit craters, are not related to meteorite impacts. Based on comparison to similar craters observed on Earth and created in laboratory models, we think pit craters form because rock collapses into holes present beneath the surface. There are many suggestions for how these holes form, but all suggest their presence destabilises overlying rock, which drains into the hole and leaves a crater at the surface. We have not been able to test suggestions about how these holes form, because we cannot easily look beneath the surface of other planetary bodies. We use a technique called seismic reflection, which uses sound waves to create an ultrasound-like image of Earth's subsurface. With this technique, we image the 3D shape of pit craters found offshore Australia. These data allow us for the first time to measure what pit craters look like in the subsurface and see whether they link to any structures that could have caused their formation. We show that some pit craters are connected to igneous dykes (solidified vertical sheets of molten rock) and others to faults (cracks in the rock).

Introduction

Quasi-circular topographic depressions are observed on the surface of Earth and many planetary bodies and asteroids (e.g., Figs 1A and B) (e.g., Abelson et al., 2003; Ferrill et al., 2004; Ferrill et al., 2011; Frumkin & Naor, 2019; Horstman & Melosh, 1989; Kling et al., 2021; Martin et al., 2017; Okubo & Martel, 1998; Sauro et al., 2020; Scott & Wilson, 2002; Whitten & Martin, 2019; Wyrick et al., 2004). These depressions, termed 'pit craters', have diameters of meters to thousands of meters and commonly arranged in linear chains (e.g., Kling et al., 2021; Whitten & Martin, 2019). The lack of raised rims and ejecta deposits around pit craters suggest they are not formed by meteorite impacts (e.g., Figs 1A and B) (e.g., Halliday, 1998; Poppe et al., 2015; Wyrick et al., 2004). Instead, pit craters are thought to reflect collapse of overlying rock and/or regolith into subsurface cavities or volumetrically depleted zones generated by (Fig. 1C) (see also Wyrick et al., 2004): (i) the dissolution of carbonate or salt (e.g., sinkholes; Abelson et al., 2003; Poppe et al., 2015; Spencer & Fanale, 1990); (ii) local porosity reduction of the host material following hydrothermal fluid flow or fault-related overpressure release (e.g., pockmarks; Velayatham et al., 2019; Velayatham et al., 2018); (iii) evacuation of lava tubes (see Sauro et al., 2020 and references therein); (iv) opening of tensile fractures (e.g., Ferrill et al., 2011; Smart et al., 2011; Tanaka & Golombek, 1989); (v) local dilation where faults are steeply dipping (e.g., Ferrill & Morris, 2003; Ferrill et al., 2011; Ketterman et al., 2015; Kettermann et al., 2019; Smart et al., 2011; Von Hagke et al., 2019); (vi) dyke intrusion (e.g., Mège & Masson, 1996; Okubo & Martel, 1998; Scott & Wilson, 2002; Wall et al., 2010); (vii) magma migration out of a reservoir (e.g., Mège

et al., 2003; Poppe et al., 2015); and/or (viii) explosive volcanism (e.g., Hughes et al., 2018).

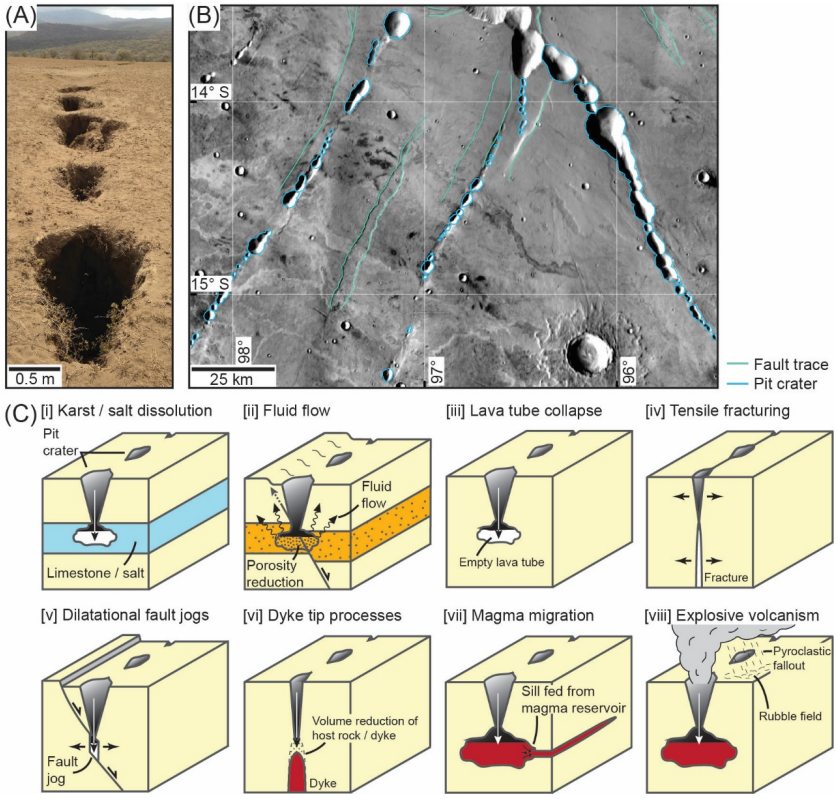

Figure 1: (A) A pit crater chain in the Natron Basin, Tanzania (Magee et al., 2019; Muirhead et al., 2015). (B) Pit crater chains and graben-bounding fault traces in the Noctis Labyrinthus area of Mars (Kling et al., 2021). Basemap is THEMIS Daytime-IR. (C) Conceptual models of pit crater formation (modified from Kettermann et al., 2019; Sauro et al., 2020; Velayatham et al., 2019; Velayatham et al., 2018; Wyrick et al., 2004).

If the surface expression of pit craters reflects their formation mechanism(s), we could use their morphology to interrogate inaccessible subsurface processes and structures on Earth, as well as other planetary bodies and asteroids (e.g., Kling et al., 2021; Korteniemi et al., 2010; Martin et al., 2017; Mège & Masson, 1997; Smart et al., 2011; Whitten & Martin, 2019). However, imaging pit craters on other worlds is difficult (Wyrick et al., 2004), and even our knowledge of the subsurface geometry of pit craters on Earth remains limited (cf. Abelson et al., 2003; Frumkin & Naor, 2019; Halliday, 1998; Wall et al., 2010). We thus rely on physical experiments and numerical modelling to predict how pit crater formation may translate into surface deformation (e.g., Poppe et al., 2015; Smart et al., 2011). Identifying pit craters on Earth, the subsurface structure of which we *can* study, is crucial to validating these models and thus determining whether pit crater surface expressions can be used to distinguish formation mechanisms.

Reflection seismology provides unprecedented insight into Earth's subsurface and can uniquely image the three-dimensional structure of pit craters (Abelson et al., 2003; Magee et al., 2019; Magee & Jackson, 2020a; Wall et al., 2010). Here, we use seismic reflection data imaging a sedimentary basin on the Exmouth Plateau, offshore NW Australia to conduct the first-ever quantitative, 3D analysis of pit craters and their underlying structure. Seismic-stratigraphic analyses reveal the now-buried pit craters developed during a phase of Late Jurassic igneous dyking (Magee & Jackson, 2020a). Our data allow us to: (i) quantify the palaeosurface expression and subsurface structure of pit craters in 3D; and (ii) identify underlying structures that may

be related to pit crater formation. Overall, we can thus test whether the (palaeo)surface expression of pit craters are diagnostic of subsurface structure and processes.

We map 59 pit craters, which typically have a funnel-like appearance comprising an upper inverted cone that is underlain by a pipe, and are commonly arranged in linear chains. Most (54) pit craters occur in chains located along the floor of [?]2 km wide, buried graben that are bound by dyke-induced faults and underlain by what were northwards-propagating dykes (Magee & Jackson, 2020a); five other pit craters are connect to steeply dipping portions of tectonic normal faults. The link between pit craters and dykes and faults confirms that magmatic processes and overburden collapse into dilatational fault jogs. By recognising that some pit craters above dykes occur at different stratigraphic levels and broadly get younger southwards, we specifically suggest these pit craters may have formed when a waning of magma pressure and potential backflow led to a local volume reduction of the dyke. In addition to obtaining insight into pit crater formation mechanisms, we also show that pit crater depths are variable across the study area. Pit crater depth are one of the few morphological properties of pit craters that can be measured from surficial data, and have been suggested to equal and thus be a proxy for regolith thickness on other planetary bodies (e.g., Whitten & Martin, 2019; Wyrick et al., 2004). The variability in pit crater depths we record suggest this characteristic may *not* always control regolith thickness. Overall, our work demonstrates that seismic reflection data provides a unique insight into the structure and growth of pit craters on Earth. Further seismic-based studies will help us understand extraterrestrial pit craters and, thus, probe the subsurface structure and composition of other planetary bodies for which direct, in situ data are not yet available.

Geological setting

The North Carnarvon Basin, offshore NW Australia (Fig. 2A) formed during periodic rifting between Australia and Greater India in the Late Carboniferous-to-Early Cretaceous (e.g., Direen et al., 2008; Longley et al., 2002; Stagg et al., 2004). The Exmouth Plateau, where the studied pit craters are situated, lies within the North Carnarvon Basin and itself began in the Rhaetian (Late Triassic) to Callovian (Middle Jurassic) rift phase, which produced an array of ˜N-striking, large-throw (up to ˜1 km) normal faults (Figs 2B and C) (e.g., Bilal et al., 2018; Black et al., 2017; Gartrell et al., 2016; Marshall & Lang, 2013; Stagg & Colwell, 1994; Tindale et al., 1998). These tectonic faults displace a thick pre-rift succession, including the fluvio-deltaic Mungaroo Formation, and accommodated deposition of a relatively condensed ([?]100 m thick), clastic-dominated, syn-rift succession (i.e. the Brigadier and North Rankin formations, the Murat Siltstone, and the Athol Formation; Figs 2B and C) (Hocking, 1992; Hocking et al., 1987; Stagg et al., 2004; Tindale et al., 1998).

The Callovian unconformity caps the Athol Formation and underlies the Oxfordian-to-Tithonian, marine Dingo Claystone, marking the end of major Late Triassic-to-Middle Jurassic rifting (Figs 2B and C) (e.g., Tindale et al., 1998; Yang & Elders, 2016). Renewed rifting in the Tithonian (Late Jurassic) to Valanginian (Early Cretaceous) involved (Figs 2B and C): (i) sub-aerial development of the regionally developed, Base Cretaceous unconformity at ˜148 Ma (latest Tithonian); (ii) rapid and significant subsidence to accommodate deposition of the [?]3 km thick, fully marine Barrow Group; and (iii) relatively limited upper crustal faulting, which was restricted to minor reactivation of older faults and generation of an array of N-S to NE-SW striking, low-throw (<0.1 km) normal faults (e.g., Driscoll & Karner, 1998; Magee et al., 2016; Paumard et al., 2018; Reeve et al., 2016). Continental break-up occurred along the western and southern margin of the Exmouth Plateau in the Valanginian-to-Hauterivian (˜135–130 Ma; Fig. 2B) (e.g., Direen et al., 2008; Reeve et al., 2021; Robb et al., 2005). Following break-up, thermal subsidence accommodated deposition of a thick post-rift succession that hosts several tiers of polygonal faults (e.g., Paganoni et al., 2019; Velayatham et al., 2019).

During the Late Jurassic, at ˜148 Ma, a radial dyke swarm, up to ˜170–500 km long and ˜300 km wide, was emplaced across much of the Exmouth Plateau (Figs 2A and B) (Magee & Jackson, 2020a). Associated with this dyke swarm is an array of dyke-induced faults that extend up from and dip towards the upper tips of dykes, offsetting Late Triassic-to-Late Jurassic strata and bounding dyke-parallel graben (e.g., Figs 2D and 3A) (Magee & Jackson, 2020a; Magee & Jackson, 2020b). Within these graben, linear chains of sub-

circular depressions are recognised (e.g., Figs 2D and 3A) (Magee & Jackson, 2020a; Velayatham et al., 2019; Velayatham et al., 2018). These depressions, which are interpreted to have formed at the contemporaneous free surface, are underlain by pipe-like features that extend down towards dykes, dyke-induced normal faults, or tectonic normal faults (e.g., Figs 2D and 3A) (Magee & Jackson, 2020a; Velayatham et al., 2019; Velayatham et al., 2018). The depressions have previously been interpreted as pockmarks formed by fluid escape from an overpressured horizon when faulting locally reduced the overburden pressure (e.g., Fig. 1B [ii]) (Velayatham et al., 2018). However, the spatial and temporal association between the depressions and underlying dykes suggests they may be analogous to pit craters observed elsewhere on Earth and other planetary bodies (Magee & Jackson, 2020a); henceforth we refer to these depressions as 'pit craters'.

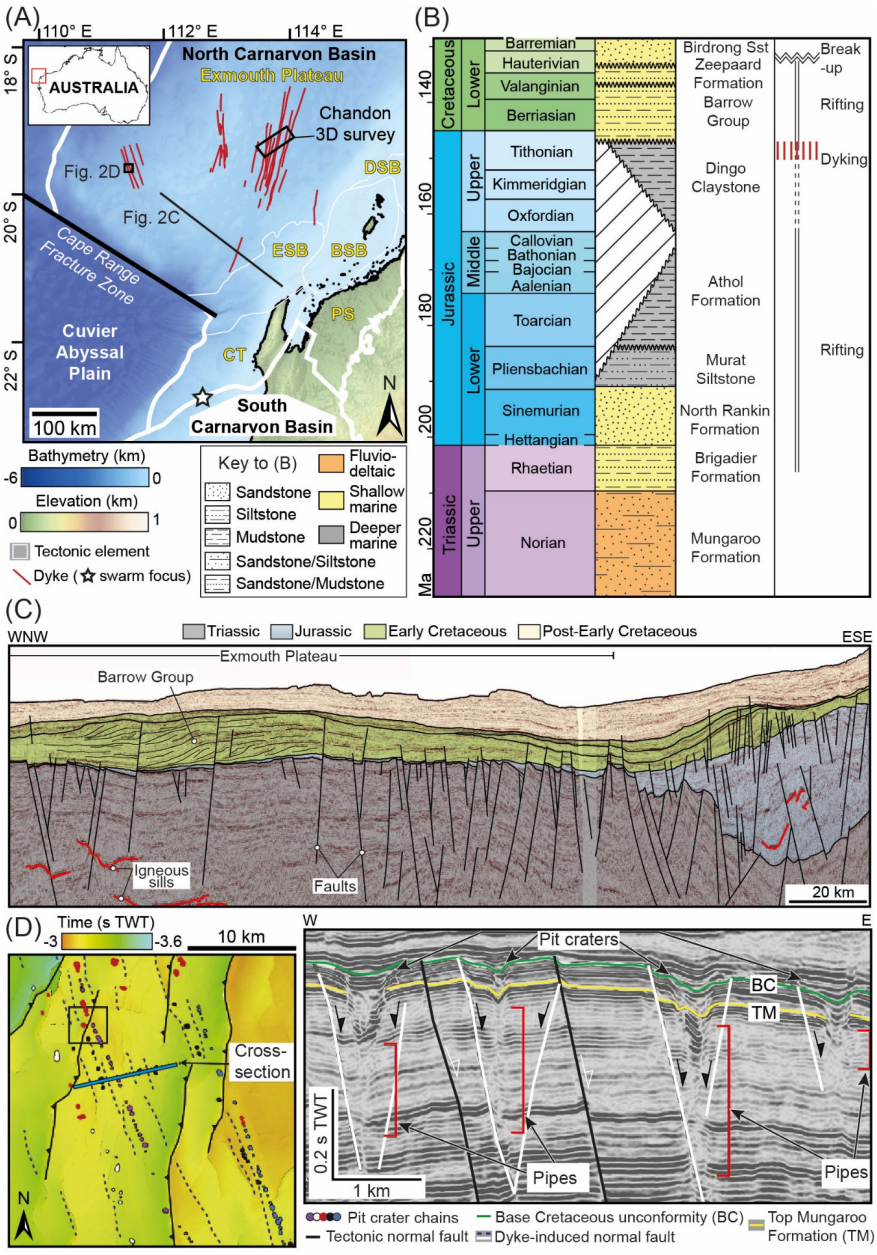

Figure 2: (A) Map of the southern portion of the North Carnarvon Basin highlighting principal tectonic elements, including the: ESB = Exmouth Sub-basin, CT = Carnarvon Terrace, BSB = Barrow Sub-basin, DSB = Dampier Sub-basin, and PS = Peedamullah Shelf. The location of the Exmouth Dyke Swarm is also shown (Magee & Jackson, 2020a). Elevation data are based on the 2009 Australian Bathymetry and Topography grid (Geoscience Australia). Inset: Location map of the North Carnarvon Basin (NCB) relative to Australia. (B) Stratigraphic column for the Exmouth Plateau summarising the age, dominant lithology, and generalised depositional environment for key units (after Hocking et al., 1987; Partington et al., 2003; Tindale et al., 1998). Key tectonics and magmatic events are also shown for (see Reeve et al., 2021 and references therein). (C) Interpreted seismic section, showing generalised stratigraphic architecture of the Exmouth Plateau and Exmouth Sub-basin (modified from Reeve et al., 2016). See Figure 2A for location. (D) Interpreted time-structure map and seismic section showing pit crater-like features arranged in chains and associated with normal faults in the western portion of the Exmouth Plateau (modified from Velayatham et al., 2018). See Figure 2A for map location.

Dataset and Methods

The zero-phase, time-migrated Chandon 3D seismic reflection survey covers an area of ˜951 km^2, has a bin spacing of 25 m, and a record length of 6 seconds two-way time (s TWT). We present seismic images where a trough (black) reflection has a positive polarity and corresponds to a downward increase in acoustic impedance, and a peak (white) reflection has a negative polarity and represents a downward decrease in acoustic impedance (e.g., Fig. 3A). To help identify and map the pit craters, their underlying dykes, and spatially associated faults, we extract a variance volume attribute; this accentuates spatial variations in waveform similarity (e.g., Chopra & Marfurt, 2005; Marfurt & Alves, 2015).

We use data from five boreholes (Chandon-1, Chandon-2, Chandon-3, Mercury-1, and Yellowglen-1) within the survey area to establish estimates for: (i) the age and intervening lithology of three mapped stratigraphic horizons, which correspond to the Top Mungaroo Formation (TM; ˜209 Ma), Top Athol Formation (TA; ˜164 Ma), and Base Cretaceous unconformity (BC; ˜148 Ma); (ii) an average time-depth relationship for the subsurface (see Supporting Figure 1), allowing us to depth-convert (from ms TWT to metres) measurements taken from the top 4 s TWT of the survey; and (iii) the seismic velocity (v) range of the interval of interest within which the pit craters are imaged. Seismic velocity increases with depth, from 2.64(±10%) km s^{-1} to 3.66(±10%) km s^{-1}, as the dominant frequency (f) of the data broadly decreases from ˜33 Hz to ˜23 Hz; with these data we calculate the wavelength ($\lambda = v / f$) of the data and estimate that its vertical seismic resolution can be characterised by limits of separability ($\lambda/4$) of 37(±7)–17(±3) m and limits of visibility ($\lambda/30$) of 5(±1)–3(±1) m (e.g., Brown, 2011). The limits of separability and visibility correspond to the minimum vertical distance between two features required for them to be imaged, respectively, as: (i) two discrete reflections; and (ii) a tuned reflection package, created by convolution of the two reflections on their return to the surface (Brown, 2011). The horizontal resolution of the time-migrated seismic reflection data is estimated to be at least 25 m, which is equivalent to the bin spacing, and likely increases to 37(±7) m (i.e. $\lambda/4$) with depth.

Plan-view measurements

We identify 59 pit craters that we label An –In if they overlie a dyke, with A–I corresponding to the dyke name (Magee & Jackson, 2020a; Magee & Jackson, 2020b), or Xn if they appear spatially related to tectonic normal faults; n denotes the pit crater number, which increases along each chain from south to north. We map the plan-view outline of each pit crater at: (i) their uppermost expression in the seismic reflection data; and (ii) where they intersect the Top Athol Formation; this allows us to characterise how pit crater plan-view morphology changes with depth. For each mapped pit crater outline, we use image analysis software (ImageJ) to define a best-fit ellipse and centroid position; where pit craters appear to have merged, we define an encompassing best-fit ellipse but manually determine centroid positions (Fig. 3B). We use the outline of each pit crater, or merged pit craters, to measure their area and the best-fit ellipses to determine their long axis lengths and azimuths, and short axis lengths (Fig. 3B). From these values, we calculate the aspect ratio of the pit crater long and short axes.

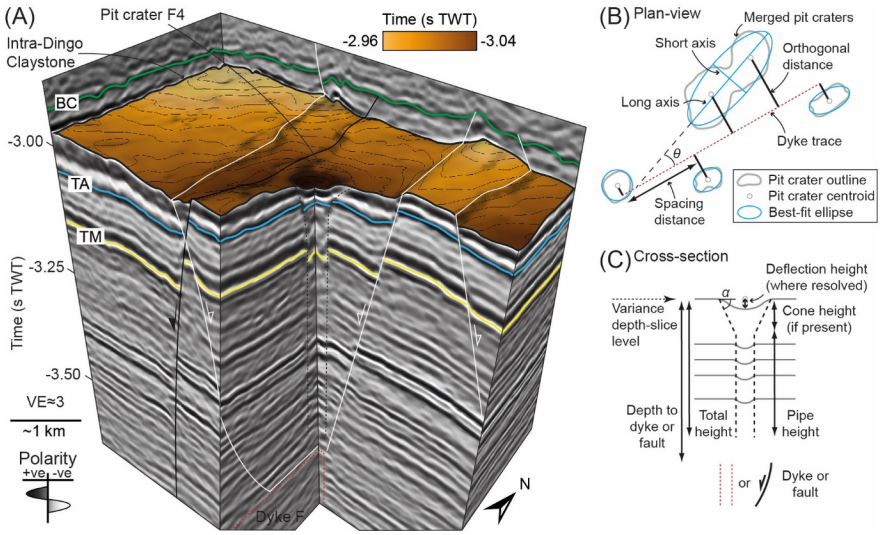

Figure 3: (A) 3D view of a funnel-like pit crater (F4), the top of which occurs at a horizon between the Base Cretaceous unconformity (BC) and Top Athol Formation (TA) (Magee & Jackson, 2020a). The pit crater occurs with a graben and extends down to the top of Dyke F, below the Top Mungaroo Formation (TM). (B and C) Schematics showing the measurements of pit crater plan-view (B) and cross-sectional (C) morphologies.

Cross-section measurements

The only cross-section attributes commonly available to measure for most pit craters on Earth and other planetary bodies are the depth and slope; together these can be used to estimate volume, of their surface expression (e.g., Gwinner et al., 2012; Sauro et al., 2020; Scott & Wilson, 2002; Wyrick et al., 2004). Most (54; i.e. 92%) pit craters we study display a funnel-like morphology, comprising an upper, inwardly inclined conical surface, which we refer to as an 'inverted cone', underlain by a sub-vertical cylindrical 'pipe' (e.g., Fig. 3A). Some pit craters lack an inverted cone and we refer to their morphology as pipe-like. Stratigraphic reflections within many of the inverted cone sections appear continuous with in the flanking host rock, although they are often locally deflected downwards within the pit crater (e.g., Fig. 3C). Note that for some pit craters it is difficult to correlate internal and external stratigraphic reflections. Where possible, we measure both the maximum 'cone height' and 'deflection height' of pit craters (Fig. 3C). By integrating these measurements with those of pit crater long axis lengths, we estimate slopes and volumes of the inverted cone sections and deflected reflections, assuming they are axisymmetric (Fig. 3C) (Wyrick et al., 2004). We also measure 'pipe height', which for funnel-like pit craters we define as the vertical distance from the base of inverted cones down to where the pit crater structure is no longer seismically resolved (Fig. 3C). We calculate pipe volume from the pipe height and the pit crater long axis length as measured at the Top Athol Formation. To aid comparison between pit craters with and without a funnel-like morphology, we describe each as having a 'total height'; for pipe-like pit craters their total height is equal to pipe height, but for funnel-like pit craters their total height includes the cone height and pipe height (e.g., Fig. 3C). Our measured pipe and total heights are minimum estimates as a reduction in imaging with depth and the presence of other structures (e.g., faults), limits our ability to determine the true base of pit craters (Velayatham et al., 2019; Velayatham et al., 2018; Wall et al., 2010). We measure the depth of dykes or normal faults directly beneath the top of each pit crater (Fig. 3C).

Sources of error

The primary error source in our study relates to uncertainty in the seismic velocities used to depth-convert the seismic data from seconds two-way time to depth in metres. For example, our depth conversion assumes that

seismic velocities do not vary laterally across the study area. The similarity in the time-depth relationships for all four boreholes wells within the Chandon 3D survey supports our assumption that there is little lateral variation in seismic velocity (Supporting Fig. 1), but we conservatively consider that calculated velocities and measured dominant frequencies may vary by up to ±10% (Magee & Jackson, 2020a). Measurements of limits of separability and visibility, deflection height, cone height, pipe height, and the depth to underlying dykes thus have assumed depth conversion-related errors of ±10%. Manual mapping and measurement can introduce human errors (e.g., in defining pit crater pipe bases) that cannot be quantified; however, we consider that these errors may be up to ±5% (Magee & Jackson, 2020a). Overall, plan-view measurements are presented with ±5% errors as they do not require depth-conversion, but may be susceptible to human error. For measurements of pit height, cone height, pipe height, and the depth to underlying dykes, we estimate cumulative errors of ±15%; this based on the uncertainty in calculated seismic velocities and potential human errors.

Results

Stratigraphic and structural framework

Stratigraphic reflections within the interval of interest typically have a moderate amplitude and laterally continuous character (Fig. 4A). In places these reflections are: (i) offset by ˜N-striking, linear-to-curvilinear, moderate-to-high throw (up to ˜500 m) tectonic normal faults (e.g., Figs 4A-D); (ii) cross-cut by sub-vertical, ˜N-trending dykes (named A to I) that are expressed as >100 m wide zones of disrupted, low-amplitude reflections (Figs 4A and E); (iii) displaced by graben-bounding, low-throw ([?]0.1 km), dyke-induced normal faults that dip towards and converge upon the upper tips of the underlying dykes at depths of ˜3–3.5 km (Fig. 4A); or (iv) intersected by pit craters (see below) (Figs 3A and 4A). Below the Base Cretaceous unconformity, pit craters and dykes are marked by high variance, as are areas where strata are folded and/or offset by tectonic faults (e.g., Fig. 4A).

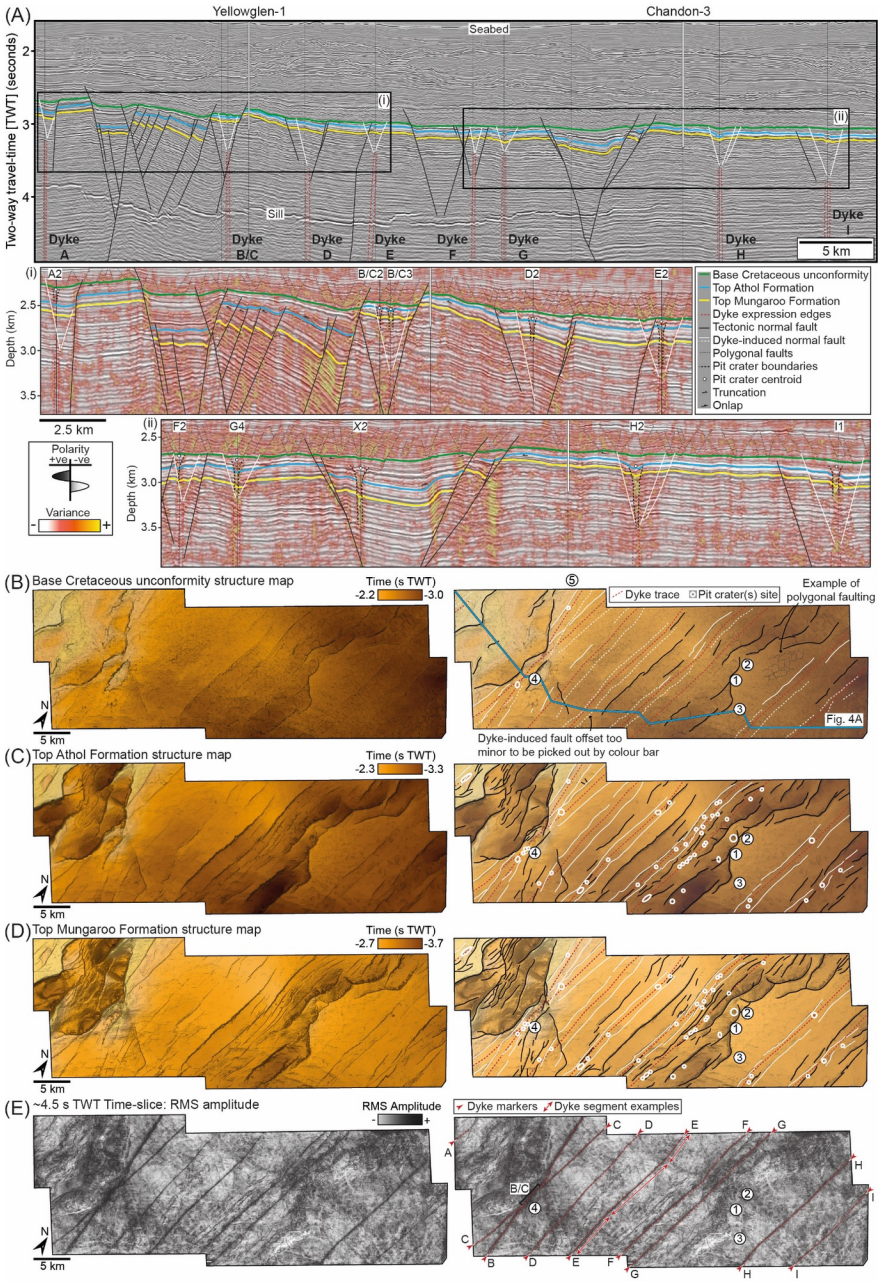

Figure 4: (A) Interpreted composite section capturing the tectono-stratigraphy of the area, intersecting all dykes (A-I) and revealing the structure some dyke-induced normal faults and pit craters. The line also intersects the Yellowglen-1 and Chandon-3 boreholes. The time-migrated data is shown in the top panel, and in the lower panels we show selected depth-converted, reflectivity data overlain by a variance attribute. See Figure 4B for line location. (B-C) Time-structure maps of the three major horizons (Base Cretaceous unconformity, Top Athol Formation, and Top Mungaroo Formation) interpreted in Figure 4A. Uninterpreted and interpreted versions of the maps are shown, highlighting underlying dyke traces, faults, and boreholes. The boreholes shown are: 1 = Chandon-1; 2 = Chandon-2; 3 = Chandon-3; 4 = Yellowglen-1; and 5 = Mercury-1. (E) Uninterpreted and interpreted RMS (root-mean squared) amplitude time-slice at 4.5 seconds two-way time (TWT) showing the seismic expression of dykes A-I. For part of their length, dykes B and C

merge and we cannot determine if both dykes are continuous, or if one cross-cuts and displaces the other.

Pit crater morphology

Pit craters occur across the dataset, primarily arranged in chains aligned parallel to and occurring within dyke-induced graben (Fig. 5). Five pit craters (*X1 –X5*) are located outside these graben and are instead situated in the hanging wall of tectonic normal faults (Fig. 5). Of the 54 pit craters within dyke-induced graben, 50 have a funnel-like morphology in cross-section, as do four of the pit craters associated with tectonic normal faults (Figs 5-8). The remaining four pit craters within dyke-induced graben (A4, F5, G7, and H1), as well as*X3* , have a pipe-like geometry and no inverted cone section (Figs 5-8).

At the Top Athol Formation, we mapped 61 pit craters (Fig. 5); three pit craters observed at this structural level merge (e.g., E1a and b, F10a and b, G10a and b; Figs 6E, 7A, and B) and one splits (G2/3; Fig. 8B) at shallower depths. Of the 57 pit craters within dyke-induced graben at the Top Athol Formation, 30 occur directly above dyke traces and 27 have centroids situated ˜75–653 m orthogonally from the associated dyke trace (Fig. 5C). The only pipe-like pit crater located directly above a dyke trace is A4 (Fig. 5).

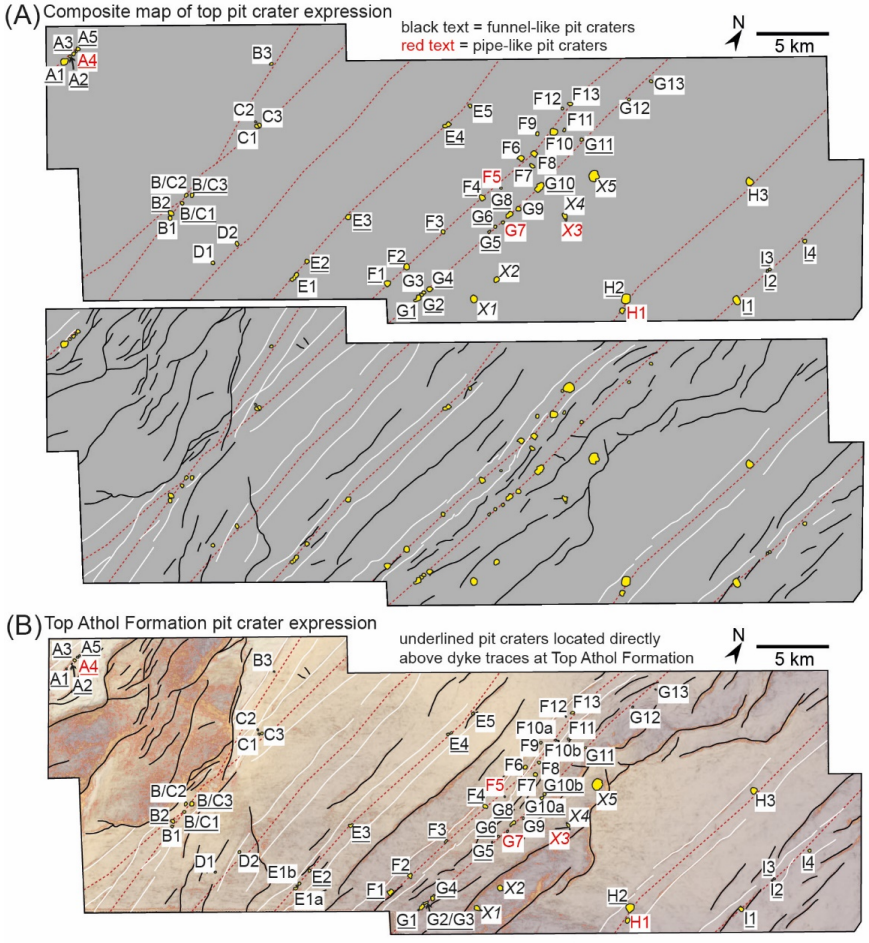

Figure 5: (A) Composite map showing the outlines of each pit crater at the shallowest stratigraphic level they occur at, relative to dyke and fault traces. (B) Map showing the expression of each pit crater at the Top Athol Formation.

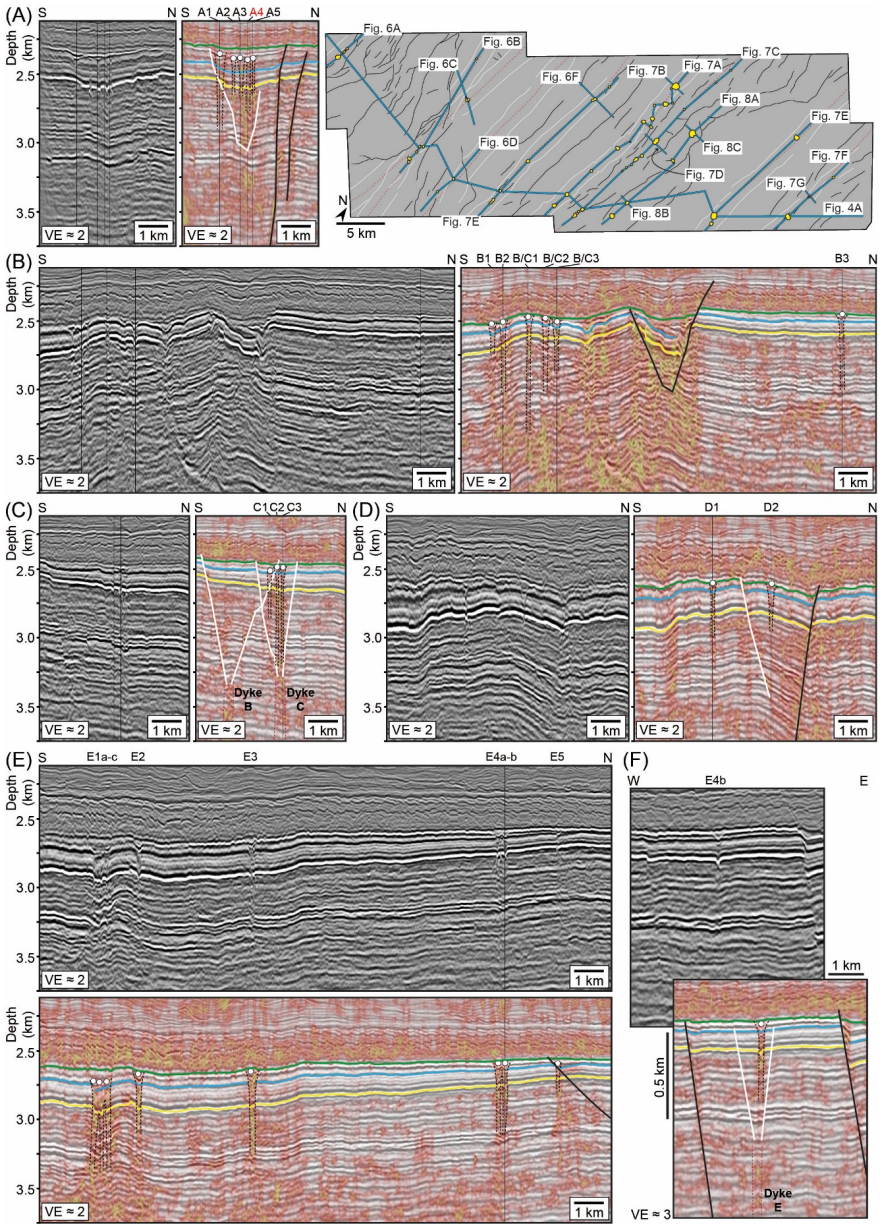

Figure 6: (A-F) Uninterpreted and interpreted, depth-converted seismic sections showing the structure of pit craters associated with dykes A-E. See Figure 4 for interpreted section key. VE = vertical exaggeration Inset: map showing line locations.

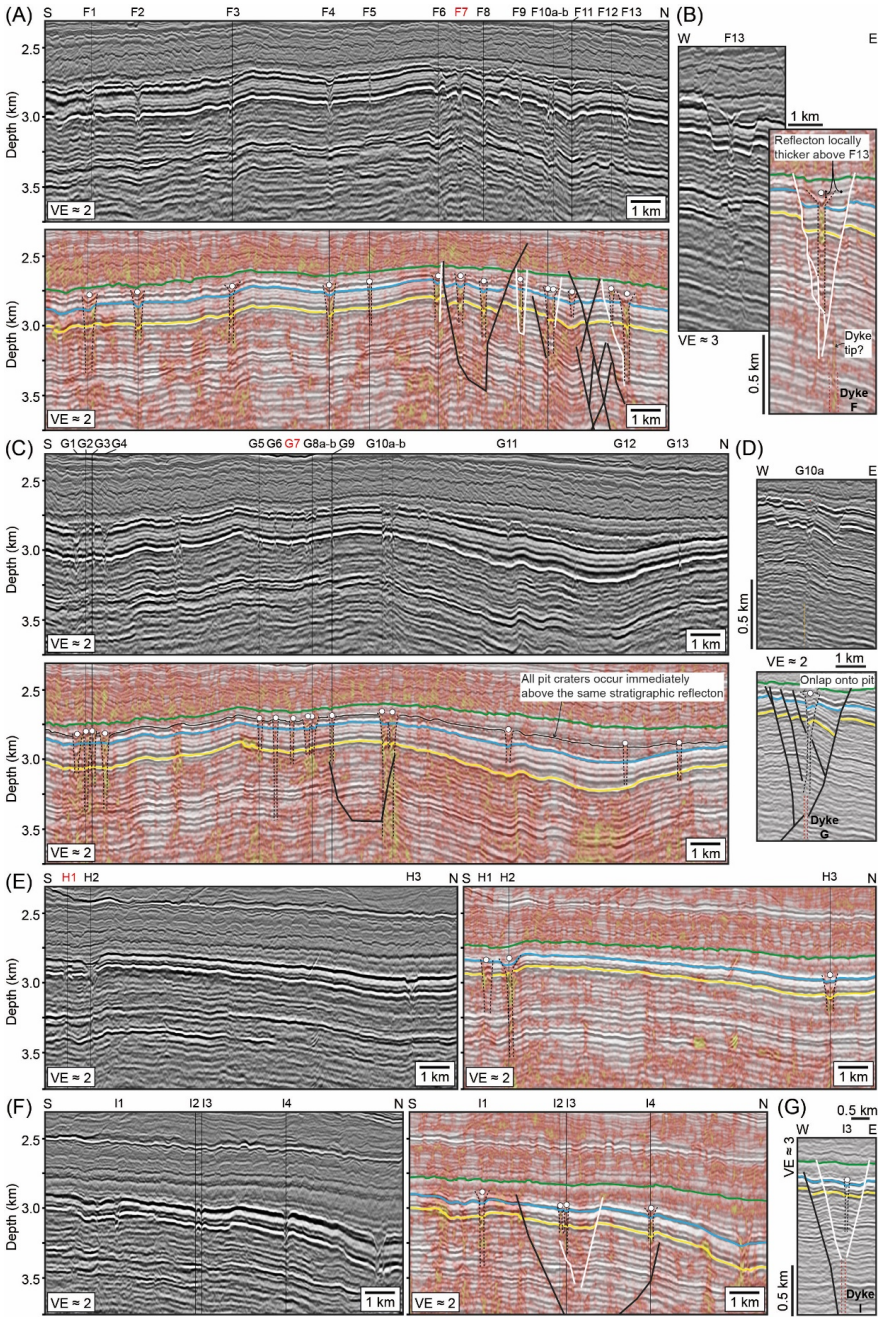

Figure 7: (A-G) Uninterpreted and interpreted, depth-converted seismic sections showing the structure of pit craters associated with dykes F-I. See Figure 4 for interpreted section key and Figure 7 for line locations.

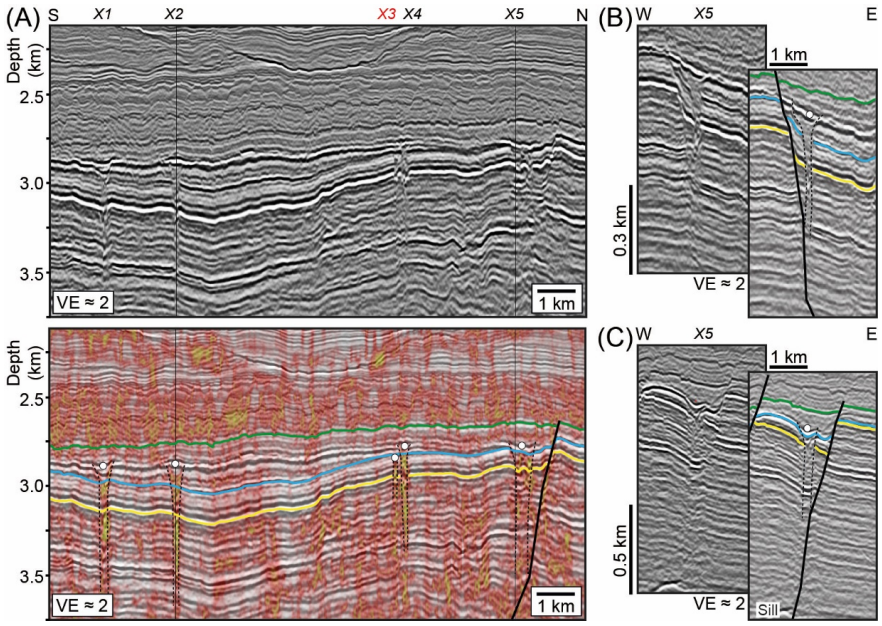

Figure 8: (A-C) Uninterpreted and interpreted, depth-converted seismic sections showing the structure of pit craters (X1-X5) associated with tectonic normal faults. See Figure 4 for interpreted section key and Figure 7 for line locations.

Plan-view geometry

Within dyke-induced graben, funnel-like pit crater tops have long axes of 150–740 m, areas of 0.05–1.24 km^2, and are quasi-circular to elliptical with aspect ratios of 1.04–3.05 (Fig. 9A; Supporting Table 1). The orientation of these pit crater long axes is variable, with a mean axis trend of 080° and a mode of 005–015° (Fig. 9B). At the Top Athol Formation, typically located below inverted cone sections, the pipes of these funnel-like pit craters are smaller in plan-view: long axis lengths are 108–585 m, aspect ratios are 1.01–3.14, and areas are 0.02–0.10 km^2 (Figs 9A and C; Supporting Table 1). For pipe-like pit craters within dyke-induced graben, their plan-view outlines at their tops are characterised by long axes of 170–390 m with no clear alignment, aspect ratios of 1.23–1.63, and areas of 0.06–0.39 km^2 (Figs 9A and C; Supporting Table 1). At the Top Athol Formation, pipe-like pit crater long axes within dyke-induced graben are 117–364 m, have aspect ratios of 1.22–1.47, and have areas of 0.04–0.32 km^2 (Figs 9A and C; Supporting Table 1).

The area and aspect ratio of the 29 pit craters situated directly above dykes broadly decrease ($R^2 = 0.55$) and seemingly increase ($R^2 = 0.29$) with depth, respectively, and tend to be larger than those above dyke-induced faults (Figs 9A, C, and D). Although the 29 pit craters above dykes cumulatively have a mean long axis orientation of 077°, six are oriented between 005–015°, sub-parallel to the mean axis (011°) of dyke segments in the study area (Fig. 9B). The size and shape of the 25 pit craters above dyke-induced faults varies non-systematically with depth; i.e. the correlation between area and aspect ratios measured at the pit crater tops and at the structurally deeper Top Athol Formation are $R^2 = 0.26$ and $R^2 = 0.08$, respectively (Figs 9A, C, and D).

Pit craters with a funnel-like morphology, but associated with tectonic normal faults (*X1* , *X2* , *X4* , and *X5*), are typically larger than those within dyke-induced graben and have long axes of 400–740 m, aspect ratios of 1.17–1.55, and areas of 0.33–1.47 km^2 at their tops (Fig. 9A; Supporting Table 1). At the Top Athol Formation, these funnel-like pit craters have long axes of 358–790 m, aspect ratios of 1.10–2.24, and areas of 0.18–1.66 km^2 (Fig. 9; Supporting Table 1). The only pit crater associated with a tectonic normal fault that does not have a funnel-like morphology (*X3*) is 140 m long, has an aspect ratio of 1.3, and an area of 0.05 km^2 at its top (Fig. 9A; Supporting Table 1). At the Top Athol Formation, this pipe-like pit crater

is 98 m long, has an aspect ratio of 1.6, and an area of 0.02 km^2(Fig. 9A; Supporting Table 1). Of the pit craters above tectonic faults, some increase in area or aspect ratio with depth, whereas others decrease (Figs 9C and D). There is no preferred orientation of pit crater long axes above tectonic faults (Fig. 9B).

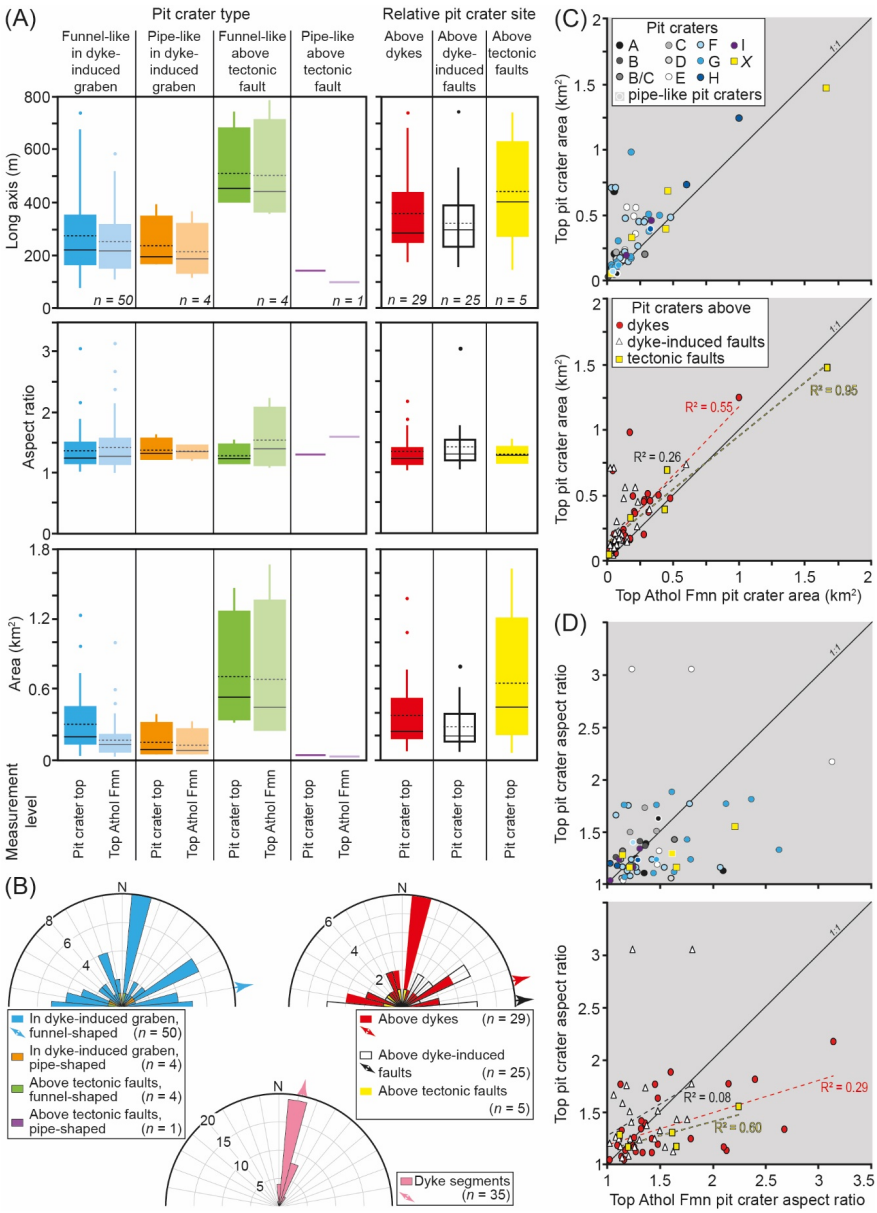

Figure 9: (A) Box and whisker plots comparing the long axes, aspect ratios, and areas of pit craters measured at two stratigraphic levels, distinguishing those that have different geometries (i.e. funnel-like and pipe-like) and/or associated with different structures (i.e. dykes, dyke-induced faults, and tectonic faults) (Supporting Table 1). n = number. The plots also highlight data median (thin black line), mean (dashed black line), and outliers. See Figure 3B for explanation of measured parameters. (B) Rose plots showing the orientation of pit crater long axes, grouped based on their morphology and/or association with different structures (Supporting Table 1). Arrows show the mean vector of select populations. Orientation of dyke segments is also shown (Magee & Jackson, 2020a). (C and D) Graphs comparing the area (C) and aspect ratio (B) of pit crater

expressions at their tops and at the Top Athol Formation. Two plots are provided for area and aspect ratio comparison, with one grouping the data based on the associated dyke or tectonic faults, and the other highlighting different between pit craters located directly above dykes, dyke-induced faults, and tectonic faults.

Cross-section geometry

In cross-section, pit crater walls typically bound zones within which stratigraphic reflections locally have a lower amplitude and are deflected (e.g., E4b) or displaced (e.g., F13) downwards relative to those in the flanking host rock (Figs 4A, 6-8). Pit crater centroids typically occur within the Dingo Claystone, ˜16–188 m (i.e. 0.5–5.5 seismic cycles where one cycle is a peak and trough pair) beneath the Base Cretaceous unconformity (Figs 4A, 6-8, 10A, and B). Only B1-B3 and D1-D2 are expressed at the Base Cretaceous unconformity (Fig. 10A). Stratigraphic reflections overlying some pit craters appear locally thickened (e.g., F13; Fig. 7B) whereas others seem to onlap onto crater walls (e.g., G10a; Fig. 7D).

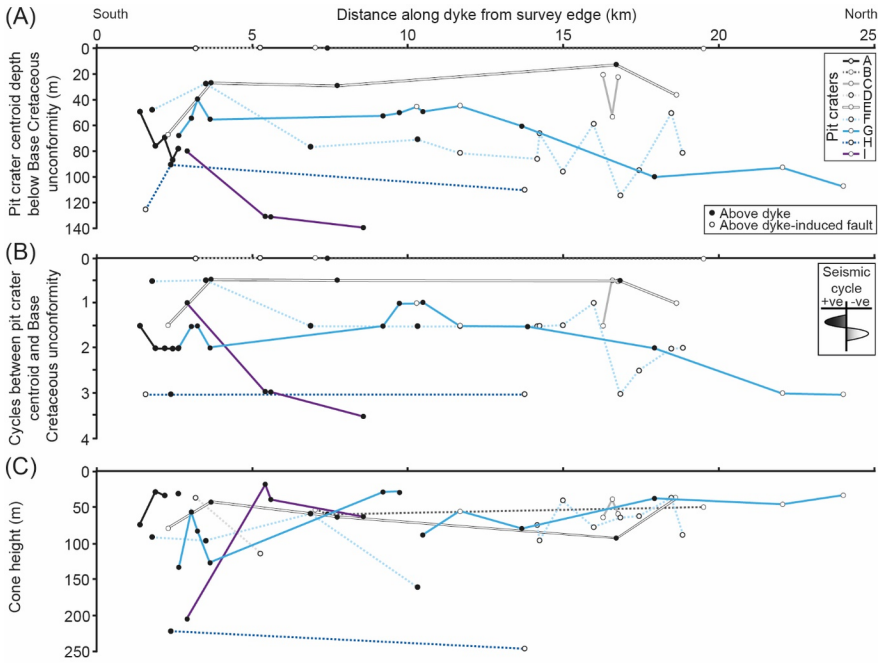

Figure 10: (A and B) Plots showing how deep (A) or how many seismic cycles (B) pit crater centroids are beneath the Base Cretaceous unconformity along dyke-strike (Supporting Table 1). Inset into (B): schematic depicting what constitutes a seismic cycle. (C) Plot of cone height along dyke strike (Supporting Table 1). See Figure 3B for explanation of measured parameters.

For each pit crater chain situated within dyke-induced graben, the depth of their pit crater centroids beneath the Base Cretaceous unconformity varies by [?]60 m along their length (Fig. 10A). Several pit crater chains (A, D, F, G, and I) show a broad northwards increase in centroid depth (Fig. 10A). Above some dykes, pit crater centroids all occur along the same stratigraphic reflection (i.e. D and G), even though the number of cycles between their level and the Base Cretaceous unconformity may vary (i.e., the post-overburden varies in thickness over a length-scale longer than that of an individual crater or chain of craters Figs 6D, 7B, and 10B). For other chains, pit crater centroids coincide with different (deeper or shallower) reflections along their length (i.e. A, B, C, E, F, H, and I; Figs 6, 7, and 10B). The pit craters associated with tectonic normal faults have centroids that occur at the same stratigraphic reflection above the Top Athol Formation, except for*X3* which is the only pit crater to terminate below the Top Athol Formation (Fig. 8).

The total height of the pit craters varies across the data, with most extending down into the Mungaroo

Formation (Figs 4A and 6-8); pit craters G5, G11, and G12 appear to terminate at or above the Top Mungaroo Formation (Fig. 7C). Our measurements show pit crater total height ranges from 114–868 m (Supporting Table 1). In places, mapped bases of pit crater pipes coincide with the upper tips of underlying dykes (G2, G4, G6, G10a, G12, and H2) or dyke-induced fault planes (B/C2, C2, C3, F9, F13, I2, and I3) (Figs 6-7). The *X1 -X5*pit crater pipes all extend down to tectonic faults (e.g., Fig. 8). Where the base of pit crater pipes intersect dyke-induced or tectonic faults, they typically do so where the fault planes are relatively steep or sub-vertical (e.g., Figs 6C, 7B, F, 8B, and C). Other pit craters appear to terminate within strata overlying dyke upper tips or fault planes (Figs 4A and 6-8).

Where pit craters display a funnel-like morphology, we measure the height of their inverted cone section and occasionally the deflection of the uppermost stratigraphic reflection within them (i.e. the deflection height) (Fig. 3B). We show inverted cone heights are ˜18–245 m, with slopes of 7–51°, and that these values vary across the study area and along individual pit crater chains (Figs 10C, 11A, and B; Supporting Table 1). The corresponding pipe height of these funnel-like pit craters are 27–789 m (Fig. 11A; Supporting Table 1); the heights of pipe-like pit craters are 107–254 m (Table 2). There is no correlation between cone height and total height or pipe height for pit craters within dyke-induced graben (either those above dykes or dyke-induced faults), or for those associated with tectonic normal faults (Figs 11A and B; Supporting Table 1). Deflection heights are ˜4–21 m, with slopes <12°, and do not correlate with either total height or cone height (Figs 11C and D; Supporting Table 1).

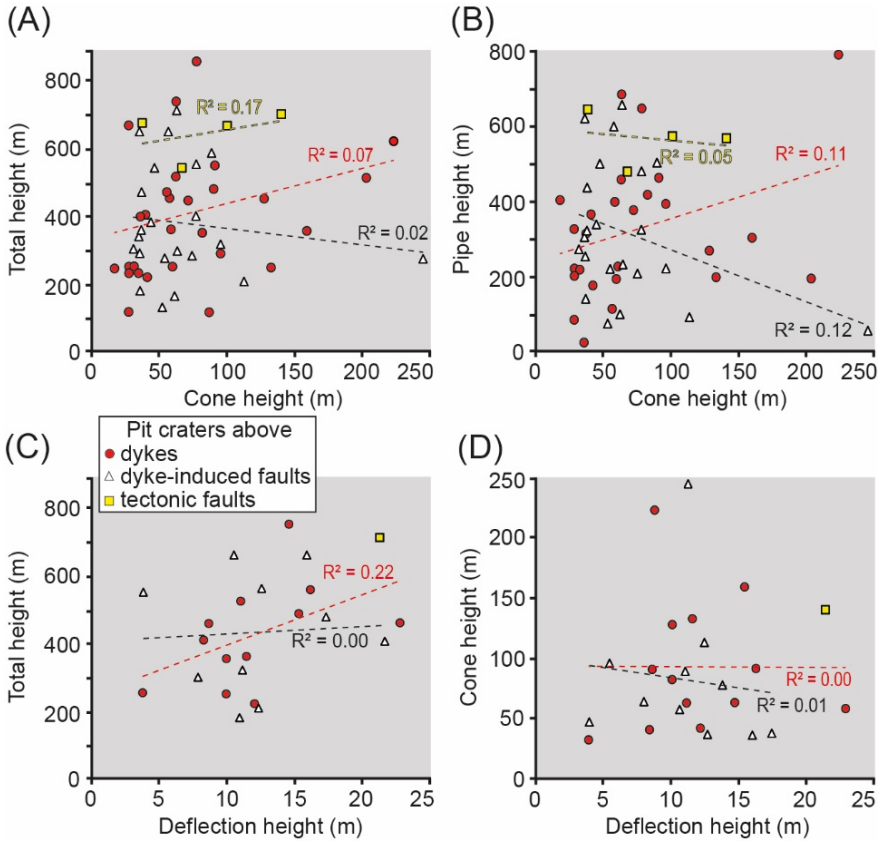

Figure 11: (A-D) Graphs comparing how the total height, pipe height, cone height, and deflection height relate (Supporting Table 1). See Figure 3B for explanation of measured parameters.

Comparative analyses

With our 3D seismic reflection data we are able to quantitatively assess relationships between the plan-view and cross-sectional geometry of the pit craters. Between pit crater total heights and long axis lengths there is a very weak positive correlation between for those above dykes ($R^2 = 0.17$), no meaningful correlation for pit craters above dyke-induced faults ($R^2 = 0.04$), but a strong positive correlation for those above tectonic faults ($R^2 = 0.71$) (Fig. 12A). Visually similar pit craters recognised elsewhere across the Exmouth Plateau within dyke-induced graben (e.g., Fig. 2D) display a moderate ($R^2 = 0.37$–0.50) positive correlation between total height and long axes (Fig. 12A) (see Velayatham et al., 2019). For all measured pit craters across the Exmouth Plateau there is no correlation (R^2[?]0.06) between total height and the aspect ratio of their long and short axes (Fig. 12B).

For pit craters above dykes, dyke-induced faults, and tectonic faults, there are positive, power-law correlations between cone height and pit crater long axes with R^2 values of 0.61, 0.24, and 0.77 respectively (Fig. 12C); these trends are consistent with power-law correlations that define pit crater depth and long axes of craters observed elsewhere on Earth and on other planetary bodies (Fig. 12C) (e.g., Ferrill et al., 2011; Gwinner et al., 2012; Okubo & Martel, 1998; Scott & Wilson, 2002; Whitten & Martin, 2019; Wyrick et al., 2004). There is no correlation ($<R^2 = 0.08$) between deflection height and pit crater long axes (Fig. 12C). Inverted cone volumes (1.34×10^{-4} km^3 to 2.71×10^{-2} km^3), and those of the deflected reflections (7.89×10^{-5} $km^3$to 1.62×10^{-3} km^3), are typically smaller than corresponding pipe volumes ($1.41\times10^{-3}km^3$ to $2.79\times10^{-1}km^3$) (Supporting Table 1).

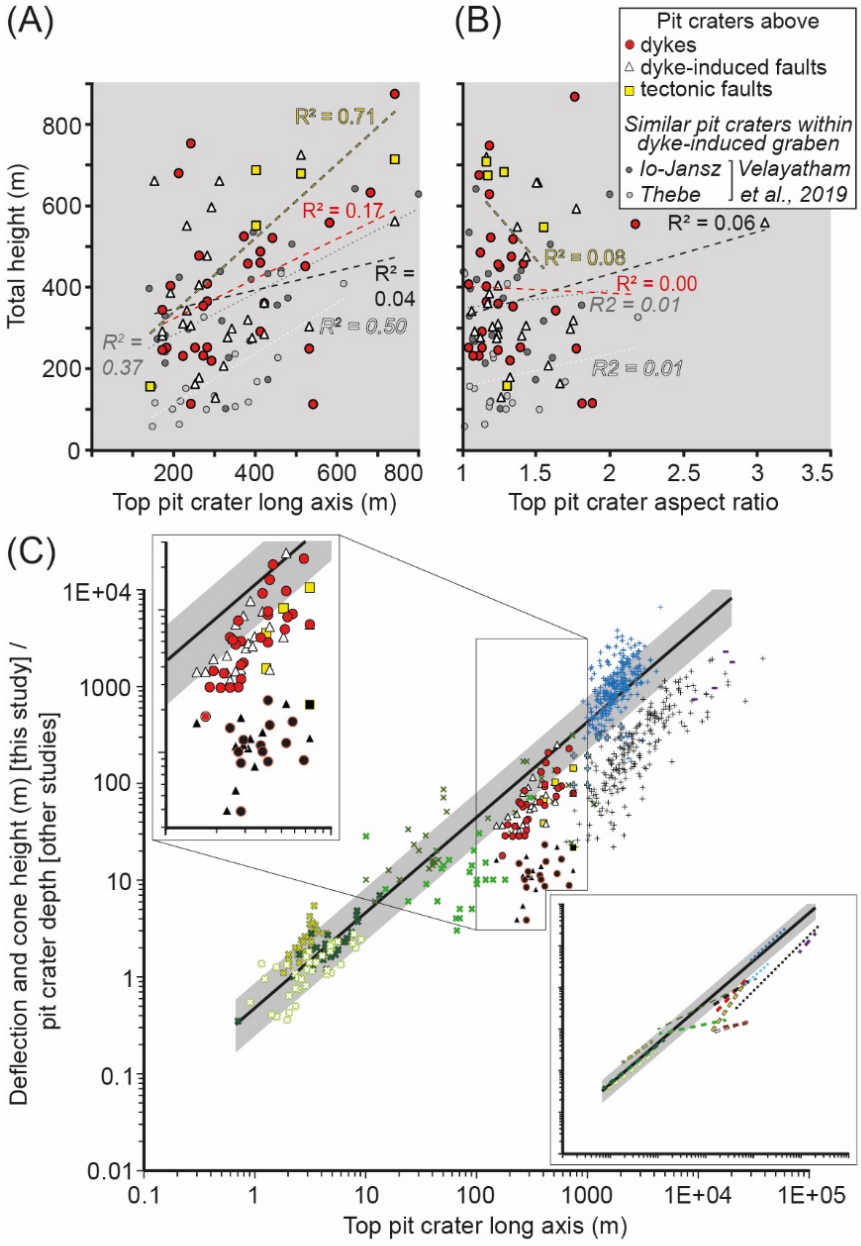

Symbol	Power-law	This study	
		Dyke-related cones	R² = 0.61
		Dyke-induced fault-related cones	R² = 0.24
		Tectonic fault-related cones	R² = 0.77
		Dyke-related deflections	R² = 0.03
		Dyke-induced fault-related deflections	R² = 0.08
		Tectonic fault-related deflections	
		Pit craters inferred to be dyke- / fault-related	
		Mercury (Gwinner et al., 2012)	R² = 0.80
		Mars (Kling et al., 2021)	R² = 0.69
		Mars (Wyrick et al., 2004)	R² = 0.90
		Mars (Scott and Wilson, 2002)	R² = 0.75
		Earth - Hawaii (Okubo et al., 1998)	R² = 0.64
		Earth - Iceland (basalt host; Whitten and Martin, 2019)	R² = 0.45
		Earth - Iceland (deltaic host; Whitten and Martin, 2019)	R² = 0.79
		Earth - Iceland (Ferrill et al., 2011)	R² = 0.49
		Earth - Syria (Frumkin and Naor, 2019)	R² = 0.05
		+ standard error	
		Power-law best-fit ($y = 0.44x^{0.9949}$)	R² = 0.94

Figure 12: (A and B) Plots comparing total height to pit crater long axes (A) and aspect ratio (B) for those located above dykes, dyke-induced faults, and tectonic faults (Supporting Table 1). Data is also shown from two other 3D seismic surveys (Io-Jansz and Thebe) from the Exmouth Plateau, although the exact relation of each pit crater to underlying structure is unknown (Velayatham et al., 2019). (C) Log-log plot of deflection and cone height, one of which is expected equivalent to pit crater depth (e.g., Wyrick et al., 2004), compared to pit crater long axis. Insets show a zoomed-in view of our data and the power-law best-fit trendlines for each plotted dataset. The power-law best-fit trendline shown (black line) with standard errors was calculated from all literature data plotted, with the exception of data from Frumkin and Naor (2019) and Kling et al., (2021) as these pit craters show evidence of post-formation modification.

Discussion

Pit crater structure

Seismic reflection data provides unique opportunities to image and quantify the entire 3D geometry of pit craters. Like pit craters observed elsewhere on Earth and other planetary bodies, those on the Exmouth Plateau have manifest as the as quasi-circular depressions, which in plan-view are commonly arranged in chains (e.g., Figs 3A and 5). Offset of stratigraphic reflections within most mapped pit craters indicate that these structures form because of spatially restricted host rock subsidence (Figs 3A, 4A, and 6-8). This subsidence is confined to cylindrical pipe-like structures with sub-vertical walls, which towards their tops commonly widen and become inwardly inclined, broadly describing an inverted conical shape (i.e. they are funnel-like) (Figs 3A, 4A, 6-8, and 9C). These observations are consistent with the inferred subsurface geometry of pit craters recognised elsewhere and those modelled using physical or numerical approaches (e.g., Ferrill et al., 2011; Kettermann et al., 2019; Wyrick, 2004; Wyrick et al., 2015). We note that the subsided strata within the studied pit craters typically have a lower amplitude and/or higher variance expression compared to reflections in the flanking host rock (Figs 2D, 3A, 4A, and 6-8). These seismic attribute changes indicate less seismic energy was reflected from within the pit crater, perhaps due to increased scattering of seismic energy from and/or local decreases in acoustic impedance across disrupted beeding (Brown, 2011). Both controls on the amount of seismic energy reflected could be linked to disaggregation of and fluid infiltration through rock during or after subsidence, which are likely common processes during pit crater formation (e.g., Frumkin & Naor, 2019; Halliday, 1998; Velayatham et al., 2018).

Pit crater age

Where data resolution allows, some reflections we observe above the pit craters appear thickened (e.g., F13; Fig. 7B) and/or onlap onto the conical walls of pits (e.g., G10a; Fig. 7D). These seismic-stratigraphic relationships imply that the strata represented by these reflections were deposited *within* the pit craters; i.e. the pit craters were surficial features, similar to those recently formed on Earth (Abelson et al., 2003; Frumkin & Naor, 2019; Okubo & Martel, 1998; Whitten & Martin, 2019). Having established that the shallowest expression of the pit craters likely marks the contemporaneous surface to their formation, we can use biostratigraphic data from local boreholes to estimate their age.

The youngest pit craters (B1-3, D1-2) formed coincident with the Base Cretaceous unconformity at ˜148 Ma (Figs 6B and D). Critically, the uppermost expression of pit craters across the study area and along individual chains (e.g., A–C, E, F, H, and I) often occur at different stratigraphic horizons above the ˜165 Ma Top Athol Formation (Figs 6-7, 10A, and B). These observations indicate the pit craters developed periodically during deposition of the marine Dingo Claystone in the Late Jurassic (Figs 2B, 6-7, 10A, and B). For some pit crater chains, specifically D1-D2 and G1-G13, the tops of individual pits occur along the same stratigraphic horizon suggesting they formed near-synchronously (Figs 6D, 7B, 10A, and B).

Our inferred Late Jurassic timing of pit crater formation is consistent with seismic-stratigraphic constraints on the age of the Exmouth Dyke Swarm and associated dyke-induced faults (Fig. 2) (Magee & Jackson, 2020a). As most pit craters are found below the ˜148 Ma Base Cretaceous unconformity, but all dyke-induced faults offset this horizon, it seems likely that pit crater formation generally ceased before dyking and associated faulting ended (Figs 4B and C) (Magee & Jackson, 2020a). Overall, we suggest that the oldest

pit craters occurred during the early development of the Exmouth Dyke Swarm and associated dyke-induced faults, with dyking and fault growth occurring (periodically) up until ˜148 Ma.

Pit crater origin

Numerous processes involving underlying cavity collapse or the volumetric reduction of a subsurface body have previously been proposed to generate space for overburden subsidence and pit crater formation (Fig. 1B) (see Wyrick et al., 2004 and references therein). We identify no clear cavity-like structures at the pit crater bases (Figs 3A, 4A, and 6-8), and disregard the following possible mechanisms of pit crater formation: (i) carbonate or salt dissolution (Fig. 1C [i]) (Abelson et al., 2003; Spencer & Fanale, 1990), because the Triassic-to-Late Jurassic strata hosting the pit craters contains no (or only very little) carbonate rocks and no salt (Fig. 2B) (e.g., Exon et al., 1992; Stagg et al., 2004; Tindale et al., 1998); (ii) evacuation of lava tubes (see Sauro et al., 2020 and references therein), as there is no evidence for high-amplitude, sinuous, strata-concordant reflections that could be attributed to lava flows or tubes (Figs 3A, 4A, and 7-9) (e.g., Sun et al., 2019); and (iii) magma migration from a reservoir (e.g., Mège et al., 2003; Poppe et al., 2015), as there is no evidence for underlying tabular igneous intrusions (e.g., sills or laccoliths) (Figs 3A, 4A, and 6-8), which are typically expressed as high-amplitude, positive, sub-horizontal-to-inclined reflections (e.g., Planke et al., 2005). Instead, we find that some pit craters directly emanate from either the upper tips of dykes (n = 6), dyke-induced fault planes (n= 6), or tectonic faults (n = 5) (Figs 6-8). Where we observe pit crater bases situated some distance above dyke upper tips or dyke-induced faults (Figs 6-8), we consider it plausible that seismically unresolved or obscured portions of their pipes extend down to these underlying structures. Our observations allow for the generation of these pit craters in response to the opening of vertical tensile fractures (Fig. 1C [iv]) (e.g., Ferrill et al., 2011; Smart et al., 2011; Tanaka & Golombek, 1989), which cannot be imaged in seismic reflection data.

The generation of pit craters linked to dyke tips may be driven by (Fig. 1C [vi]): (i) a volume reduction of the dyke itself, perhaps as magma pressure wanes or volatiles escape (e.g., Patterson et al., 2016; Scott & Wilson, 2002); (ii) escape of heated pore fluids from the tip-adjacent host rock and subsequent porosity collapse (e.g., Schofield et al., 2010); (iii) phreatic eruption (Hughes et al., 2018); and/or (iv) subsidence of material into a tensile fracture that opens above an inflating and widening dyke (similar to Fig. 1C [iv]) (e.g., Ferrill et al., 2011; Smart et al., 2011; Tanaka & Golombek, 1989). We show that within some pit crater chains, the tops of individual pits located directly above dykes occur at deeper stratigraphic levels and are thus older towards the north of our study area (e.g., above dykes A and I; Figs 10A and B). These occurrences of pit crater tops at multiple stratigraphic levels above single dykes indicate that periods of sediment deposition separated pit crater formation (Fig. 13); this interpretation is consistent with fault displacement data, which reveals the dyke-induced faults likely grew incrementally via segment linkage (Magee & Jackson, 2020b). As the dykes are part of a radial dyke swarm that intruded laterally northwards (Fig. 2A) (Magee & Jackson, 2020a), the apparent southwards decrease in age of the pit craters suggests that they did not develop above propagating dyke tips (Fig. 13A). Dyke thickness also decreases gradually northwards (Magee & Jackson, 2020a), so it seems unlikely that pit crater formation occurred in response to dyke widening and tensile fracturing of the overburden; i.e. we should expect areas where dyke width is greatest to generate pit craters first (Fig. 13B). We suggest that the possible southwards decrease in age of pit craters directly above dykes may have occurred due to localised volume reductions of the intrusion as driving pressure periodically waned (Fig. 13C). Such volume reductions could have been driven by magma backflow and retreat (e.g., Philpotts & Asher, 1994; Philpotts & Philpotts, 2007), or solidification and contraction (e.g., Caricchi et al., 2014). Cyclical periods of intrusion and driving pressure waning could create complex trends of pit craters along individual dykes.

Pit craters linked to faults observed elsewhere on the Exmouth Plateau have been attributed to local reduction of confining pressure and fluid escape from an overpressured horizon in the Mungaroo Formation during faulting (e.g., Fig. 1C [ii]) (Velayatham et al., 2019; Velayatham et al., 2018). We show that some pit craters link to steep-to-sub-vertical fault portions, suggesting their formation may also be associated with the collapse of dilatational jogs (Figs 1C [v], 7B, 8B, and C) (e.g., Ferrill & Morris, 2003; Ferrill et al., 2011;

Ketterman et al., 2015; Kettermann et al., 2019; Smart et al., 2011; Von Hagke et al., 2019).

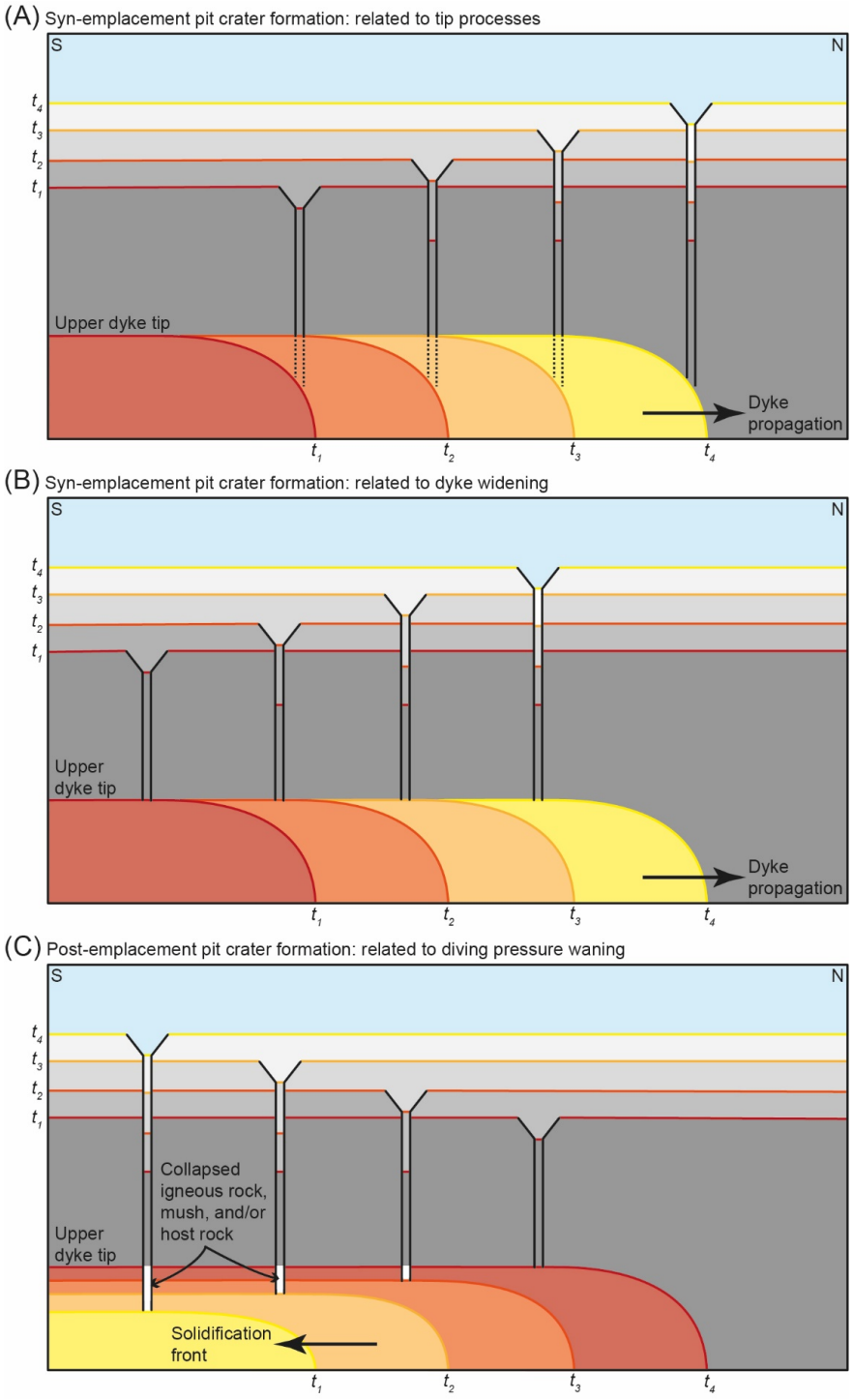

Figure 13: Schematic models describing how pit crater may be expected to relate to different dyke processes. (A) Pit crater formation is linked to lateral propagation of the dyke tip, perhaps driven by fluid escape into and/or collapse of the tip cavity, or eruption (Hughes et al., 2018; Scott & Wilson, 2002). Pit crater

age decreases further from the dyke source. (B) Pit crater formation occurs as the dyke widens behind the propagating tip, perhaps linked to tensile fracturing (Tanaka & Golombek, 1989) as dyke widening induces extension of the overlying rock, fluid escape into and/or collapse of the tip cavity, or eruption (Hughes et al., 2018; Scott & Wilson, 2002). Pit crater age decreases further from the dyke source. (C) Pit crater formation occurs as the magma driving pressure or supply wanes, causing magma to flow backwards (e.g., Philpotts & Asher, 1994) and/or solidify and contract (i.e. a volume reduction) (e.g., Caricchi et al., 2014). Pit crater age increases further from the dyke source.

Pit crater depth

Where pit craters are observed on the surface of Earth and other planetary bodies, we are typically restricted to measuring their plan-view geometry (e.g., axial dimensions) and crater depth (e.g., Whitten & Martin, 2019; Wyrick et al., 2004). Numerous studies have demonstrated that pit crater depths of most populations likely related to dyke or fault activity, positively correlates with their long axis length via power-law relations (R^2 = 0.45–0.90) with similar slopes (Fig. 12C) (e.g., Ferrill et al., 2011; Gwinner et al., 2012; Kling et al., 2021; Okubo & Martel, 1998; Scott & Wilson, 2002; Whitten & Martin, 2019; Wyrick et al., 2004); all these data can be fit by a power-law relationship (R^2 = 0.94; Fig. 12C). Some pit craters within the Golan volcanic province, southern Levant, are an exception to this power-law trend as they show no correlation between pit crater depth and long axis, which has been attributed to recent modification by erosion and sedimentation (R^2 = 0.05; Fig. 12C) (Frumkin & Naor, 2019).

From our seismic reflection data, we can measure pit crater morphometric properties, but we first need to establish whether the height of the inverted cone sections we describe, or that of the deflected reflections they contain, are equivalent to pit crater depth (Fig. 3B). For pit craters above dykes, dyke-induced faults, and tectonic faults, we find that cone height and pit long axis length positively correlate (R^2 = 0.61, 0.24, and 0.77, respectively) and overlaps with data from many other locations (Fig. 12C). However, there is no meaningful correlation (R^2 = <0.1) for deflection height and pit long axis length (Fig. 12C). The deflection height measurements also fall an order of magnitude below the power-law trend fit to the compiled published pit crater data; this is similar to pit craters in the Golan volcanic province and Noctis Labyrinthus (Mars), both of which display evidence for post-formation modification of their initial geometries (Fig. 12C) (Frumkin & Naor, 2019; Kling et al., 2021). Based on these comparisons, we suggest that the walls of the inverted cone sections represent the original pit crater morphology (Fig. 14). The reflections within the inverted cone sections are interpreted to correspond to material that infilled the pit crater (Fig. 14). Our results support recent suggestions that relationships between pit crater depths and long axis lengths may provide some indication as to whether post-formation erosional and infilling processes have modified pit geometry (Figs 12C and 14) (Frumkin & Naor, 2019; Kling et al., 2021).

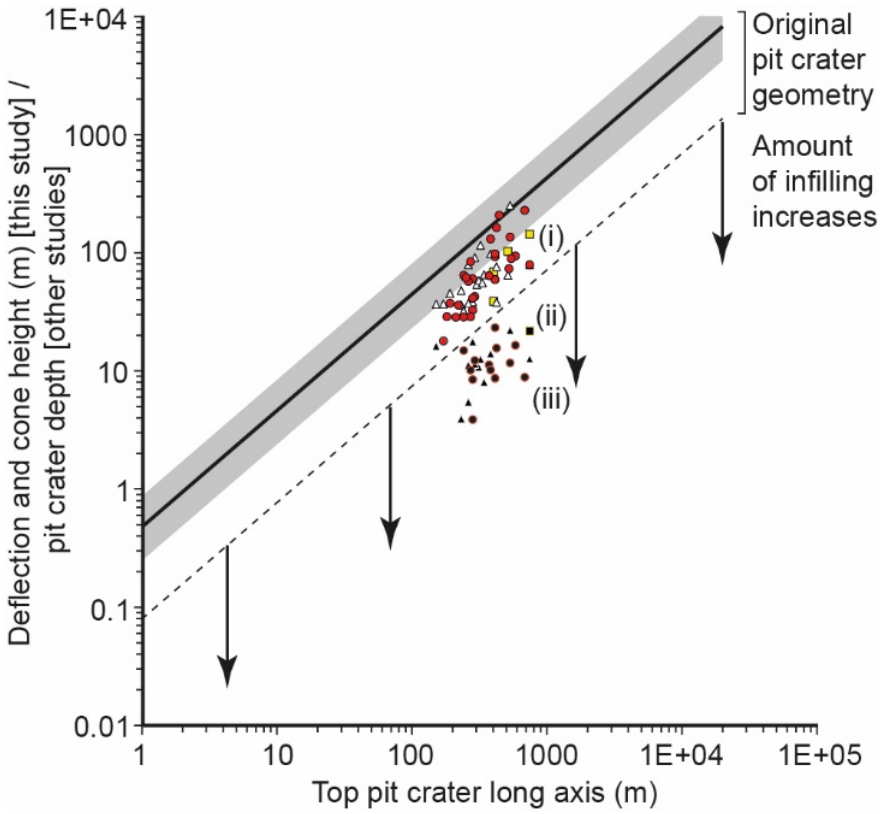

Figure 14: Simplified version of Figure 12C showing our deflection and cone height data plotted against pit crater long axis, coupled with the power-law trend of all literature data used. We define an arbitrary boundary between areas where original pit crater geometries are likely preserved and those where infilling may modify apparent pit crater depths. Inset: sketches showing how infilling may modify pit crater depths.

Can we relate the surface expression of pit craters to subsurface structures and processes?

The surface expression of pit craters observed on Earth and other planetary bodies has been used to infer how they formed and establish characteristics of subsurface geology (e.g., regolith depth) (e.g., Kling et al., 2021; Korteniemi et al., 2010; Martin et al., 2017; Mège & Masson, 1997; Smart et al., 2011; Whitten & Martin, 2019). For example, we may expect pit craters long axes, like that of volcanic vents, to align parallel to underlying dykes as they form within the same stress field (Bonini & Mazzarini, 2010; Magee et al., 2016; Paulsen & Wilson, 2010). Because we have established that pit crater formation was related to either be dyking or faulting, and because we can image these features in 3D, we can examine pit crater morphologies to see if magmatic and tectonic origins can be distinguished. Aside from cone height (pit crater depth) and long axis lengths, our data demonstrates that most pit crater properties are only weakly positively correlated or that there is no correlation at all (Figs 11 and 12). Critically, there are no significant differences in sizes of pit craters developed above dykes, dyke-induced faults, or tectonic faults (Figs 11 and 12). The pit craters we analyse also show no preferred long axis orientation, even those seemingly related to contemporaneous dykes and dyke-induced faults that are clearly aligned ˜N-S (Fig. 12B). The disparity in dyke and dyke-induced fault orientation relative to the elongation of the pit craters implies formation of the latter was not sensitive to the prevailing stress field, perhaps because they formed in unconsolidated wet sediments. Overall, our data suggest that pit craters related to dyking, dyke-induced faulting, or tectonic faulting cannot be easily distinguished based on their surficial size and orientation (Figs 9A, C, and 12).

In addition to relating surface expression to pit crater formation, pit crater depths have been used as a

proxy for regolith thickness on other planetary bodies (e.g., Whitten & Martin, 2019; Wyrick et al., 2004). This use of pit crater depth follows the inference that drainage of loose, unconsolidated material into an underlying cavity instigates development of an inverted cone section controlled by the host materials angle of repose (e.g., Whitten & Martin, 2019; Wyrick et al., 2004). Our pit craters formed during deposition of the marine Dingo Claystone (Tindale et al., 1998), so we assume their contemporaneous shallow sub-seabed material was unconsolidated and wet. Although the presence of pore fluids may alter the behaviour of host sediment relative to dry regolith on other planetary bodies, it seems reasonable to expect both materials to respond similarly to localised subsidence; i.e. they should drain into underlying pipes. However, we show that cone height (i.e. pit crater depth) varies non-systematically across the study area, including along individual chains, with adjacent pit craters of the same age often displaying different cone heights (Figs 6-8 and 10). Furthermore, some pit craters seemingly have no seismically resolved inverted cone section and appear simply to have a pipe-like geometry (Figs 6-8). Assuming that the transition from unconsolidated wet sediment to lithified rock (i.e. perhaps equivalent to a regolith-rock transition) occurred at a relatively constant depth across the study area, the observed variation in pit crater cone heights and their local absence suggest the changing rheology of the host material did not primarily control pit crater geometry (cf. Whitten & Martin, 2019; Wyrick et al., 2004).

Conclusions

Here, we use seismic reflection data from offshore NW Australia to image the entire 3D geometry of pit craters and underlying magmatic and tectonic structures. Our work demonstrates that pit craters link at depth to dykes and steep fault segments, confirming pit crater formation can occur in response to magmatic processes and dilatational faulting. We also show that pit crater depths strongly correlate with their long axis lengths, consistent with observations of pit craters elsewhere on Earth and other planetary bodies; deviation of pit crater populations from the power-law trend that defines these may be an indicator that pit craters have been infilled and/or modified. Our results suggest that we should be cautious when interpreting the origin of pit craters on other planetary bodies because: (i) the distribution and size of pit craters may not be diagnostic of the potential dyking and/or faulting processes driving their formation; and (ii) pit crater size may not simply relate to the mechanical properties of the host material (e.g., regolith) or their driving mechanism. Overall, our work shows that reflection seismology is a powerful tool for subsurface exploration on other worlds, as it allows us to examine the 3D structure of features on Earth thought analogous to those recognised on the surfaces of other planetary bodies.

Acknowledgements

We are grateful to Geoscience Australia for making the data we use freely available, and to Schlumberger for providing use of Petrel seismic interpretation software. Funding for this work was acquired by Magee as part of a NERC Independent Research Fellowship (NE\R014086\1) and a Royal Society International Exchange Grant (IES\R3\193221).

Data availability statement

Seismic reflection and well data used in this study are freely available from the Geoscience Australia NOPIMS (https://nopims.dmp.wa.gov.au/nopims) data repository. The NOPIMS data access centre allows 'Wells' (i.e. for this study Chandon 1, Chandon 2, Chandon 3, Mercury 1, and Yellowglen 1) and 'Surveys' (i.e. for this study the Chandon 3D MSS seismic reflection survey) from offshore Australia to be searched for. From these search results, well data can be downloaded by highlighting the correct well and using 'view details for selected rows'; due to the file size of seismic reflection segy data like the Chandon 3D MSS, few can be downloaded but all can be added to a basket and freely requested from Geoscience Australia. All measurements and calculations acquired during this research are provided in Supporting Table 1 and copies will be hosted in the National Geoscience Data Centre of the British Geological Survey (https://www.bgs.ac.uk/geological-data/national-geoscience-data-centre/) and Figshare (https://figshare.com/).

References

Abelson, M., Baer, G., Shtivelman, V., Wachs, D., Raz, E., Crouvi, O., et al. (2003). Collapse-sinkholes and radar interferometry reveal neotectonics concealed within the Dead Sea basin. *Geophysical Research Letters, 30* (10), 1545.

Bilal, A., McClay, K., & Scarselli, N. (2018). Fault-scarp degradation in the central Exmouth Plateau, North West Shelf, Australia. *Geological Society, London, Special Publications, 476* , SP476. 411.

Black, M., McCormack, K., Elders, C., & Robertson, D. (2017). Extensional fault evolution within the Exmouth Sub-basin, North West Shelf, Australia. *Marine and Petroleum Geology, 85* , 301-315.

Bonini, M., & Mazzarini, F. (2010). Mud volcanoes as potential indicators of regional stress and pressurized layer depth. *Tectonophysics, 494* (1), 32-47.

Brown, A. R. (2011). *Interpretation of three-dimensional seismic data* (6th ed. Vol. 42). Oklahoma, USA: AAPG and SEG.

Caricchi, L., Biggs, J., Annen, C., & Ebmeier, S. (2014). The influence of cooling, crystallisation and re-melting on the interpretation of geodetic signals in volcanic systems. *Earth and Planetary Science Letters, 388* , 166-174.

Chopra, S., & Marfurt, K. J. (2005). Seismic attributes—A historical perspective. *Geophysics, 70* (5), 3SO-28SO.

Direen, N. G., Stagg, H. M. J., Symonds, P. A., & Colwell, J. B. (2008). Architecture of volcanic rifted margins: new insights from the Exmouth – Gascoyne margin, Western Australia. *Australian Journal of Earth Sciences, 55* (3), 341-363.

Driscoll, N. W., & Karner, G. D. (1998). Lower crustal extension across the Northern Carnarvon basin, Australia: Evidence for an eastward dipping detachment. *Journal of Geophysical Research: Solid Earth (1978–2012), 103* (B3), 4975-4991.

Exon, N., Haq, B., & Von Rad, U. (1992). *Exmouth Plateau revisited: scientific drilling and geological framework.* Paper presented at the Proceedings of the Ocean Drilling Program, Scientific Results.

Ferrill, D. A., & Morris, A. P. (2003). Dilational normal faults. *Journal of Structural Geology, 25* (2), 183-196.

Ferrill, D. A., Wyrick, D. Y., Morris, A. P., Sims, D. W., & Franklin, N. M. (2004). Dilational fault slip and pit chain formation on Mars. *GSA Today, 14* (10), 4.

Ferrill, D. A., Wyrick, D. Y., & Smart, K. J. (2011). Coseismic, dilational-fault and extension-fracture related pit chain formation in Iceland: Analog for pit chains on Mars. *Lithosphere, 3* (2), 133-142.

Frumkin, A., & Naor, R. (2019). Formation and modification of pit craters–example from the Golan volcanic plateau, southern Levant. *Zeitschrift fur Geomorphologie, 62* (3), 163-181.

Gartrell, A., Torres, J., Dixon, M., & Keep, M. (2016). Mesozoic rift onset and its impact on the sequence stratigraphic architecture of the Northern Carnarvon Basin. *The APPEA Journal, 56* (1), 143-158.

Gwinner, K., Head, J., Oberst, J., Gillis-Davis, J., Xiao, Z., Strom, R., et al. (2012). Morphology of pit craters on Mercury from stereo-derived topography and implications for pit crater formation. (1659), 1991.

Halliday, W. R. (1998). " Pit Craters", lava tubes, and open vertical volcanic conduits in Hawaii: a problem in terminology. *International Journal of Speleology, 27* (1), 113-124.

Hocking, R. (1992). Jurassic deposition in the southern and central North West Shelf. *Western Australia: Geological Survey Western Australia Record, 199217* .

Hocking, R. M., Moors, H. T., & Van de Graaff, W. E. (1987). *Geology of the carnarvon basin, Western Australia* (Vol. 133): State Print. Division.

Horstman, K., & Melosh, H. (1989). Drainage pits in cohesionless materials: Implications for the surface of Phobos. *Journal of Geophysical Research: Solid Earth, 94* (B9), 12433-12441.

Hughes, S. S., Nawotniak, S. E. K., Sears, D. W., Borg, C., Garry, W. B., Christiansen, E. H., et al. (2018). Phreatic explosions during basaltic fissure eruptions: Kings Bowl lava field, Snake River Plain, USA. *Journal of Volcanology and Geothermal Research, 351* , 89-104.

Ketterman, M., Grutzner, C., Urai, J., Reicherter, K., & Mertens, J. (2015). Evolution of a highly dilatant fault zone in the grabens of Canyonlands National Park, Utah, USA–integrating fieldwork, ground-penetrating radar and airborne imagery analysis. *Solid Earth, 6* , 839-855.

Kettermann, M., Weismuller, C., von Hagke, C., Reicherter, K., & Urai, J. L. (2019). Large near-surface block rotations at normal faults of the Iceland rift: Evolution of tectonic caves and dilatancy. *Geology, 47* (8), 781-785.

Kling, C. L., Byrne, P. K., Atkins, R. M., & Wegmann, K. W. (2021). Tectonic Deformation and Volatile Loss in the Formation of Noctis Labyrinthus, Mars. *Journal of Geophysical Research: Planets* , e2020JE006555.

Korteniemi, J., Raitala, J., Aittola, M., Ivanov, M. A., Kostama, V.-P., Ohman, T., & Hiesinger, H. (2010). Dike indicators in the Hadriaca Patera–Promethei Terra region, Mars. *Earth and Planetary Science Letters, 294* (3), 466-478.

Longley, I., Buessenschuett, C., Clydsdale, L., Cubitt, C., Davis, R., Johnson, M., et al. (2002). The North West Shelf of Australia–a Woodside perspective. *The sedimentary basins of Western Australia, 3* , 27-88.

Magee, C., Duffy, O. B., Purnell, K., Bell, R. E., Jackson, C. A. L., & Reeve, M. T. (2016). Fault-controlled fluid flow inferred from hydrothermal vents imaged in 3D seismic reflection data, offshore NW Australia. *Basin Research, 28* (3), 299-318.

Magee, C., Ernst, R. E., Muirhead, J., Phillips, T., & Jackson, C. A.-L. (2019). Magma Transport Pathways in Large Igneous Provinces: Lessons from Combining Field Observations and Seismic Reflection Data. In R. Srivastava, R. Ernst, & P. Peng (Eds.), *Dyke Swarms of the World: A Modern Perspective* (pp. 45-85): Springer.

Magee, C., & Jackson, C.-L. (2020a). Seismic reflection data reveal the 3D structure of the newly discovered Exmouth Dyke Swarm, offshore NW Australia. *Solid Earth, 11* (2), 576-606.

Magee, C., & Jackson, C. A.-L. (2020b). Can we relate the surface expression of dike-induced normal faults to subsurface dike geometry?*Geology, 49* .

Marfurt, K. J., & Alves, T. M. (2015). Pitfalls and limitations in seismic attribute interpretation of tectonic features.*Interpretation, 3* (1), SB5-SB15.

Marshall, N., & Lang, S. (2013). *A new sequence stratigraphic framework for the North West Shelf, Australia.* Paper presented at the The Sedimentary Basins of Western Australia 4: Proceedings PESA Symposium. Perth.

Martin, E. S., Kattenhorn, S. A., Collins, G. C., Michaud, R. L., Pappalardo, R. T., & Wyrick, D. Y. (2017). Pit chains on Enceladus signal the recent tectonic dissection of the ancient cratered terrains.*Icarus, 294* , 209-217.

Mege, D., Cook, A. C., Garel, E., Lagabrielle, Y., & Cormier, M. H. (2003). Volcanic rifting at Martian grabens. *Journal of Geophysical Research: Planets, 108* (E5).

Mege, D., & Masson, P. (1996). A plume tectonics model for the Tharsis province, Mars. *Planetary and Space Science*

44 (12), 1499-1546.

Mege, D., & Masson, P. (1997). *Graben formation and dike emplacement on Earth and other planets.* Paper presented at the Lunar and Planetary Science Conference.

Muirhead, J. D., Kattenhorn, S. A., & Le Corvec, N. (2015). Varying styles of magmatic strain accommodation across the East African Rift. *Geochemistry, Geophysics, Geosystems* .

Okubo, C. H., & Martel, S. J. (1998). Pit crater formation on Kilauea volcano, Hawaii. *Journal of Volcanology and Geothermal Research, 86* (1), 1-18.

Paganoni, M., King, J. J., Foschi, M., Mellor-Jones, K., & Cartwright, J. A. (2019). A natural gas hydrate system on the Exmouth Plateau (NW shelf of Australia) sourced by thermogenic hydrocarbon leakage. *Marine and Petroleum Geology, 99* , 370-392.

Partington, M., Aurisch, K., Clark, W., Newlands, I., Phelps, S., Senycia, P., et al. (2003). The hydrocarbon potential of exploration permits WA-299-P and WA-300-P, Carnarvon Basin: a case study. *The APPEA Journal, 43* (1), 339-361.

Patterson, C. W., Ernst, R. E., & Samson, C. (2016). Pit Chains Belonging to Radiating Graben-Fissure Systems on Venus: Model for Formation during Lateral Dyke Injection. *Acta Geologica Sinica (English Edition), 90* (s1), 143-144.

Paulsen, T. S., & Wilson, T. J. (2010). New criteria for systematic mapping and reliability assessment of monogenetic volcanic vent alignments and elongate volcanic vents for crustal stress analyses. *Tectonophysics, 482* (1), 16-28.

Paumard, V., Bourget, J., Payenberg, T., Ainsworth, R. B., George, A. D., Lang, S., et al. (2018). Controls on shelf-margin architecture and sediment partitioning during a syn-rift to post-rift transition: Insights from the Barrow Group (Northern Carnarvon Basin, North West Shelf, Australia). *Earth-Science Reviews, 177* , 643-677.

Philpotts, A., & Asher, P. (1994). Magmatic flow-direction indicators in a giant diabase feeder dike, Connecticut. *Geology, 22* (4), 363-366.

Philpotts, A. R., & Philpotts, D. E. (2007). Upward and downward flow in a camptonite dike as recorded by deformed vesicles and the anisotropy of magnetic susceptibility (AMS). *Journal of Volcanology and Geothermal Research, 161* (1-2), 81-94.

Planke, S., Rasmussen, T., Rey, S. S., & Myklebust, R. (2005). Seismic characteristics and distribution of volcanic intrusions and hydrothermal vent complexes in the Voring and More basins. In A. G. Dore (Ed.),*Petroleum Geology: North-West Europe and Global Perspectives - Proceddings of the 6th Petroleum Geology Conference* (pp. 833-844): Geological Society, London.

Poppe, S., Holohan, E. P., Pauwels, E., Cnudde, V., & Kervyn, M. (2015). Sinkholes, pit craters, and small calderas: Analog models of depletion-induced collapse analyzed by computed X-ray microtomography. *Geological Society of America Bulletin, 127* (1-2), 281-296.

Reeve, M. T., Jackson, C. A. L., Bell, R. E., Magee, C., & Bastow, I. D. (2016). The stratigraphic record of prebreakup geodynamics: Evidence from the Barrow Delta, offshore Northwest Australia. *Tectonics, 35* (8), 1935-1968.

Reeve, M. T., Magee, C., Bastow, I. D., McDermott, C., Jackson, C. A.-L., Bell, R. E., & Prytulak, J. (2021). Nature of the Cuvier Abyssal Plain crust, offshore NW Australia. *Journal of the Geological Society* .

Robb, M. S., Taylor, B., & Goodliffe, A. M. (2005). Re-examination of the magnetic lineations of the Gascoyne and Cuvier Abyssal Plains, off NW Australia. *Geophysical Journal International, 163* (1), 42-55.

Sauro, F., Pozzobon, R., Massironi, M., De Berardinis, P., Santagata, T., & De Waele, J. (2020). Lava tubes

on Earth, Moon and Mars: A review on their size and morphology revealed by comparative planetology. *Earth-Science Reviews, 209* (103288).

Schofield, N., Stevenson, C., & Reston, T. (2010). Magma fingers and host rock fluidization in the emplacement of sills. *Geology, 38* (1), 63-66.

Scott, E. D., & Wilson, L. (2002). Plinian eruptions and passive collapse events as mechanisms of formation for Martian pit chain craters. *Journal of Geophysical Research: Planets, 107* (E4), 4-1-4-11.

Smart, K. J., Wyrick, D. Y., & Ferrill, D. A. (2011). Discrete element modeling of Martian pit crater formation in response to extensional fracturing and dilational normal faulting. *Journal of Geophysical Research: Planets, 116* (E4).

Spencer, J. R., & Fanale, F. P. (1990). New models for the origin of Valles Marineris closed depressions. *Journal of Geophysical Research: Solid Earth, 95* (B9), 14301-14313.

Stagg, H., Alcock, M., Bernardel, G., Moore, A., Symonds, P., & Exon, N. (2004). *Geological framework of the outer Exmouth Plateau and adjacent ocean basins* : Geoscience Australia.

Stagg, H., & Colwell, J. (1994). *The structural foundations of the Northern Carnarvon Basin.* Paper presented at the The sedimentary basins of Western Australia: Proceedings of Petroleum Exploration Society of Australia Symposium, Perth.

Sun, Q., Jackson, C. A.-L., Magee, C., Mitchell, S. J., & Xie, X. (2019). Extrusion dynamics of deepwater volcanoes revealed by 3-D seismic data. *Solid Earth, 10* (4), 1269-1282.

Tanaka, K., & Golombek, M. (1989). *Martian tension fractures and the formation of grabens and collapse features at Valles Marineris.*Paper presented at the Lunar and Planetary Science Conference Proceedings.

Tindale, K., Newell, N., Keall, J., & Smith, N. (1998).*Structural evolution and charge history of the Exmouth Sub-basin, northern Carnarvon Basin, Western Australia.* Paper presented at the The Sedimentary Basins of Western Australia 2: Proc. of Petroleum Society Australia Symposium, Perth, WA.

Velayatham, T., Holford, S., Bunch, M., King, R., & Magee, C. (2019).*3D Seismic Analysis of Ancient Subsurface Fluid Flow in the Exmouth Plateau, Offshore Western Australia.* Paper presented at the West Australian Basins Symposium, Perth, Western Australia.

Velayatham, T., Holford, S. P., & Bunch, M. A. (2018). Ancient fluid flow recorded by remarkably long, buried pockmark trains observed in 3D seismic data, Exmouth Plateau, Northern Carnarvon basin. *Marine and Petroleum Geology, 95* , 303-313.

Von Hagke, C., Kettermann, M., Bitsch, N., Bucken, D., Weismuller, C., & Urai, J. L. (2019). The effect of obliquity of slip in normal faults on distribution of open fractures. *Frontiers in Earth Science, 7* (18).

Wall, M., Cartwright, J., Davies, R., & McGrandle, A. (2010). 3D seismic imaging of a Tertiary Dyke Swarm in the Southern North Sea, UK.*Basin Research, 22* (2), 181-194.

Whitten, J. L., & Martin, E. S. (2019). Icelandic pit chains as planetary analogs: Using morphologic measurements of pit chains to determine regolith thickness. *Journal of Geophysical Research: Planets, 124* (11), 2983-2999.

Wyrick, D. (2004). Distribution, morphology, and origins of Martian pit crater chains. *Journal of Geophysical Research, 109* (E6).

Wyrick, D., Ferrill, D. A., Morris, A. P., Colton, S. L., & Sims, D. W. (2004). Distribution, morphology, and origins of Martian pit crater chains. *Journal of Geophysical Research, 109* (E6), E06005.

Wyrick, D. Y., Morris, A. P., Todt, M. K., & Watson-Morris, M. J. (2015). Physical analogue modelling of Martian dyke-induced deformation.*Geological Society, London, Special Publications, 401* (1), 395-403.

Yang, X.-M., & Elders, C. (2016). The Mesozoic structural evolution of the Gorgon Platform, North Carnarvon Basin, Australia. *Australian Journal of Earth Sciences, 63* (6), 755-770.

Seismic reflection data reveal the 3D subsurface structure of pit craters

Craig Magee[1], Corbin Kling[2], Paul Byrne[3], Christopher A-L Jackson[4]

[1]School of Earth Science and Environment, University of Leeds, Leeds, LS2 9JT, UK

[2]Center for Earth and Planetary Studies, Smithsonian Institution, Washington, D.C., 20560, USA

[3]Washington University in St. Louis, St. Louis, MO 63132, USA

[4]Department of Earth and Environmental Sciences, University of Manchester, Williamson Building, Oxford Road, Manchester, M13 9PL, UK

Key points

- We image and quantify the palaeosurface and subsurface 3D geometry of pit craters formed in the Late Jurassic
- Pit craters physically connected to upper tips of igneous dykes or steeply dipping, dilatational portions of normal faults
- No apparent relationship between pit crater geometry and formation mechanism

Abstract

Pit craters are enigmatic, quasi-circular depressions observed on rocky (e.g., Earth and Mars) and icy (e.g., Enceladus) planetary bodies, and numerous asteroids. These depressions are not related to meteorite impacts. Instead pit craters are thought to be generated by overburden collapse into a subsurface cavity (e.g., created by dilatational faulting), or volumetrically depleted zone (e.g., an evacuated magma reservoir or conduit). The surface size and distribution of pit craters should thus provide an important record of otherwise inaccessible subsurface processes. Because we cannot access the subsurface structure of pit craters observed on planetary surfaces, we rely on physical and numerical models to infer the subsurface processes linked to their formation. Here, we use 3D seismic reflection data to quantify the palaeosurface and subsurface geometry of pit craters. These data enable us to identify whether pit craters connect to and their formation thus related to underlying structures. We map 59, Late Jurassic pit craters deeply buried within a sedimentary basin, offshore NW Australia. We demonstrate that some pit craters extend down and appear physically connected to igneous dykes, whereas others connect to dyke-induced and tectonic faults, seemingly where faults are steeply dipping and dilatational. There are no apparent relationships between pit crater geometries (e.g., palaeosurface expression or vertical extent) and the different magmatic and fault-related mechanisms we infer drove their formation. Reflection seismology is a powerful tool for understanding how pit craters form and whether their surface expression can be used to reconstruct subsurface structures and processes on other planetary bodies.

Plain language summary

Linear chains of small craters are commonly observed on planetary bodies like Mars, Enceladus, or various asteroids. These craters, called pit craters, are not related to meteorite impacts. Based on comparison to similar craters observed on Earth and created in laboratory models, we think pit craters form because rock collapses into holes present beneath the surface. There are many suggestions for how these holes form, but all suggest their presence destabilises overlying rock, which drains into the hole and leaves a crater at the surface. We have not been able to test suggestions about how these holes form, because we cannot easily look beneath the surface of other planetary bodies. We use a technique called seismic reflection, which uses sound waves to create an ultrasound-like image of Earth's subsurface. With this technique, we image the 3D shape of pit craters found offshore Australia. These data allow us for the first time to measure what pit craters look like in the subsurface and see whether they link to any structures that could have caused their formation. We show that some pit craters are connected to igneous dykes (solidified vertical sheets of molten rock) and others to faults (cracks in the rock).

1. Introduction

Quasi-circular topographic depressions are observed on the surface of Earth and many planetary bodies and asteroids (e.g., Figs 1A and B) (e.g., Abelson et al., 2003; Ferrill et al., 2004; Ferrill et al., 2011; Frumkin & Naor, 2019; Horstman & Melosh, 1989; Kling et al., 2021; Martin et al., 2017; Okubo & Martel, 1998; Sauro et al., 2020; Scott & Wilson, 2002; Whitten & Martin, 2019; Wyrick et al., 2004). These depressions, termed 'pit craters', have diameters of meters to thousands of meters and commonly arranged in linear chains (e.g., Kling et al., 2021; Whitten & Martin, 2019). The lack of raised rims and ejecta deposits around pit craters suggest they are not formed by meteorite impacts (e.g., Figs 1A and B) (e.g., Halliday, 1998; Poppe et al., 2015; Wyrick et al., 2004). Instead, pit craters are thought to reflect collapse of overlying rock and/or regolith into subsurface cavities or volumetrically depleted zones generated by (Fig. 1C) (see also Wyrick et al., 2004): (i) the dissolution of carbonate or salt (e.g., sinkholes; Abelson et al., 2003; Poppe et al., 2015; Spencer & Fanale, 1990); (ii) local porosity reduction of the host material following hydrothermal fluid flow or fault-related overpressure release (e.g., pockmarks; Velayatham et al., 2019; Velayatham et al., 2018); (iii) evacuation of lava tubes (see Sauro et al., 2020 and references therein); (iv) opening of tensile fractures (e.g., Ferrill et al., 2011; Smart et al., 2011; Tanaka & Golombek, 1989); (v) local dilation where faults are steeply dipping (e.g., Ferrill & Morris, 2003; Ferrill et al., 2011; Ketterman et al., 2015; Kettermann et al., 2019; Smart et al., 2011; Von Hagke et al., 2019); (vi) dyke intrusion (e.g., Mège & Masson, 1996; Okubo & Martel, 1998; Scott & Wilson, 2002; Wall et al., 2010); (vii) magma migration out of a reservoir (e.g., Mège et al., 2003; Poppe et al., 2015); and/or (viii) explosive volcanism (e.g., Hughes et al., 2018).

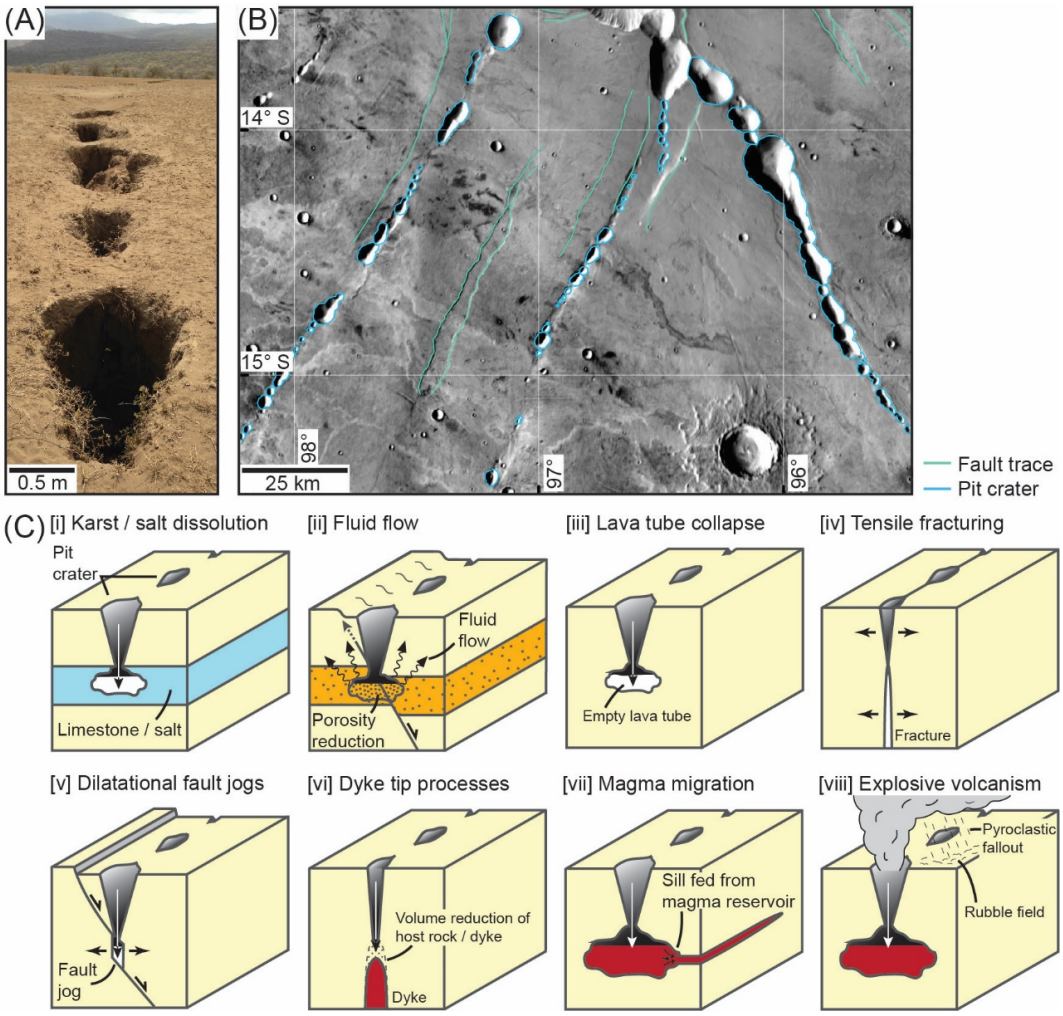

Figure 1: (A) A pit crater chain in the Natron Basin, Tanzania (Magee et al., 2019; Muirhead et al., 2015). (B) Pit crater chains and graben-bounding fault traces in the Noctis Labyrinthus area of Mars (Kling et al., 2021). Basemap is THEMIS Daytime-IR. (C) Conceptual models of pit crater formation (modified from Kettermann et al., 2019; Sauro et al., 2020; Velayatham et al., 2019; Velayatham et al., 2018; Wyrick et al., 2004).

If the surface expression of pit craters reflects their formation mechanism(s), we could use their morphology to interrogate inaccessible subsurface processes and structures on Earth, as well as other planetary bodies and asteroids (e.g., Kling et al., 2021; Korteniemi et al., 2010; Martin et al., 2017; Mège & Masson, 1997; Smart et al., 2011; Whitten & Martin, 2019). However, imaging pit craters on other worlds is difficult (Wyrick et al., 2004), and even our knowledge of the subsurface geometry of pit craters on Earth remains limited (cf. Abelson et

al., 2003; Frumkin & Naor, 2019; Halliday, 1998; Wall et al., 2010). We thus rely on physical experiments and numerical modelling to predict how pit crater formation may translate into surface deformation (e.g., Poppe et al., 2015; Smart et al., 2011). Identifying pit craters on Earth, the subsurface structure of which we *can* study, is crucial to validating these models and thus determining whether pit crater surface expressions can be used to distinguish formation mechanisms.

Reflection seismology provides unprecedented insight into Earth's subsurface and can uniquely image the three-dimensional structure of pit craters (Abelson et al., 2003; Magee et al., 2019; Magee & Jackson, 2020a; Wall et al., 2010). Here, we use seismic reflection data imaging a sedimentary basin on the Exmouth Plateau, offshore NW Australia to conduct the first-ever quantitative, 3D analysis of pit craters and their underlying structure. Seismic-stratigraphic analyses reveal the now-buried pit craters developed during a phase of Late Jurassic igneous dyking (Magee & Jackson, 2020a). Our data allow us to: (i) quantify the palaeosurface expression and subsurface structure of pit craters in 3D; and (ii) identify underlying structures that may be related to pit crater formation. Overall, we can thus test whether the (palaeo)surface expression of pit craters are diagnostic of subsurface structure and processes.

We map 59 pit craters, which typically have a funnel-like appearance comprising an upper inverted cone that is underlain by a pipe, and are commonly arranged in linear chains. Most (54) pit craters occur in chains located along the floor of 2 km wide, buried graben that are bound by dyke-induced faults and underlain by what were northwards-propagating dykes (Magee & Jackson, 2020a); five other pit craters are connect to steeply dipping portions of tectonic normal faults. The link between pit craters and dykes and faults confirms that magmatic processes and overburden collapse into dilatational fault jogs. By recognising that some pit craters above dykes occur at different stratigraphic levels and broadly get younger southwards, we specifically suggest these pit craters may have formed when a waning of magma pressure and potential backflow led to a local volume reduction of the dyke. In addition to obtaining insight into pit crater formation mechanisms, we also show that pit crater depths are variable across the study area. Pit crater depth are one of the few morphological properties of pit craters that can be measured from surficial data, and have been suggested to equal and thus be a proxy for regolith thickness on other planetary bodies (e.g., Whitten & Martin, 2019; Wyrick et al., 2004). The variability in pit crater depths we record suggest this characteristic may *not* always control regolith thickness. Overall, our work demonstrates that seismic reflection data provides a unique insight into the structure and growth of pit craters on Earth. Further seismic-based studies will help us understand extraterrestrial pit craters and, thus, probe the subsurface structure and composition of other planetary bodies for which direct, in situ data are not yet available.

1. Geological setting

The North Carnarvon Basin, offshore NW Australia (Fig. 2A) formed during periodic rifting between Australia and Greater India in the Late Carboniferous-

to-Early Cretaceous (e.g., Direen et al., 2008; Longley et al., 2002; Stagg et al., 2004). The Exmouth Plateau, where the studied pit craters are situated, lies within the North Carnarvon Basin and itself began in the Rhaetian (Late Triassic) to Callovian (Middle Jurassic) rift phase, which produced an array of ~N-striking, large-throw (up to ~1 km) normal faults (Figs 2B and C) (e.g., Bilal et al., 2018; Black et al., 2017; Gartrell et al., 2016; Marshall & Lang, 2013; Stagg & Colwell, 1994; Tindale et al., 1998). These tectonic faults displace a thick pre-rift succession, including the fluvio-deltaic Mungaroo Formation, and accommodated deposition of a relatively condensed (100 m thick), clastic-dominated, syn-rift succession (i.e. the Brigadier and North Rankin formations, the Murat Siltstone, and the Athol Formation; Figs 2B and C) (Hocking, 1992; Hocking et al., 1987; Stagg et al., 2004; Tindale et al., 1998).

The Callovian unconformity caps the Athol Formation and underlies the Oxfordian-to-Tithonian, marine Dingo Claystone, marking the end of major Late Triassic-to-Middle Jurassic rifting (Figs 2B and C) (e.g., Tindale et al., 1998; Yang & Elders, 2016). Renewed rifting in the Tithonian (Late Jurassic) to Valanginian (Early Cretaceous) involved (Figs 2B and C): (i) sub-aerial development of the regionally developed, Base Cretaceous unconformity at ~148 Ma (latest Tithonian); (ii) rapid and significant subsidence to accommodate deposition of the 3 km thick, fully marine Barrow Group; and (iii) relatively limited upper crustal faulting, which was restricted to minor reactivation of older faults and generation of an array of N-S to NE-SW striking, low-throw (<0.1 km) normal faults (e.g., Driscoll & Karner, 1998; Magee et al., 2016; Paumard et al., 2018; Reeve et al., 2016). Continental break-up occurred along the western and southern margin of the Exmouth Plateau in the Valanginian-to-Hauterivian (~135–130 Ma; Fig. 2B) (e.g., Direen et al., 2008; Reeve et al., 2021; Robb et al., 2005). Following break-up, thermal subsidence accommodated deposition of a thick post-rift succession that hosts several tiers of polygonal faults (e.g., Paganoni et al., 2019; Velayatham et al., 2019).

During the Late Jurassic, at ~148 Ma, a radial dyke swarm, up to ~170–500 km long and ~300 km wide, was emplaced across much of the Exmouth Plateau (Figs 2A and B) (Magee & Jackson, 2020a). Associated with this dyke swarm is an array of dyke-induced faults that extend up from and dip towards the upper tips of dykes, offsetting Late Triassic-to-Late Jurassic strata and bounding dyke-parallel graben (e.g., Figs 2D and 3A) (Magee & Jackson, 2020a; Magee & Jackson, 2020b). Within these graben, linear chains of sub-circular depressions are recognised (e.g., Figs 2D and 3A) (Magee & Jackson, 2020a; Velayatham et al., 2019; Velayatham et al., 2018). These depressions, which are interpreted to have formed at the contemporaneous free surface, are underlain by pipe-like features that extend down towards dykes, dyke-induced normal faults, or tectonic normal faults (e.g., Figs 2D and 3A) (Magee & Jackson, 2020a; Velayatham et al., 2019; Velayatham et al., 2018). The depressions have previously been interpreted as pockmarks formed by fluid escape from an overpressured horizon when faulting locally reduced the overburden pressure (e.g., Fig. 1B [ii]) (Velayatham et al., 2018). However, the spatial and temporal association be-

tween the depressions and underlying dykes suggests they may be analogous to pit craters observed elsewhere on Earth and other planetary bodies (Magee & Jackson, 2020a); henceforth we refer to these depressions as 'pit craters'.

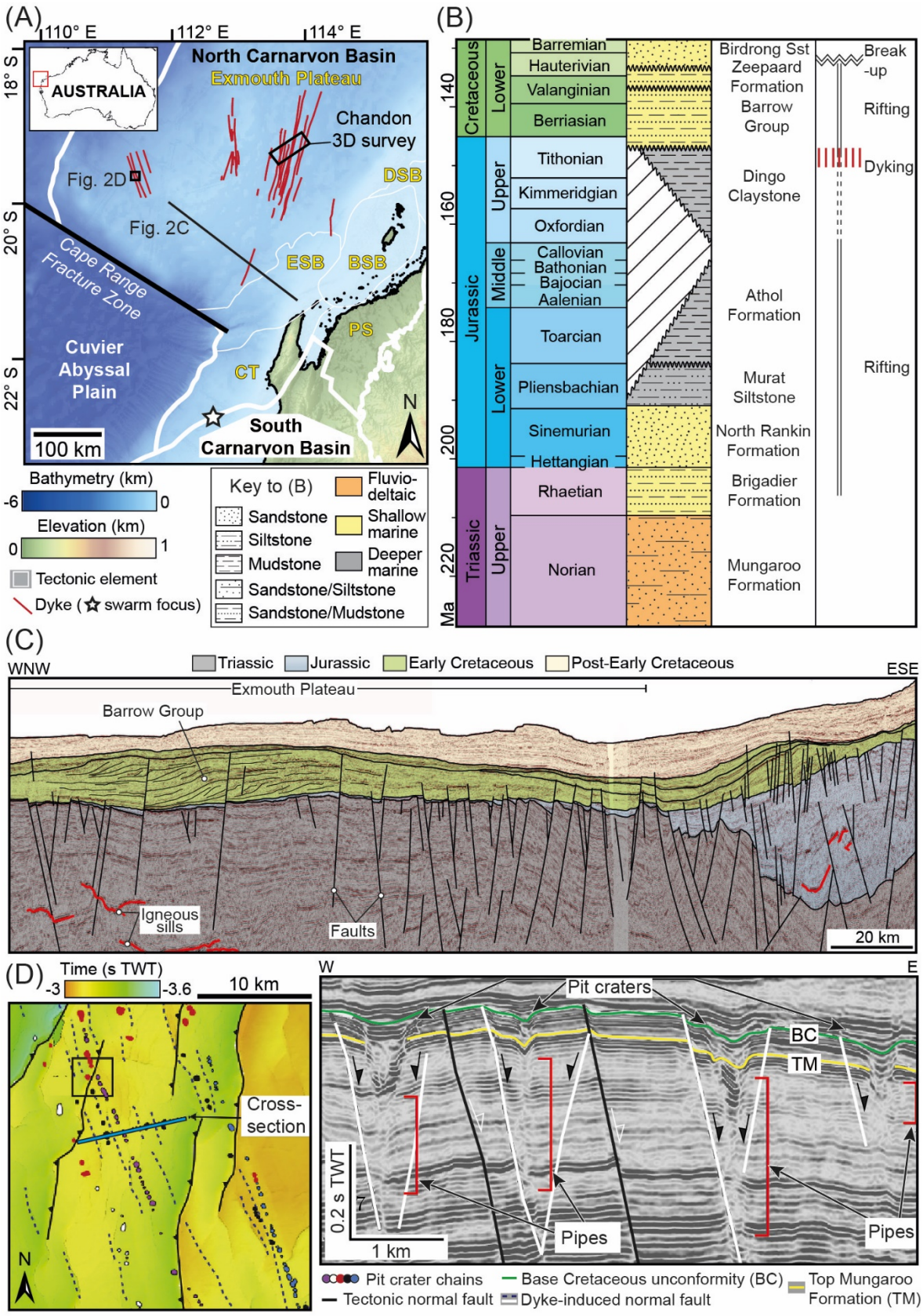
(A)
110° E
112° E
114° E
18° S
20° S
22° S
AUSTRALIA
North Carnarvon Basin
Exmouth Plateau
Chandon 3D survey
Fig. 2D
Fig. 2C
DSB
ESB
BSB
PS
CT
Cape Range Fracture Zone
Cuvier Abyssal Plain
South Carnarvon Basin
100 km
N
Bathymetry (km)
-6
0
Elevation (km)
0
1
Tectonic element
Dyke (☆ swarm focus)
Key to (B)
Sandstone
Siltstone
Mudstone
Sandstone/Siltstone
Sandstone/Mudstone
Fluvio-deltaic
Shallow marine
Deeper marine
(B)
Ma
140
160
180
200
220
Cretaceous
Lower
Jurassic
Upper
Middle
Lower
Triassic
Upper
Barremian
Hauterivian
Valanginian
Berriasian
Tithonian
Kimmeridgian
Oxfordian
Callovian
Bathonian
Bajocian
Aalenian
Toarcian
Pliensbachian
Sinemurian
Hettangian
Rhaetian
Norian
Birdrong Sst
Zeepaard Formation
Barrow Group
Dingo Claystone
Athol Formation
Murat Siltstone
North Rankin Formation
Brigadier Formation
Mungaroo Formation
Break-up
Rifting
Dyking
Rifting
(C)
WNW
ESE
Triassic
Jurassic
Early Cretaceous
Post-Early Cretaceous
Exmouth Plateau
Barrow Group
Igneous sills
Faults
20 km
(D)
Time (s TWT)
-3
-3.6
10 km
Cross-section
N
W
E
Pit craters
BC
TM
0.2 s TWT
1 km
Pipes
Pipes
Pit crater chains
Base Cretaceous unconformity (BC)
Top Mungaroo Formation (TM)
Tectonic normal fault
Dyke-induced normal fault

Figure 2: (A) Map of the southern portion of the North Carnarvon Basin highlighting principal tectonic elements, including the: ESB = Exmouth Sub-basin, CT = Carnarvon Terrace, BSB = Barrow Sub-basin, DSB = Dampier Sub-basin, and PS = Peedamullah Shelf. The location of the Exmouth Dyke Swarm is also shown (Magee & Jackson, 2020a). Elevation data are based on the 2009 Australian Bathymetry and Topography grid (Geoscience Australia). Inset: Location map of the North Carnarvon Basin (NCB) relative to Australia. (B) Stratigraphic column for the Exmouth Plateau summarising the age, dominant lithology, and generalised depositional environment for key units (after Hocking et al., 1987; Partington et al., 2003; Tindale et al., 1998). Key tectonics and magmatic events are also shown for (see Reeve et al., 2021 and references therein). (C) Interpreted seismic section, showing generalised stratigraphic architecture of the Exmouth Plateau and Exmouth Sub-basin (modified from Reeve et al., 2016). See Figure 2A for location. (D) Interpreted time-structure map and seismic section showing pit crater-like features arranged in chains and associated with normal faults in the western portion of the Exmouth Plateau (modified from Velayatham et al., 2018). See Figure 2A for map location.

1. Dataset and Methods

The zero-phase, time-migrated Chandon 3D seismic reflection survey covers an area of ~951 km^2, has a bin spacing of 25 m, and a record length of 6 seconds two-way time (s TWT). We present seismic images where a trough (black) reflection has a positive polarity and corresponds to a downward increase in acoustic impedance, and a peak (white) reflection has a negative polarity and represents a downward decrease in acoustic impedance (e.g., Fig. 3A). To help identify and map the pit craters, their underlying dykes, and spatially associated faults, we extract a variance volume attribute; this accentuates spatial variations in waveform similarity (e.g., Chopra & Marfurt, 2005; Marfurt & Alves, 2015).

We use data from five boreholes (Chandon-1, Chandon-2, Chandon-3, Mercury-1, and Yellowglen-1) within the survey area to establish estimates for: (i) the age and intervening lithology of three mapped stratigraphic horizons, which correspond to the Top Mungaroo Formation (TM; ~209 Ma), Top Athol Formation (TA; ~164 Ma), and Base Cretaceous unconformity (BC; ~148 Ma); (ii) an average time-depth relationship for the subsurface (see Supporting Figure 1), allowing us to depth-convert (from ms TWT to metres) measurements taken from the top 4 s TWT of the survey; and (iii) the seismic velocity (v) range of the interval of interest within which the pit craters are imaged. Seismic velocity increases with depth, from 2.64(±10%) km s^{-1} to 3.66(±10%) km s^{-1}, as the dominant frequency (f) of the data broadly decreases from ~33 Hz to ~23 Hz; with these data we calculate the wavelength ($\lambda = v/f$) of the data and estimate that its vertical seismic resolution can be characterised by limits of separability ($\lambda/4$) of 37(±7)–17(±3) m and limits of visibility ($\lambda/30$) of 5(±1)–3(±1) m (e.g., Brown, 2011). The limits of separability and visibility correspond to the minimum vertical distance between two features required for them to be imaged, respectively, as: (i) two discrete reflections; and (ii) a tuned reflection pack-

age, created by convolution of the two reflections on their return to the surface (Brown, 2011). The horizontal resolution of the time-migrated seismic reflection data is estimated to be at least 25 m, which is equivalent to the bin spacing, and likely increases to 37(±7) m (i.e. /4) with depth.

1. ***Plan-view measurements***

We identify 59 pit craters that we label A*n*–I*n* if they overlie a dyke, with A–I corresponding to the dyke name (Magee & Jackson, 2020a; Magee & Jackson, 2020b), or *Xn* if they appear spatially related to tectonic normal faults; *n* denotes the pit crater number, which increases along each chain from south to north. We map the plan-view outline of each pit crater at: (i) their uppermost expression in the seismic reflection data; and (ii) where they intersect the Top Athol Formation; this allows us to characterise how pit crater plan-view morphology changes with depth. For each mapped pit crater outline, we use image analysis software (ImageJ) to define a best-fit ellipse and centroid position; where pit craters appear to have merged, we define an encompassing best-fit ellipse but manually determine centroid positions (Fig. 3B). We use the outline of each pit crater, or merged pit craters, to measure their area and the best-fit ellipses to determine their long axis lengths and azimuths, and short axis lengths (Fig. 3B). From these values, we calculate the aspect ratio of the pit crater long and short axes.

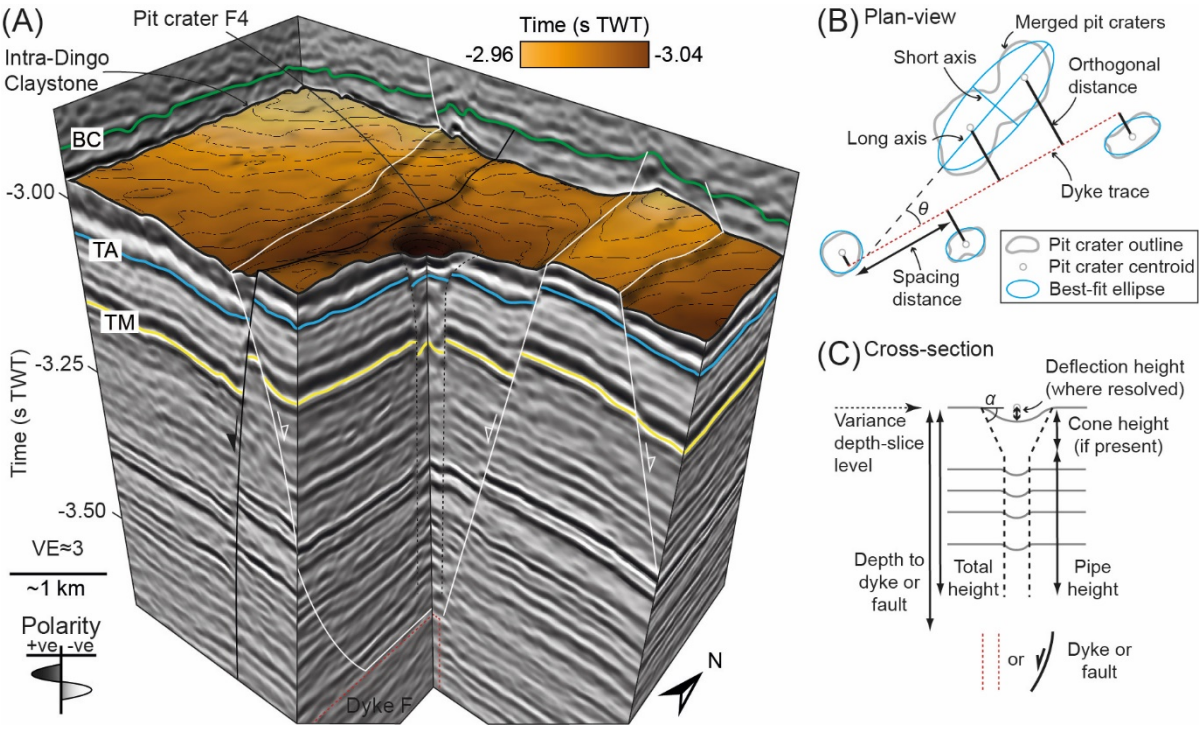

Figure 3: (A) 3D view of a funnel-like pit crater (F4), the top of which occurs

at a horizon between the Base Cretaceous unconformity (BC) and Top Athol Formation (TA) (Magee & Jackson, 2020a). The pit crater occurs with a graben and extends down to the top of Dyke F, below the Top Mungaroo Formation (TM). (B and C) Schematics showing the measurements of pit crater plan-view (B) and cross-sectional (C) morphologies.

1. ***Cross-section measurements***

The only cross-section attributes commonly available to measure for most pit craters on Earth and other planetary bodies are the depth and slope; together these can be used to estimate volume, of their surface expression (e.g., Gwinner et al., 2012; Sauro et al., 2020; Scott & Wilson, 2002; Wyrick et al., 2004). Most (54; i.e. 92%) pit craters we study display a funnel-like morphology, comprising an upper, inwardly inclined conical surface, which we refer to as an 'inverted cone', underlain by a sub-vertical cylindrical 'pipe' (e.g., Fig. 3A). Some pit craters lack an inverted cone and we refer to their morphology as pipe-like. Stratigraphic reflections within many of the inverted cone sections appear continuous with in the flanking host rock, although they are often locally deflected downwards within the pit crater (e.g., Fig. 3C). Note that for some pit craters it is difficult to correlate internal and external stratigraphic reflections. Where possible, we measure both the maximum 'cone height' and 'deflection height' of pit craters (Fig. 3C). By integrating these measurements with those of pit crater long axis lengths, we estimate slopes and volumes of the inverted cone sections and deflected reflections, assuming they are axisymmetric (Fig. 3C) (Wyrick et al., 2004). We also measure 'pipe height', which for funnel-like pit craters we define as the vertical distance from the base of inverted cones down to where the pit crater structure is no longer seismically resolved (Fig. 3C). We calculate pipe volume from the pipe height and the pit crater long axis length as measured at the Top Athol Formation. To aid comparison between pit craters with and without a funnel-like morphology, we describe each as having a 'total height'; for pipe-like pit craters their total height is equal to pipe height, but for funnel-like pit craters their total height includes the cone height and pipe height (e.g., Fig. 3C). Our measured pipe and total heights are minimum estimates as a reduction in imaging with depth and the presence of other structures (e.g., faults), limits our ability to determine the true base of pit craters (Velayatham et al., 2019; Velayatham et al., 2018; Wall et al., 2010). We measure the depth of dykes or normal faults directly beneath the top of each pit crater (Fig. 3C).

1. ***Sources of error***

The primary error source in our study relates to uncertainty in the seismic velocities used to depth-convert the seismic data from seconds two-way time to depth in metres. For example, our depth conversion assumes that seismic velocities do not vary laterally across the study area. The similarity in the time-depth relationships for all four boreholes wells within the Chandon 3D survey supports our assumption that there is little lateral variation in seismic velocity (Supporting Fig. 1), but we conservatively consider that calculated velocities and measured dominant frequencies may vary by up to $\pm 10\%$ (Magee & Jackson,

2020a). Measurements of limits of separability and visibility, deflection height, cone height, pipe height, and the depth to underlying dykes thus have assumed depth conversion-related errors of ±10%. Manual mapping and measurement can introduce human errors (e.g., in defining pit crater pipe bases) that cannot be quantified; however, we consider that these errors may be up to ±5% (Magee & Jackson, 2020a). Overall, plan-view measurements are presented with ±5% errors as they do not require depth-conversion, but may be susceptible to human error. For measurements of pit height, cone height, pipe height, and the depth to underlying dykes, we estimate cumulative errors of ±15%; this based on the uncertainty in calculated seismic velocities and potential human errors.

1. **Results**

   (a) ***Stratigraphic and structural framework***

Stratigraphic reflections within the interval of interest typically have a moderate amplitude and laterally continuous character (Fig. 4A). In places these reflections are: (i) offset by ~N-striking, linear-to-curvilinear, moderate-to-high throw (up to ~500 m) tectonic normal faults (e.g., Figs 4A-D); (ii) cross-cut by sub-vertical, ~N-trending dykes (named A to I) that are expressed as >100 m wide zones of disrupted, low-amplitude reflections (Figs 4A and E); (iii) displaced by graben-bounding, low-throw (0.1 km), dyke-induced normal faults that dip towards and converge upon the upper tips of the underlying dykes at depths of ~3–3.5 km (Fig. 4A); or (iv) intersected by pit craters (see below) (Figs 3A and 4A). Below the Base Cretaceous unconformity, pit craters and dykes are marked by high variance, as are areas where strata are folded and/or offset by tectonic faults (e.g., Fig. 4A).

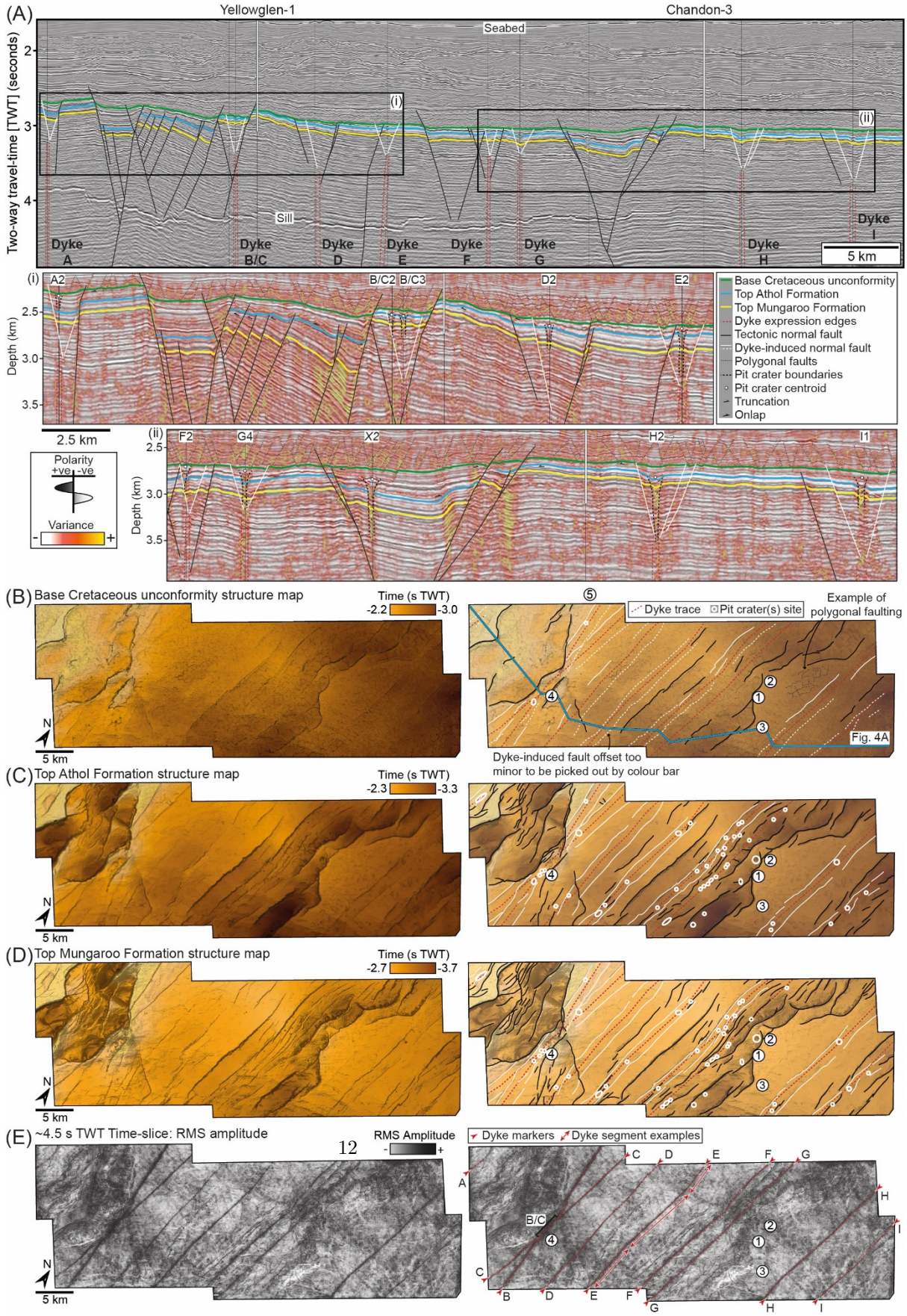
(A)
Yellowglen-1
Chandon-3
Seabed
Two-way travel-time [TWT] (seconds)
(i)
(ii)
Sill
Dyke A
Dyke B/C
Dyke D
Dyke E
Dyke F
Dyke G
Dyke H
Dyke I
5 km
Depth (km)
A2
B/C2
B/C3
D2
E2
F2
G4
X2
H2
I1
2.5 km
Polarity
+ve -ve
Variance
Base Cretaceous unconformity
Top Athol Formation
Top Mungaroo Formation
Dyke expression edges
Tectonic normal fault
Dyke-induced normal fault
Polygonal faults
Pit crater boundaries
Pit crater centroid
Truncation
Onlap
(B) Base Cretaceous unconformity structure map
Time (s TWT)
-2.2
-3.0
N
5 km
Dyke trace
Pit crater(s) site
Example of polygonal faulting
Fig. 4A
Dyke-induced fault offset too minor to be picked out by colour bar
(C) Top Athol Formation structure map
-2.3
-3.3
(D) Top Mungaroo Formation structure map
-2.7
-3.7
(E) ~4.5 s TWT Time-slice: RMS amplitude
RMS Amplitude
Dyke markers
Dyke segment examples

Figure 4: (A) Interpreted composite section capturing the tectono-stratigraphy of the area, intersecting all dykes (A-I) and revealing the structure some dyke-induced normal faults and pit craters. The line also intersects the Yellowglen-1 and Chandon-3 boreholes. The time-migrated data is shown in the top panel, and in the lower panels we show selected depth-converted, reflectivity data overlain by a variance attribute. See Figure 4B for line location. (B-C) Time-structure maps of the three major horizons (Base Cretaceous unconformity, Top Athol Formation, and Top Mungaroo Formation) interpreted in Figure 4A. Uninterpreted and interpreted versions of the maps are shown, highlighting underlying dyke traces, faults, and boreholes. The boreholes shown are: 1 = Chandon-1; 2 = Chandon-2; 3 = Chandon-3; 4 = Yellowglen-1; and 5 = Mercury-1. (E) Uninterpreted and interpreted RMS (root-mean squared) amplitude time-slice at 4.5 seconds two-way time (TWT) showing the seismic expression of dykes A-I. For part of their length, dykes B and C merge and we cannot determine if both dykes are continuous, or if one cross-cuts and displaces the other.

1. ***Pit crater morphology***

Pit craters occur across the dataset, primarily arranged in chains aligned parallel to and occurring within dyke-induced graben (Fig. 5). Five pit craters (*X1–X5*) are located outside these graben and are instead situated in the hanging wall of tectonic normal faults (Fig. 5). Of the 54 pit craters within dyke-induced graben, 50 have a funnel-like morphology in cross-section, as do four of the pit craters associated with tectonic normal faults (Figs 5-8). The remaining four pit craters within dyke-induced graben (A4, F5, G7, and H1), as well as *X3*, have a pipe-like geometry and no inverted cone section (Figs 5-8).

At the Top Athol Formation, we mapped 61 pit craters (Fig. 5); three pit craters observed at this structural level merge (e.g., E1a and b, F10a and b, G10a and b; Figs 6E, 7A, and B) and one splits (G2/3; Fig. 8B) at shallower depths. Of the 57 pit craters within dyke-induced graben at the Top Athol Formation, 30 occur directly above dyke traces and 27 have centroids situated ~75–653 m orthogonally from the associated dyke trace (Fig. 5C). The only pipe-like pit crater located directly above a dyke trace is A4 (Fig. 5).

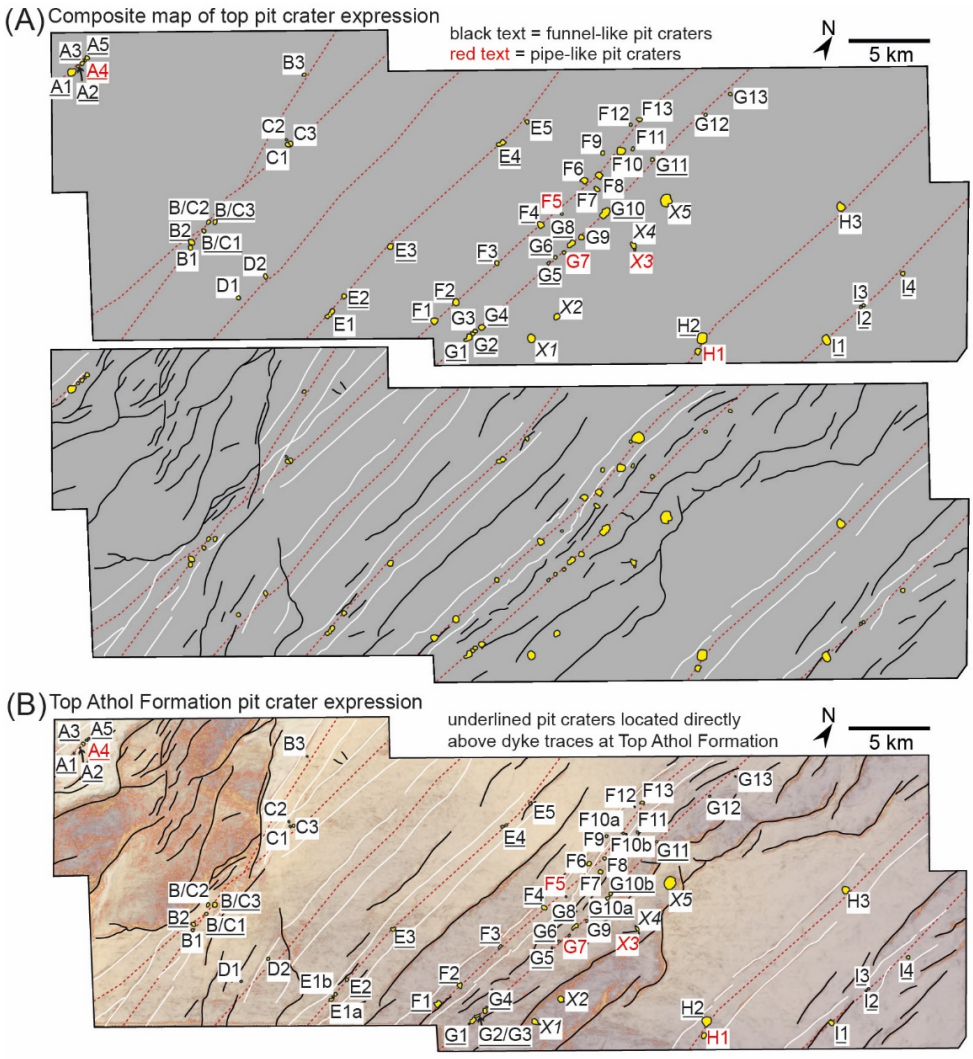

Figure 5: (A) Composite map showing the outlines of each pit crater at the shallowest stratigraphic level they occur at, relative to dyke and fault traces. (B) Map showing the expression of each pit crater at the Top Athol Formation.

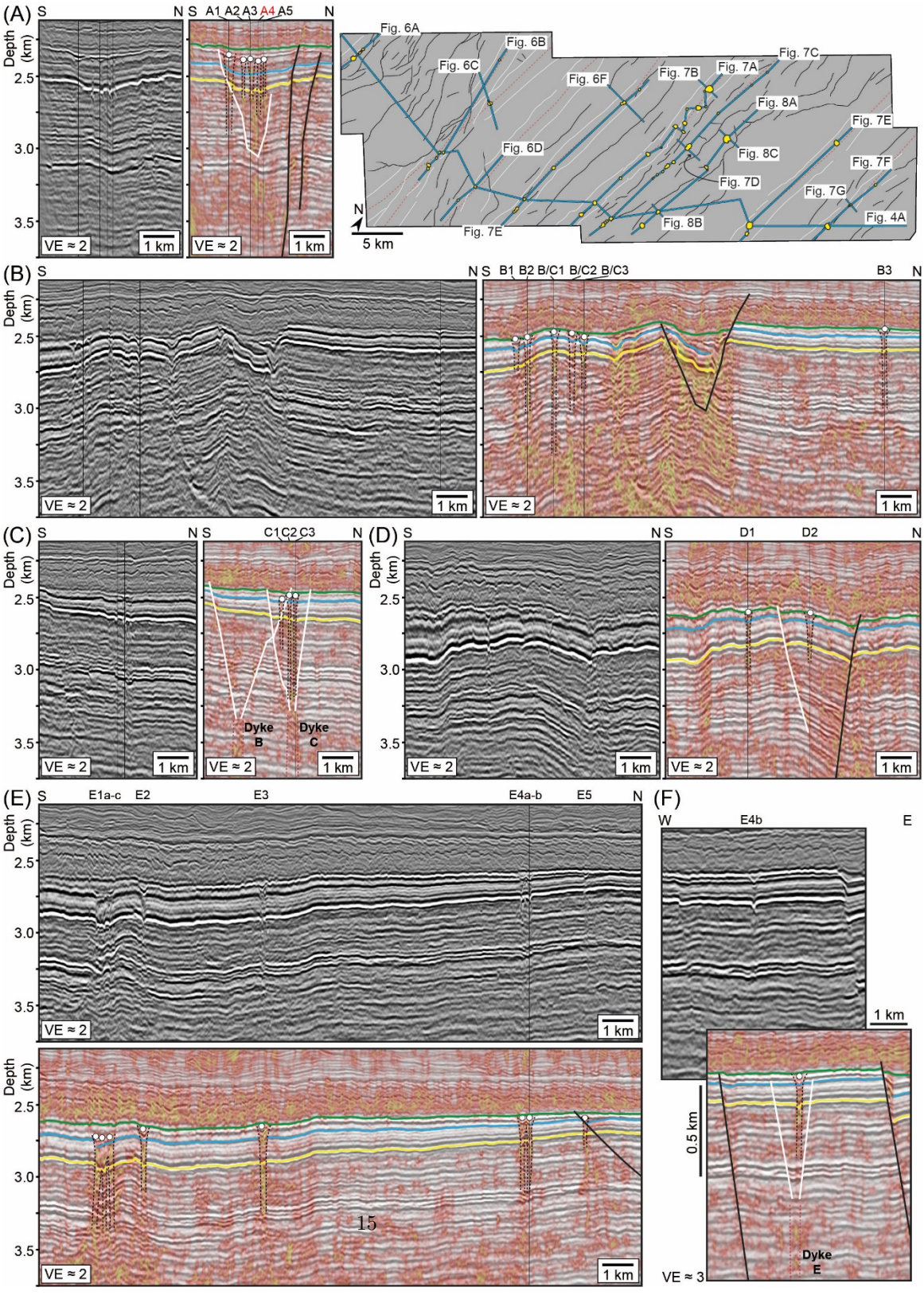
(A)
S
N
S
A1 A2 A3 A4 A5
N
Depth (km)
2.5
3.0
3.5
VE ≈ 2
1 km
VE ≈ 2
1 km
Fig. 6A
Fig. 6B
Fig. 6C
Fig. 6F
Fig. 7B
Fig. 7A
Fig. 7C
Fig. 8A
Fig. 7E
Fig. 6D
Fig. 8C
Fig. 7F
Fig. 7D
Fig. 7G
Fig. 4A
Fig. 8B
Fig. 7E
N
5 km
(B)
S
N
S
B1 B2 B/C1 B/C2 B/C3
B3
N
Depth (km)
2.5
3.0
3.5
VE ≈ 2
1 km
VE ≈ 2
1 km
(C)
S
N
S
C1 C2 C3
N
Depth (km)
2.5
3.0
3.5
VE ≈ 2
1 km
Dyke B
Dyke C
VE ≈ 2
1 km
(D)
S
N
S
D1
D2
N
Depth (km)
2.5
3.0
3.5
VE ≈ 2
1 km
VE ≈ 2
1 km
(E)
S
E1a-c
E2
E3
E4a-b
E5
N
Depth (km)
2.5
3.0
3.5
VE ≈ 2
1 km
Depth (km)
2.5
3.0
3.5
VE ≈ 2
1 km
(F)
W
E4b
E
1 km
0.5 km
Dyke E
VE ≈ 3

Figure 6: (A-F) Uninterpreted and interpreted, depth-converted seismic sections showing the structure of pit craters associated with dykes A-E. See Figure 4 for interpreted section key. VE = vertical exaggeration Inset: map showing line locations.

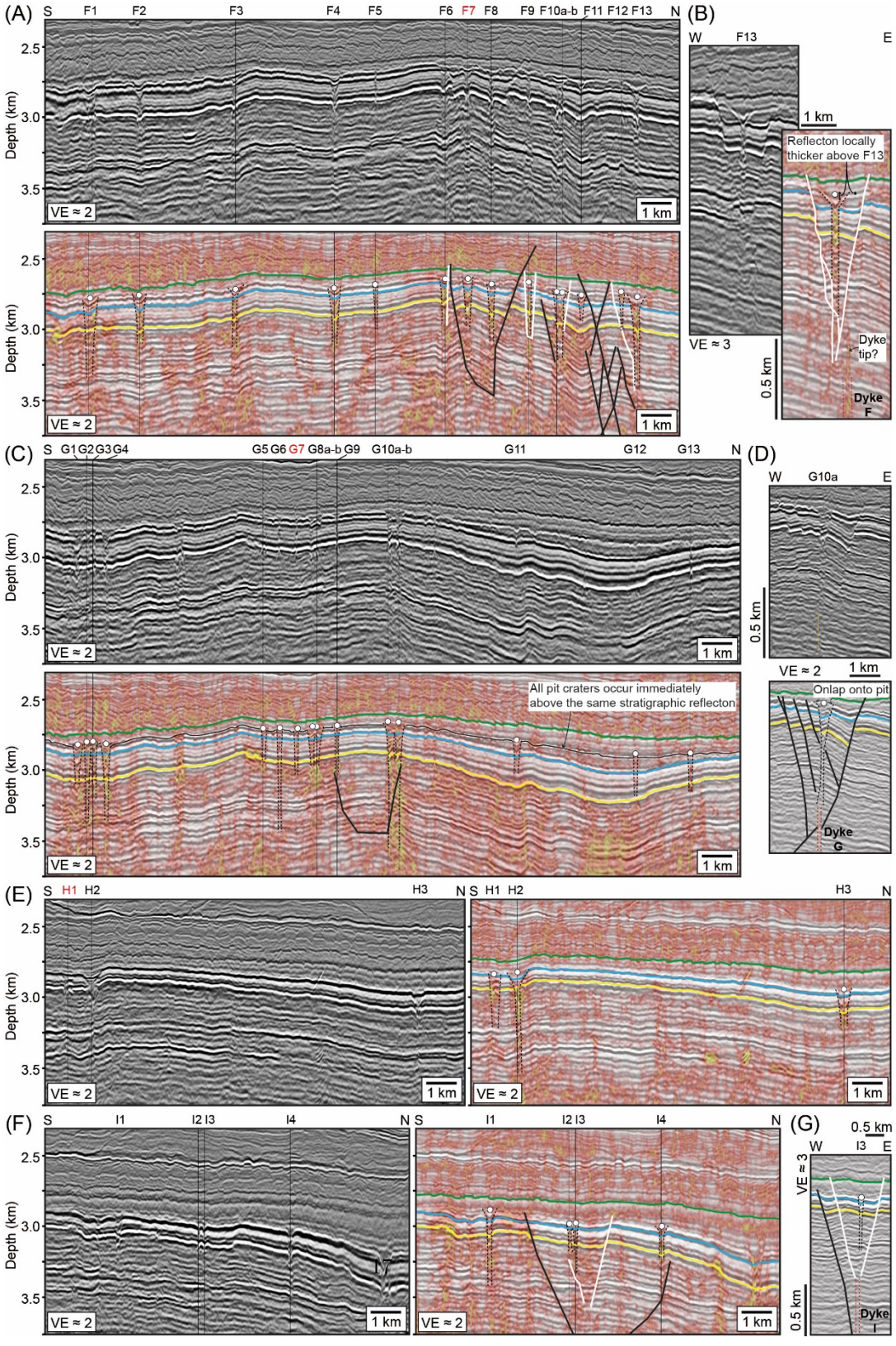
(A)
S
F1
F2
F3
F4
F5
F6
F7
F8
F9
F10a-b
F11
F12
F13
N
Depth (km)
2.5
3.0
3.5
VE ≈ 2
1 km
(B)
W
F13
E
1 km
Reflecton locally thicker above F13
VE ≈ 3
0.5 km
Dyke tip?
Dyke F
(C)
S
G1
G2
G3
G4
G5
G6
G7
G8a-b
G9
G10a-b
G11
G12
G13
N
All pit craters occur immediately above the same stratigraphic reflecton
(D)
W
G10a
E
0.5 km
VE ≈ 2
1 km
Onlap onto pit
Dyke G
(E)
S
H1
H2
H3
N
(F)
S
I1
I2
I3
I4
N
I7
(G)
0.5 km
W
I3
E
VE ≈ 3
0.5 km
Dyke I

Figure 7: (A-G) Uninterpreted and interpreted, depth-converted seismic sections showing the structure of pit craters associated with dykes F-I. See Figure 4 for interpreted section key and Figure 7 for line locations.

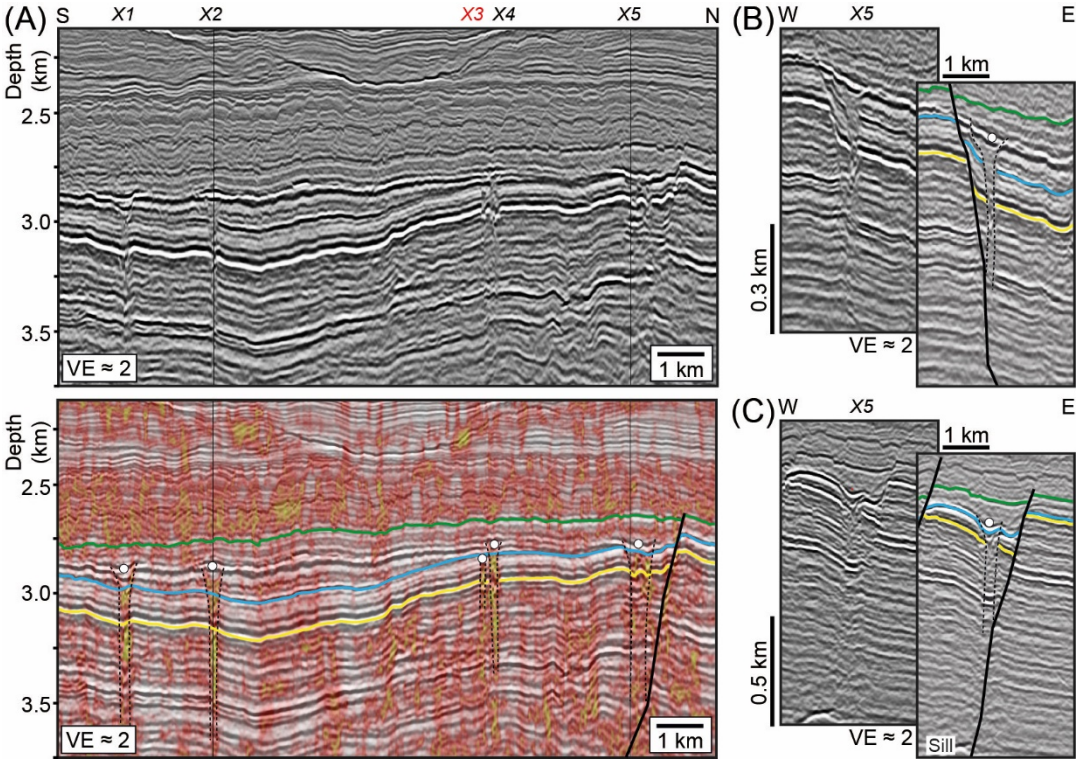

Figure 8: (A-C) Uninterpreted and interpreted, depth-converted seismic sections showing the structure of pit craters (X1-X5) associated with tectonic normal faults. See Figure 4 for interpreted section key and Figure 7 for line locations.

1. *Plan-view geometry*

Within dyke-induced graben, funnel-like pit crater tops have long axes of 150–740 m, areas of 0.05–1.24 km^2, and are quasi-circular to elliptical with aspect ratios of 1.04–3.05 (Fig. 9A; Supporting Table 1). The orientation of these pit crater long axes is variable, with a mean axis trend of 080° and a mode of 005–015° (Fig. 9B). At the Top Athol Formation, typically located below inverted cone sections, the pipes of these funnel-like pit craters are smaller in plan-view: long axis lengths are 108–585 m, aspect ratios are 1.01–3.14, and areas are 0.02–0.10 km^2 (Figs 9A and C; Supporting Table 1). For pipe-like pit craters within dyke-induced graben, their plan-view outlines at their tops are characterised by long axes of 170–390 m with no clear alignment, aspect ratios of 1.23–1.63, and areas of 0.06–0.39 km^2 (Figs 9A and C; Supporting Table 1). At the Top Athol Formation, pipe-like pit crater long axes within dyke-induced graben are 117–364 m, have aspect ratios of 1.22–1.47, and have areas of 0.04–0.32 km^2

(Figs 9A and C; Supporting Table 1).

The area and aspect ratio of the 29 pit craters situated directly above dykes broadly decrease ($R^2 = 0.55$) and seemingly increase ($R^2 = 0.29$) with depth, respectively, and tend to be larger than those above dyke-induced faults (Figs 9A, C, and D). Although the 29 pit craters above dykes cumulatively have a mean long axis orientation of 077°, six are oriented between 005–015°, sub-parallel to the mean axis (011°) of dyke segments in the study area (Fig. 9B). The size and shape of the 25 pit craters above dyke-induced faults varies non-systematically with depth; i.e. the correlation between area and aspect ratios measured at the pit crater tops and at the structurally deeper Top Athol Formation are $R^2 = 0.26$ and $R^2 = 0.08$, respectively (Figs 9A, C, and D).

Pit craters with a funnel-like morphology, but associated with tectonic normal faults (*X1*, *X2*, *X4*, and *X5*), are typically larger than those within dyke-induced graben and have long axes of 400–740 m, aspect ratios of 1.17–1.55, and areas of 0.33–1.47 km^2 at their tops (Fig. 9A; Supporting Table 1). At the Top Athol Formation, these funnel-like pit craters have long axes of 358–790 m, aspect ratios of 1.10–2.24, and areas of 0.18–1.66 km^2 (Fig. 9; Supporting Table 1). The only pit crater associated with a tectonic normal fault that does not have a funnel-like morphology (*X3*) is 140 m long, has an aspect ratio of 1.3, and an area of 0.05 km^2 at its top (Fig. 9A; Supporting Table 1). At the Top Athol Formation, this pipe-like pit crater is 98 m long, has an aspect ratio of 1.6, and an area of 0.02 km^2 (Fig. 9A; Supporting Table 1). Of the pit craters above tectonic faults, some increase in area or aspect ratio with depth, whereas others decrease (Figs 9C and D). There is no preferred orientation of pit crater long axes above tectonic faults (Fig. 9B).

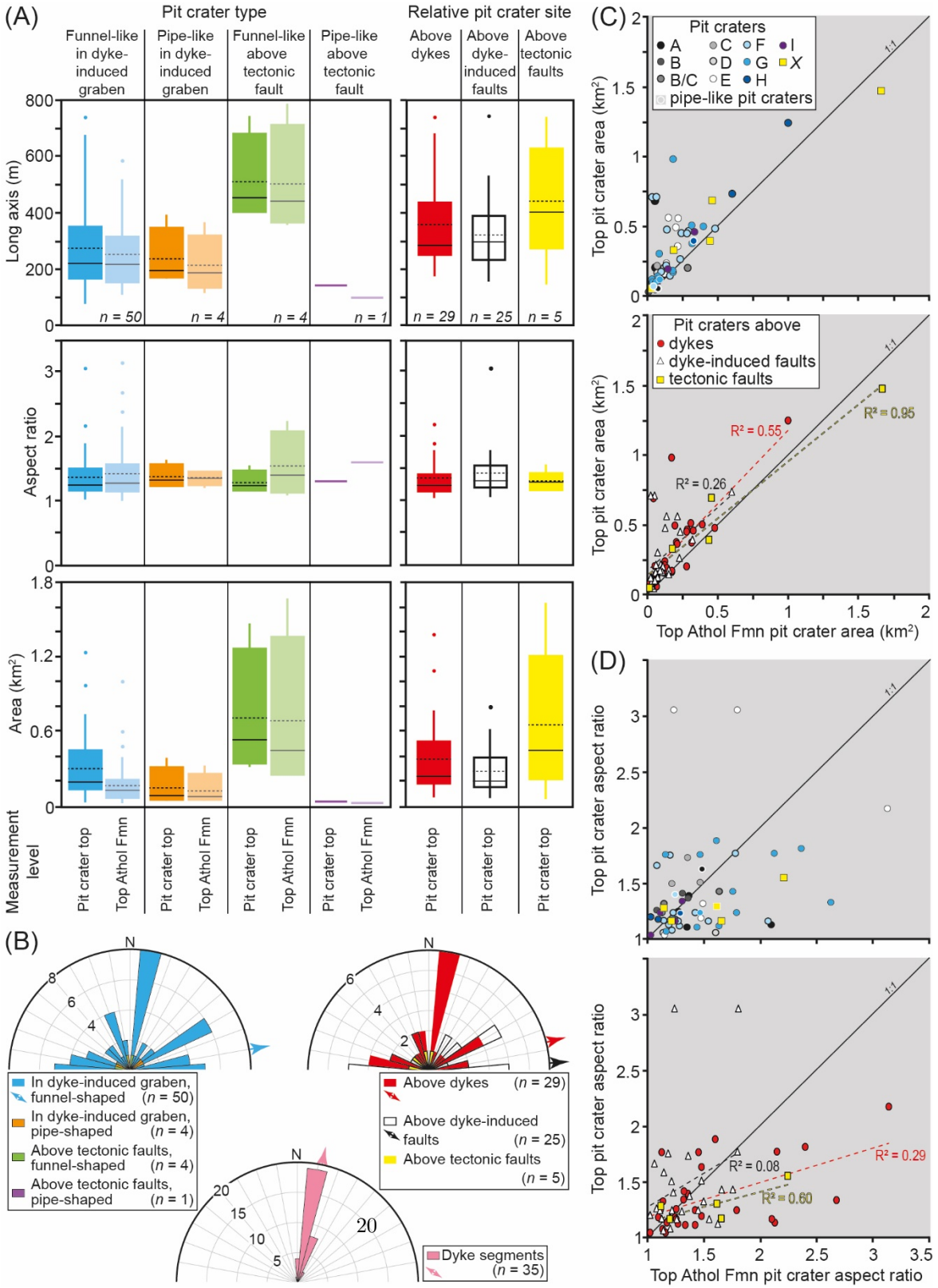
(A)
Pit crater type
Relative pit crater site
Funnel-like in dyke-induced graben
Pipe-like in dyke-induced graben
Funnel-like above tectonic fault
Pipe-like above tectonic fault
Above dykes
Above dyke-induced faults
Above tectonic faults
Long axis (m)
Aspect ratio
Area (km²)
n = 50
n = 4
n = 4
n = 1
n = 29
n = 25
n = 5
Measurement level
Pit crater top
Top Athol Fmn
(B)
In dyke-induced graben, funnel-shaped (n = 50)
In dyke-induced graben, pipe-shaped (n = 4)
Above tectonic faults, funnel-shaped (n = 4)
Above tectonic faults, pipe-shaped (n = 1)
Above dykes (n = 29)
Above dyke-induced faults (n = 25)
Above tectonic faults (n = 5)
Dyke segments (n = 35)
(C)
Pit craters
A
B
B/C
C
D
E
F
G
H
I
X
pipe-like pit craters
Pit craters above
dykes
dyke-induced faults
tectonic faults
1:1
R² = 0.55
R² = 0.26
R² = 0.95
Top pit crater area (km²)
Top Athol Fmn pit crater area (km²)
(D)
Top pit crater aspect ratio
Top Athol Fmn pit crater aspect ratio
R² = 0.08
R² = 0.60
R² = 0.29

Figure 9: (A) Box and whisker plots comparing the long axes, aspect ratios, and areas of pit craters measured at two stratigraphic levels, distinguishing those that have different geometries (i.e. funnel-like and pipe-like) and/or associated with different structures (i.e. dykes, dyke-induced faults, and tectonic faults) (Supporting Table 1). n = number. The plots also highlight data median (thin black line), mean (dashed black line), and outliers. See Figure 3B for explanation of measured parameters. (B) Rose plots showing the orientation of pit crater long axes, grouped based on their morphology and/or association with different structures (Supporting Table 1). Arrows show the mean vector of select populations. Orientation of dyke segments is also shown (Magee & Jackson, 2020a). (C and D) Graphs comparing the area (C) and aspect ratio (B) of pit crater expressions at their tops and at the Top Athol Formation. Two plots are provided for area and aspect ratio comparison, with one grouping the data based on the associated dyke or tectonic faults, and the other highlighting different between pit craters located directly above dykes, dyke-induced faults, and tectonic faults.

1. *Cross-section geometry*

In cross-section, pit crater walls typically bound zones within which stratigraphic reflections locally have a lower amplitude and are deflected (e.g., E4b) or displaced (e.g., F13) downwards relative to those in the flanking host rock (Figs 4A, 6-8). Pit crater centroids typically occur within the Dingo Claystone, ~16–188 m (i.e. 0.5–5.5 seismic cycles where one cycle is a peak and trough pair) beneath the Base Cretaceous unconformity (Figs 4A, 6-8, 10A, and B). Only B1-B3 and D1-D2 are expressed at the Base Cretaceous unconformity (Fig. 10A). Stratigraphic reflections overlying some pit craters appear locally thickened (e.g., F13; Fig. 7B) whereas others seem to onlap onto crater walls (e.g., G10a; Fig. 7D).

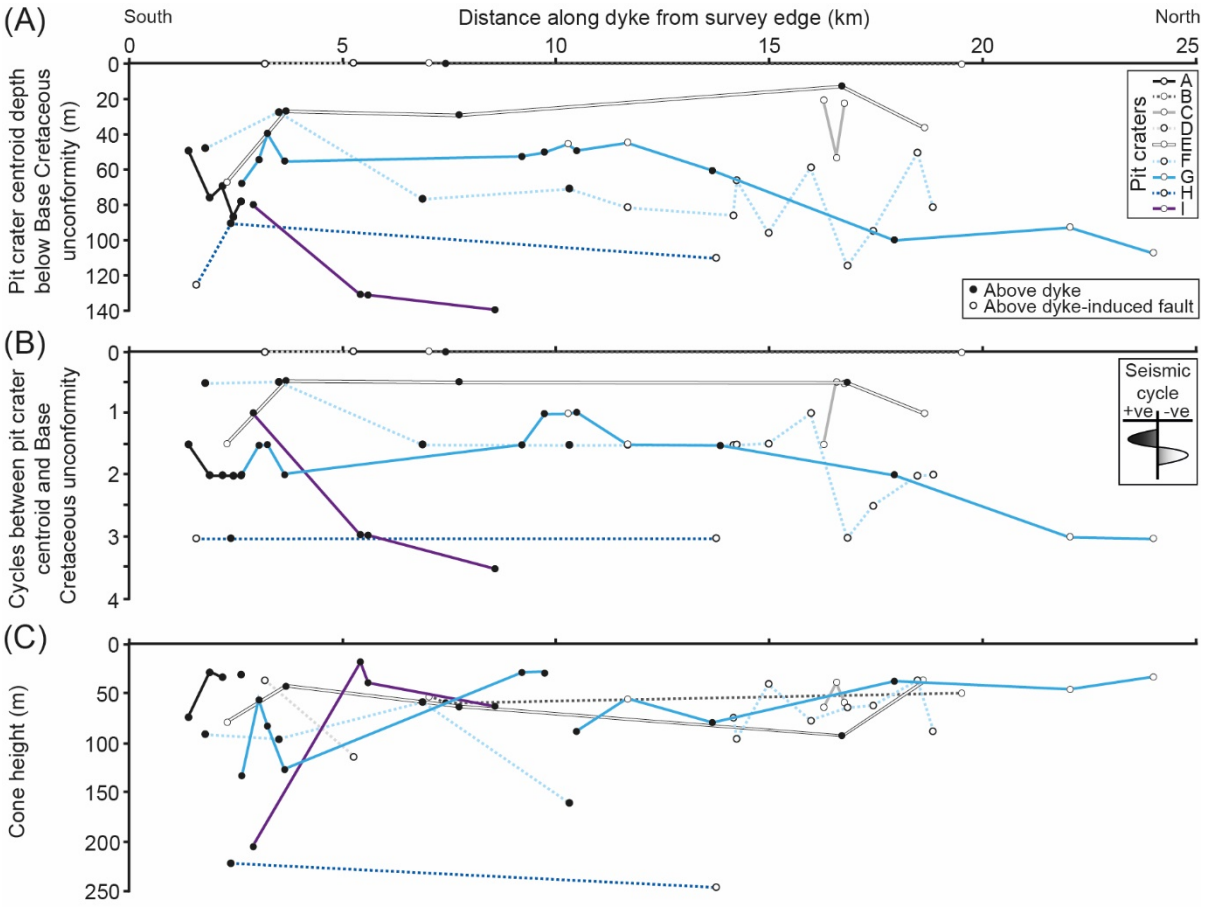

Figure 10: (A and B) Plots showing how deep (A) or how many seismic cycles (B) pit crater centroids are beneath the Base Cretaceous unconformity along dyke-strike (Supporting Table 1). Inset into (B): schematic depicting what constitutes a seismic cycle. (C) Plot of cone height along dyke strike (Supporting Table 1). See Figure 3B for explanation of measured parameters.

For each pit crater chain situated within dyke-induced graben, the depth of their pit crater centroids beneath the Base Cretaceous unconformity varies by 60 m along their length (Fig. 10A). Several pit crater chains (A, D, F, G, and I) show a broad northwards increase in centroid depth (Fig. 10A). Above some dykes, pit crater centroids all occur along the same stratigraphic reflection (i.e. D and G), even though the number of cycles between their level and the Base Cretaceous unconformity may vary (i.e., the post-overburden varies in thickness over a length-scale longer than that of an individual crater or chain of craters Figs 6D, 7B, and 10B). For other chains, pit crater centroids coincide with different (deeper or shallower) reflections along their length (i.e. A, B, C, E, F, H, and I; Figs 6, 7, and 10B). The pit craters associated with tectonic normal

faults have centroids that occur at the same stratigraphic reflection above the Top Athol Formation, except for *X3* which is the only pit crater to terminate below the Top Athol Formation (Fig. 8).

The total height of the pit craters varies across the data, with most extending down into the Mungaroo Formation (Figs 4A and 6-8); pit craters G5, G11, and G12 appear to terminate at or above the Top Mungaroo Formation (Fig. 7C). Our measurements show pit crater total height ranges from 114–868 m (Supporting Table 1). In places, mapped bases of pit crater pipes coincide with the upper tips of underlying dykes (G2, G4, G6, G10a, G12, and H2) or dyke-induced fault planes (B/C2, C2, C3, F9, F13, I2, and I3) (Figs 6-7). The *X1-X5* pit crater pipes all extend down to tectonic faults (e.g., Fig. 8). Where the base of pit crater pipes intersect dyke-induced or tectonic faults, they typically do so where the fault planes are relatively steep or sub-vertical (e.g., Figs 6C, 7B, F, 8B, and C). Other pit craters appear to terminate within strata overlying dyke upper tips or fault planes (Figs 4A and 6-8).

Where pit craters display a funnel-like morphology, we measure the height of their inverted cone section and occasionally the deflection of the uppermost stratigraphic reflection within them (i.e. the deflection height) (Fig. 3B). We show inverted cone heights are ~18–245 m, with slopes of 7–51°, and that these values vary across the study area and along individual pit crater chains (Figs 10C, 11A, and B; Supporting Table 1). The corresponding pipe height of these funnel-like pit craters are 27–789 m (Fig. 11A; Supporting Table 1); the heights of pipe-like pit craters are 107–254 m (Table 2). There is no correlation between cone height and total height or pipe height for pit craters within dyke-induced graben (either those above dykes or dyke-induced faults), or for those associated with tectonic normal faults (Figs 11A and B; Supporting Table 1). Deflection heights are ~4–21 m, with slopes <12°, and do not correlate with either total height or cone height (Figs 11C and D; Supporting Table 1).

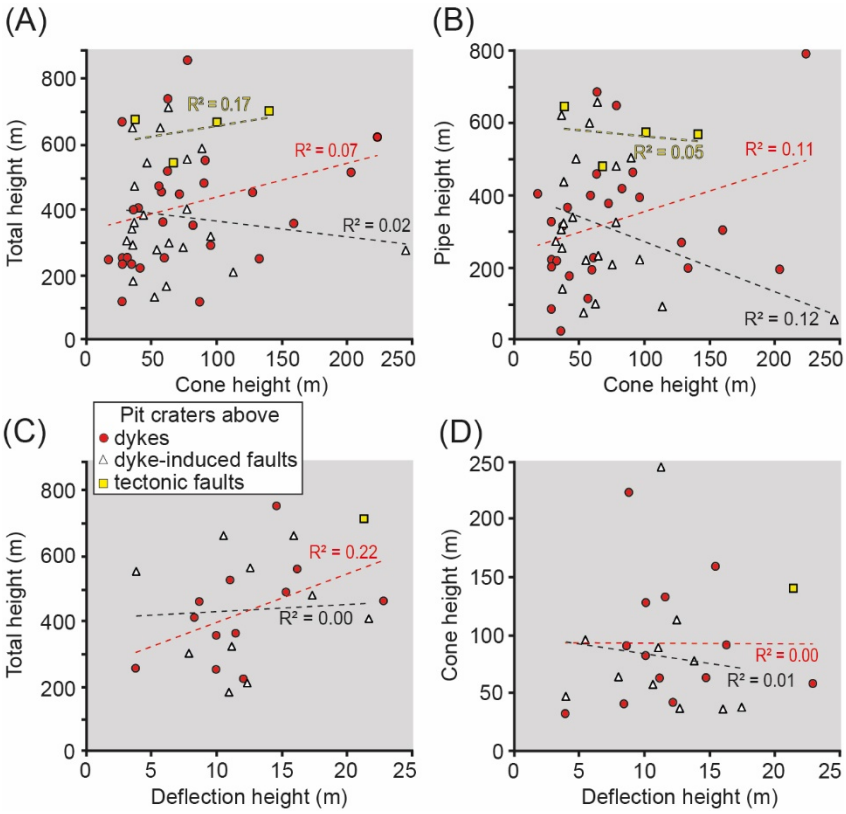

Figure 11: (A-D) Graphs comparing how the total height, pipe height, cone height, and deflection height relate (Supporting Table 1). See Figure 3B for explanation of measured parameters.

1. *Comparative analyses*

With our 3D seismic reflection data we are able to quantitatively assess relationships between the plan-view and cross-sectional geometry of the pit craters. Between pit crater total heights and long axis lengths there is a very weak positive correlation between for those above dykes ($R^2 = 0.17$), no meaningful correlation for pit craters above dyke-induced faults ($R^2 = 0.04$), but a strong positive correlation for those above tectonic faults ($R^2 = 0.71$) (Fig. 12A). Visually similar pit craters recognised elsewhere across the Exmouth Plateau within dyke-induced graben (e.g., Fig. 2D) display a moderate ($R^2 = 0.37$–0.50) positive correlation between total height and long axes (Fig. 12A) (see Velayatham et al., 2019). For all measured pit craters across the Exmouth Plateau there is no correlation (R^2 0.06) between total height and the aspect ratio of their long and short axes (Fig. 12B).

For pit craters above dykes, dyke-induced faults, and tectonic faults, there are positive, power-law correlations between cone height and pit crater long axes

with R^2 values of 0.61, 0.24, and 0.77 respectively (Fig. 12C); these trends are consistent with power-law correlations that define pit crater depth and long axes of craters observed elsewhere on Earth and on other planetary bodies (Fig. 12C) (e.g., Ferrill et al., 2011; Gwinner et al., 2012; Okubo & Martel, 1998; Scott & Wilson, 2002; Whitten & Martin, 2019; Wyrick et al., 2004). There is no correlation ($<R^2 = 0.08$) between deflection height and pit crater long axes (Fig. 12C). Inverted cone volumes (1.34×10^{-4} km^3 to 2.71×10^{-2} km^3), and those of the deflected reflections (7.89×10^{-5} km^3 to 1.62×10^{-3} km^3), are typically smaller than corresponding pipe volumes (1.41×10^{-3} km^3 to 2.79×10^{-1} km^3) (Supporting Table 1).

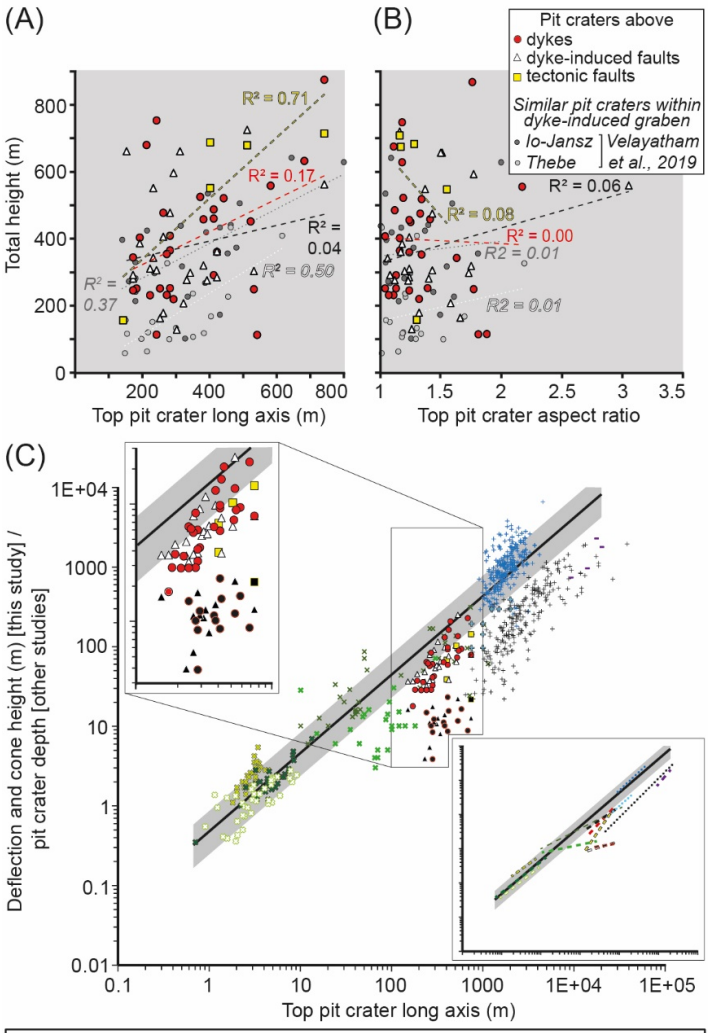

Symbol	Power-law	This study	
●	- - - -	Dyke-related cones	R² = 0.61
△	- - - -	Dyke-induced fault-related cones	R² = 0.24
■	- - - -	Tectonic fault-related cones	R² = 0.77
●	— — —	Dyke-related deflections	R² = 0.03
▲	▫ ▫ ▫ ▫	Dyke-induced fault-related deflections	R² = 0.08
■		Tectonic fault-related deflections	
		Pit craters inferred to be dyke- / fault-related	
-	— — —	Mercury (Gwinner et al., 2012)	R² = 0.80
+	·····	Mars (Kling et al., 2021)	R² = 0.69
+	·····	Mars (Wyrick et al., 2004)	R² = 0.90
+	·····	Mars (Scott and Wilson, 2002)	R² = 0.75
×	- - - -	Earth - Hawaii (Okubo et al., 1998)	R² = 0.64
×	— — —	Earth - Iceland (basalt host; Whitten and Martin, 2019)	R² = 0.45
×	— — —	Earth - Iceland (deltaic host; Whitten and Martin, 2019)	R² = 0.79
○	▫ ▫ ▫ ▫	Earth - Iceland (Ferrill et al., 2011)	R² = 0.49
×	- - - -	Earth - Syria (Frumkin and Naor, 2019)	R² = 0.05
		+ standard error	
	—	Power-law best-fit ($y = 0.44x^{0.9949}$)	R² = 0.94
		- standard error	

Figure 12: (A and B) Plots comparing total height to pit crater long axes (A) and aspect ratio (B) for those located above dykes, dyke-induced faults, and tectonic faults (Supporting Table 1). Data is also shown from two other 3D seismic surveys (Io-Jansz and Thebe) from the Exmouth Plateau, although the exact relation of each pit crater to underlying structure is unknown (Velayatham et al., 2019). (C) Log-log plot of deflection and cone height, one of which is expected equivalent to pit crater depth (e.g., Wyrick et al., 2004), compared to pit crater long axis. Insets show a zoomed-in view of our data and the power-law best-fit trendlines for each plotted dataset. The power-law best-fit trendline shown (black line) with standard errors was calculated from all literature data plotted, with the exception of data from Frumkin and Naor (2019) and Kling et al., (2021) as these pit craters show evidence of post-formation modification.

1. **Discussion**

(a) ***Pit crater structure***

Seismic reflection data provides unique opportunities to image and quantify the entire 3D geometry of pit craters. Like pit craters observed elsewhere on Earth and other planetary bodies, those on the Exmouth Plateau have manifest as the as quasi-circular depressions, which in plan-view are commonly arranged in chains (e.g., Figs 3A and 5). Offset of stratigraphic reflections within most mapped pit craters indicate that these structures form because of spatially restricted host rock subsidence (Figs 3A, 4A, and 6-8). This subsidence is confined to cylindrical pipe-like structures with sub-vertical walls, which towards their tops commonly widen and become inwardly inclined, broadly describing an inverted conical shape (i.e. they are funnel-like) (Figs 3A, 4A, 6-8, and 9C). These observations are consistent with the inferred subsurface geometry of pit craters recognised elsewhere and those modelled using physical or numerical approaches (e.g., Ferrill et al., 2011; Kettermann et al., 2019; Wyrick, 2004; Wyrick et al., 2015). We note that the subsided strata within the studied pit craters typically have a lower amplitude and/or higher variance expression compared to reflections in the flanking host rock (Figs 2D, 3A, 4A, and 6-8). These seismic attribute changes indicate less seismic energy was reflected from within the pit crater, perhaps due to increased scattering of seismic energy from and/or local decreases in acoustic impedance across disrupted beeding (Brown, 2011). Both controls on the amount of seismic energy reflected could be linked to disaggregation of and fluid infiltration through rock during or after subsidence, which are likely common processes during pit crater formation (e.g., Frumkin & Naor, 2019; Halliday, 1998; Velayatham et al., 2018).

1. ***Pit crater age***

Where data resolution allows, some reflections we observe above the pit craters appear thickened (e.g., F13; Fig. 7B) and/or onlap onto the conical walls of pits (e.g., G10a; Fig. 7D). These seismic-stratigraphic relationships imply that the strata represented by these reflections were deposited *within* the pit craters; i.e. the pit craters were surficial features, similar to those recently formed on Earth

(Abelson et al., 2003; Frumkin & Naor, 2019; Okubo & Martel, 1998; Whitten & Martin, 2019). Having established that the shallowest expression of the pit craters likely marks the contemporaneous surface to their formation, we can use biostratigraphic data from local boreholes to estimate their age.

The youngest pit craters (B1-3, D1-2) formed coincident with the Base Cretaceous unconformity at ~148 Ma (Figs 6B and D). Critically, the uppermost expression of pit craters across the study area and along individual chains (e.g., A–C, E, F, H, and I) often occur at different stratigraphic horizons above the ~165 Ma Top Athol Formation (Figs 6-7, 10A, and B). These observations indicate the pit craters developed periodically during deposition of the marine Dingo Claystone in the Late Jurassic (Figs 2B, 6-7, 10A, and B). For some pit crater chains, specifically D1-D2 and G1-G13, the tops of individual pits occur along the same stratigraphic horizon suggesting they formed near-synchronously (Figs 6D, 7B, 10A, and B).

Our inferred Late Jurassic timing of pit crater formation is consistent with seismic-stratigraphic constraints on the age of the Exmouth Dyke Swarm and associated dyke-induced faults (Fig. 2) (Magee & Jackson, 2020a). As most pit craters are found below the ~148 Ma Base Cretaceous unconformity, but all dyke-induced faults offset this horizon, it seems likely that pit crater formation generally ceased before dyking and associated faulting ended (Figs 4B and C) (Magee & Jackson, 2020a). Overall, we suggest that the oldest pit craters occurred during the early development of the Exmouth Dyke Swarm and associated dyke-induced faults, with dyking and fault growth occurring (periodically) up until ~148 Ma.

1. ***Pit crater origin***

Numerous processes involving underlying cavity collapse or the volumetric reduction of a subsurface body have previously been proposed to generate space for overburden subsidence and pit crater formation (Fig. 1B) (see Wyrick et al., 2004 and references therein). We identify no clear cavity-like structures at the pit crater bases (Figs 3A, 4A, and 6-8), and disregard the following possible mechanisms of pit crater formation: (i) carbonate or salt dissolution (Fig. 1C [i]) (Abelson et al., 2003; Spencer & Fanale, 1990), because the Triassic-to-Late Jurassic strata hosting the pit craters contains no (or only very little) carbonate rocks and no salt (Fig. 2B) (e.g., Exon et al., 1992; Stagg et al., 2004; Tindale et al., 1998); (ii) evacuation of lava tubes (see Sauro et al., 2020 and references therein), as there is no evidence for high-amplitude, sinuous, strata-concordant reflections that could be attributed to lava flows or tubes (Figs 3A, 4A, and 7-9) (e.g., Sun et al., 2019); and (iii) magma migration from a reservoir (e.g., Mège et al., 2003; Poppe et al., 2015), as there is no evidence for underlying tabular igneous intrusions (e.g., sills or laccoliths) (Figs 3A, 4A, and 6-8), which are typically expressed as high-amplitude, positive, sub-horizontal-to-inclined reflections (e.g., Planke et al., 2005). Instead, we find that some pit craters directly emanate from either the upper tips of dykes ($n = 6$), dyke-induced fault planes ($n = 6$), or tectonic faults ($n = 5$) (Figs 6-8). Where we observe pit crater bases

situated some distance above dyke upper tips or dyke-induced faults (Figs 6-8), we consider it plausible that seismically unresolved or obscured portions of their pipes extend down to these underlying structures. Our observations allow for the generation of these pit craters in response to the opening of vertical tensile fractures (Fig. 1C [iv]) (e.g., Ferrill et al., 2011; Smart et al., 2011; Tanaka & Golombek, 1989), which cannot be imaged in seismic reflection data.

The generation of pit craters linked to dyke tips may be driven by (Fig. 1C [vi]): (i) a volume reduction of the dyke itself, perhaps as magma pressure wanes or volatiles escape (e.g., Patterson et al., 2016; Scott & Wilson, 2002); (ii) escape of heated pore fluids from the tip-adjacent host rock and subsequent porosity collapse (e.g., Schofield et al., 2010); (iii) phreatic eruption (Hughes et al., 2018); and/or (iv) subsidence of material into a tensile fracture that opens above an inflating and widening dyke (similar to Fig. 1C [iv]) (e.g., Ferrill et al., 2011; Smart et al., 2011; Tanaka & Golombek, 1989). We show that within some pit crater chains, the tops of individual pits located directly above dykes occur at deeper stratigraphic levels and are thus older towards the north of our study area (e.g., above dykes A and I; Figs 10A and B). These occurrences of pit crater tops at multiple stratigraphic levels above single dykes indicate that periods of sediment deposition separated pit crater formation (Fig. 13); this interpretation is consistent with fault displacement data, which reveals the dyke-induced faults likely grew incrementally via segment linkage (Magee & Jackson, 2020b). As the dykes are part of a radial dyke swarm that intruded laterally northwards (Fig. 2A) (Magee & Jackson, 2020a), the apparent southwards decrease in age of the pit craters suggests that they did not develop above propagating dyke tips (Fig. 13A). Dyke thickness also decreases gradually northwards (Magee & Jackson, 2020a), so it seems unlikely that pit crater formation occurred in response to dyke widening and tensile fracturing of the overburden; i.e. we should expect areas where dyke width is greatest to generate pit craters first (Fig. 13B). We suggest that the possible southwards decrease in age of pit craters directly above dykes may have occurred due to localised volume reductions of the intrusion as driving pressure periodically waned (Fig. 13C). Such volume reductions could have been driven by magma backflow and retreat (e.g., Philpotts & Asher, 1994; Philpotts & Philpotts, 2007), or solidification and contraction (e.g., Caricchi et al., 2014). Cyclical periods of intrusion and driving pressure waning could create complex trends of pit craters along individual dykes.

Pit craters linked to faults observed elsewhere on the Exmouth Plateau have been attributed to local reduction of confining pressure and fluid escape from an overpressured horizon in the Mungaroo Formation during faulting (e.g., Fig. 1C [ii]) (Velayatham et al., 2019; Velayatham et al., 2018). We show that some pit craters link to steep-to-sub-vertical fault portions, suggesting their formation may also be associated with the collapse of dilatational jogs (Figs 1C [v], 7B, 8B, and C) (e.g., Ferrill & Morris, 2003; Ferrill et al., 2011; Ketterman et al., 2015; Kettermann et al., 2019; Smart et al., 2011; Von Hagke et al., 2019).

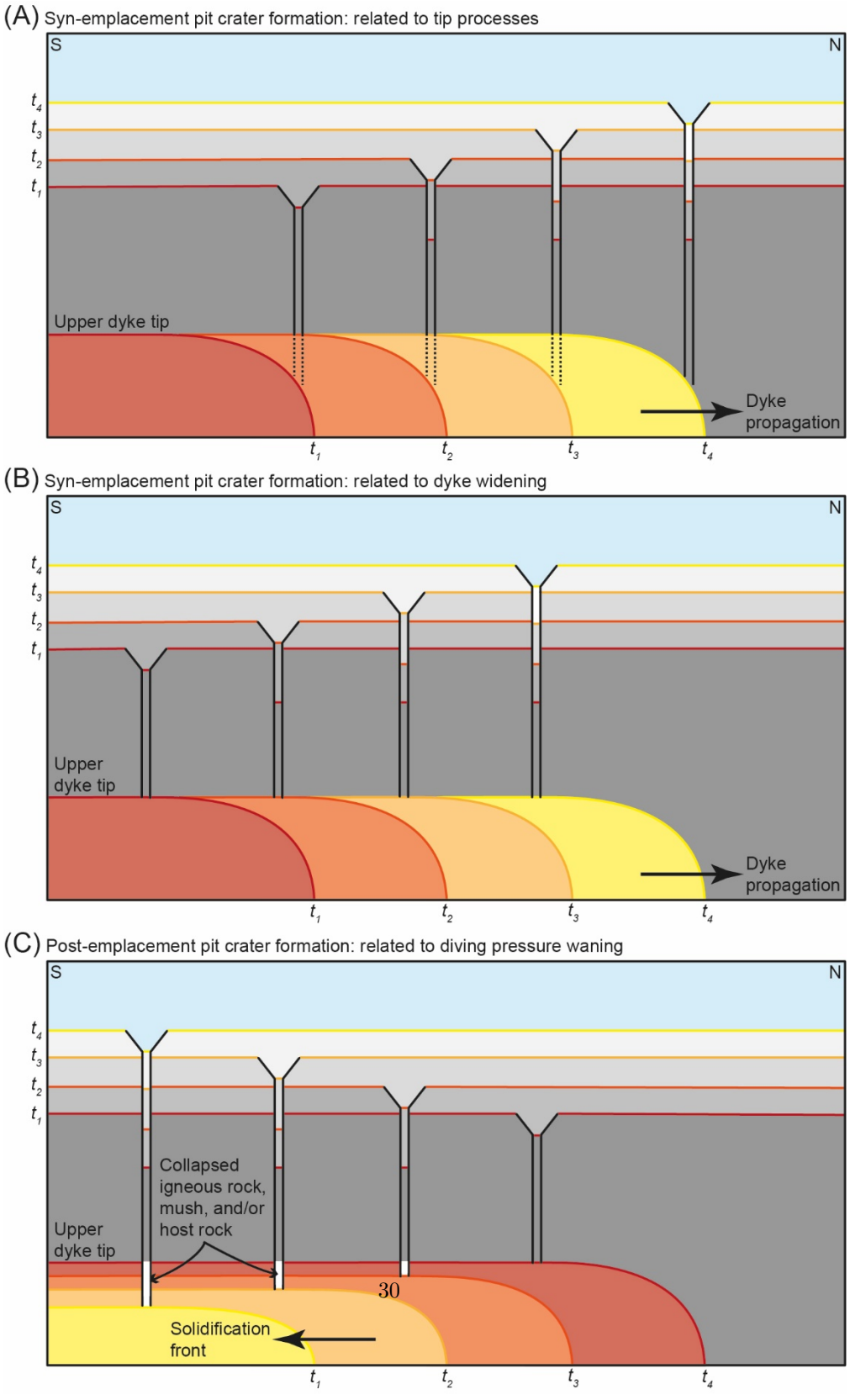
(A) Syn-emplacement pit crater formation: related to tip processes
S
N
t_4
t_3
t_2
t_1
Upper dyke tip
Dyke propagation
t_1
t_2
t_3
t_4
(B) Syn-emplacement pit crater formation: related to dyke widening
S
N
t_4
t_3
t_2
t_1
Upper dyke tip
Dyke propagation
t_1
t_2
t_3
t_4
(C) Post-emplacement pit crater formation: related to diving pressure waning
S
N
t_4
t_3
t_2
t_1
Collapsed igneous rock, mush, and/or host rock
Upper dyke tip
Solidification front
t_1
t_2
t_3
t_4

Figure 13: Schematic models describing how pit crater may be expected to relate to different dyke processes. (A) Pit crater formation is linked to lateral propagation of the dyke tip, perhaps driven by fluid escape into and/or collapse of the tip cavity, or eruption (Hughes et al., 2018; Scott & Wilson, 2002). Pit crater age decreases further from the dyke source. (B) Pit crater formation occurs as the dyke widens behind the propagating tip, perhaps linked to tensile fracturing (Tanaka & Golombek, 1989) as dyke widening induces extension of the overlying rock, fluid escape into and/or collapse of the tip cavity, or eruption (Hughes et al., 2018; Scott & Wilson, 2002). Pit crater age decreases further from the dyke source. (C) Pit crater formation occurs as the magma driving pressure or supply wanes, causing magma to flow backwards (e.g., Philpotts & Asher, 1994) and/or solidify and contract (i.e. a volume reduction) (e.g., Caricchi et al., 2014). Pit crater age increases further from the dyke source.

1. ***Pit crater depth***

Where pit craters are observed on the surface of Earth and other planetary bodies, we are typically restricted to measuring their plan-view geometry (e.g., axial dimensions) and crater depth (e.g., Whitten & Martin, 2019; Wyrick et al., 2004). Numerous studies have demonstrated that pit crater depths of most populations likely related to dyke or fault activity, positively correlates with their long axis length via power-law relations (R^2 = 0.45–0.90) with similar slopes (Fig. 12C) (e.g., Ferrill et al., 2011; Gwinner et al., 2012; Kling et al., 2021; Okubo & Martel, 1998; Scott & Wilson, 2002; Whitten & Martin, 2019; Wyrick et al., 2004); all these data can be fit by a power-law relationship (R^2 = 0.94; Fig. 12C). Some pit craters within the Golan volcanic province, southern Levant, are an exception to this power-law trend as they show no correlation between pit crater depth and long axis, which has been attributed to recent modification by erosion and sedimentation (R^2 = 0.05; Fig. 12C) (Frumkin & Naor, 2019).

From our seismic reflection data, we can measure pit crater morphometric properties, but we first need to establish whether the height of the inverted cone sections we describe, or that of the deflected reflections they contain, are equivalent to pit crater depth (Fig. 3B). For pit craters above dykes, dyke-induced faults, and tectonic faults, we find that cone height and pit long axis length positively correlate (R^2 = 0.61, 0.24, and 0.77, respectively) and overlaps with data from many other locations (Fig. 12C). However, there is no meaningful correlation (R^2 = <0.1) for deflection height and pit long axis length (Fig. 12C). The deflection height measurements also fall an order of magnitude below the power-law trend fit to the compiled published pit crater data; this is similar to pit craters in the Golan volcanic province and Noctis Labyrinthus (Mars), both of which display evidence for post-formation modification of their initial geometries (Fig. 12C) (Frumkin & Naor, 2019; Kling et al., 2021). Based on these comparisons, we suggest that the walls of the inverted cone sections represent the original pit crater morphology (Fig. 14). The reflections within the inverted cone sections are interpreted to correspond to material that infilled the

pit crater (Fig. 14). Our results support recent suggestions that relationships between pit crater depths and long axis lengths may provide some indication as to whether post-formation erosional and infilling processes have modified pit geometry (Figs 12C and 14) (Frumkin & Naor, 2019; Kling et al., 2021).

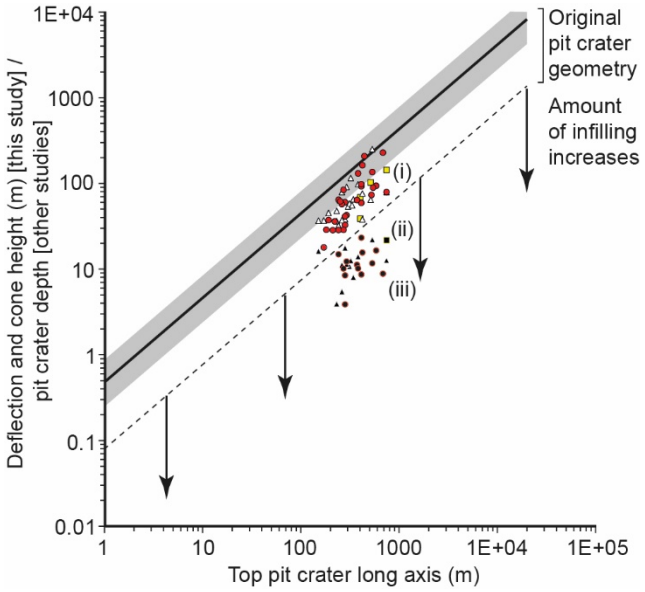

Figure 14: Simplified version of Figure 12C showing our deflection and cone height data plotted against pit crater long axis, coupled with the power-law trend of all literature data used. We define an arbitrary boundary between areas where original pit crater geometries are likely preserved and those where infilling may modify apparent pit crater depths. Inset: sketches showing how infilling may modify pit crater depths.

1. ***Can we relate the surface expression of pit craters to subsurface structures and processes?***

The surface expression of pit craters observed on Earth and other planetary bodies has been used to infer how they formed and establish characteristics of subsurface geology (e.g., regolith depth) (e.g., Kling et al., 2021; Korteniemi et al., 2010; Martin et al., 2017; Mège & Masson, 1997; Smart et al., 2011; Whitten & Martin, 2019). For example, we may expect pit craters long axes, like that of volcanic vents, to align parallel to underlying dykes as they form within the same stress field (Bonini & Mazzarini, 2010; Magee et al., 2016; Paulsen & Wilson, 2010). Because we have established that pit crater formation was related to either be dyking or faulting, and because we can image these features in 3D, we can examine pit crater morphologies to see if magmatic and tectonic origins can be distinguished. Aside from cone height (pit crater depth) and long axis lengths, our data demonstrates that most pit crater properties are only weakly positively correlated or that there is no correlation at all (Figs 11

and 12). Critically, there are no significant differences in sizes of pit craters developed above dykes, dyke-induced faults, or tectonic faults (Figs 11 and 12). The pit craters we analyse also show no preferred long axis orientation, even those seemingly related to contemporaneous dykes and dyke-induced faults that are clearly aligned ~N-S (Fig. 12B). The disparity in dyke and dyke-induced fault orientation relative to the elongation of the pit craters implies formation of the latter was not sensitive to the prevailing stress field, perhaps because they formed in unconsolidated wet sediments. Overall, our data suggest that pit craters related to dyking, dyke-induced faulting, or tectonic faulting cannot be easily distinguished based on their surficial size and orientation (Figs 9A, C, and 12).

In addition to relating surface expression to pit crater formation, pit crater depths have been used as a proxy for regolith thickness on other planetary bodies (e.g., Whitten & Martin, 2019; Wyrick et al., 2004). This use of pit crater depth follows the inference that drainage of loose, unconsolidated material into an underlying cavity instigates development of an inverted cone section controlled by the host materials angle of repose (e.g., Whitten & Martin, 2019; Wyrick et al., 2004). Our pit craters formed during deposition of the marine Dingo Claystone (Tindale et al., 1998), so we assume their contemporaneous shallow sub-seabed material was unconsolidated and wet. Although the presence of pore fluids may alter the behaviour of host sediment relative to dry regolith on other planetary bodies, it seems reasonable to expect both materials to respond similarly to localised subsidence; i.e. they should drain into underlying pipes. However, we show that cone height (i.e. pit crater depth) varies non-systematically across the study area, including along individual chains, with adjacent pit craters of the same age often displaying different cone heights (Figs 6-8 and 10). Furthermore, some pit craters seemingly have no seismically resolved inverted cone section and appear simply to have a pipe-like geometry (Figs 6-8). Assuming that the transition from unconsolidated wet sediment to lithified rock (i.e. perhaps equivalent to a regolith-rock transition) occurred at a relatively constant depth across the study area, the observed variation in pit crater cone heights and their local absence suggest the changing rheology of the host material did not primarily control pit crater geometry (cf. Whitten & Martin, 2019; Wyrick et al., 2004).

1. Conclusions

Here, we use seismic reflection data from offshore NW Australia to image the entire 3D geometry of pit craters and underlying magmatic and tectonic structures. Our work demonstrates that pit craters link at depth to dykes and steep fault segments, confirming pit crater formation can occur in response to magmatic processes and dilatational faulting. We also show that pit crater depths strongly correlate with their long axis lengths, consistent with observations of pit craters elsewhere on Earth and other planetary bodies; deviation of pit crater populations from the power-law trend that defines these may be an indicator that pit craters have been infilled and/or modified. Our results suggest that we

should be cautious when interpreting the origin of pit craters on other planetary bodies because: (i) the distribution and size of pit craters may not be diagnostic of the potential dyking and/or faulting processes driving their formation; and (ii) pit crater size may not simply relate to the mechanical properties of the host material (e.g., regolith) or their driving mechanism. Overall, our work shows that reflection seismology is a powerful tool for subsurface exploration on other worlds, as it allows us to examine the 3D structure of features on Earth thought analogous to those recognised on the surfaces of other planetary bodies.

Acknowledgements

We are grateful to Geoscience Australia for making the data we use freely available, and to Schlumberger for providing use of Petrel seismic interpretation software. Funding for this work was acquired by Magee as part of a NERC Independent Research Fellowship (NE\R014086\1) and a Royal Society International Exchange Grant (IES\R3\193221).

Data availability statement

Seismic reflection and well data used in this study are freely available from the Geoscience Australia NOPIMS (https://nopims.dmp.wa.gov.au/nopims) data repository. The NOPIMS data access centre allows 'Wells' (i.e. for this study Chandon 1, Chandon 2, Chandon 3, Mercury 1, and Yellowglen 1) and 'Surveys' (i.e. for this study the Chandon 3D MSS seismic reflection survey) from offshore Australia to be searched for. From these search results, well data can be downloaded by highlighting the correct well and using 'view details for selected rows'; due to the file size of seismic reflection segy data like the Chandon 3D MSS, few can be downloaded but all can be added to a basket and freely requested from Geoscience Australia. All measurements and calculations acquired during this research are provided in Supporting Table 1 and copies will be hosted in the National Geoscience Data Centre of the British Geological Survey (https://www.bgs.ac.uk/geological-data/national-geoscience-data-centre/) and Figshare (https://figshare.com/).

References

Abelson, M., Baer, G., Shtivelman, V., Wachs, D., Raz, E., Crouvi, O., et al. (2003). Collapse-sinkholes and radar interferometry reveal neotectonics concealed within the Dead Sea basin. *Geophysical Research Letters, 30*(10), 1545. Bilal, A., McClay, K., & Scarselli, N. (2018). Fault-scarp degradation in the central Exmouth Plateau, North West Shelf, Australia. *Geological Society, London, Special Publications, 476*, SP476. 411. Black, M., McCormack, K., Elders, C., & Robertson, D. (2017). Extensional fault evolution within the Exmouth Sub-basin, North West Shelf, Australia. *Marine and Petroleum Geology, 85*, 301-315. Bonini, M., & Mazzarini, F. (2010). Mud volcanoes as potential indicators of regional stress and pressurized layer depth. *Tectonophysics, 494*(1), 32-47. Brown, A. R. (2011). *Interpretation of three-dimensional seismic data* (6th ed. Vol. 42). Oklahoma, USA: AAPG and SEG.Caricchi, L., Biggs, J., Annen, C., & Ebmeier, S. (2014). The influence of cooling, crystallisation and

re-melting on the interpretation of geodetic signals in volcanic systems. *Earth and Planetary Science Letters, 388*, 166-174. Chopra, S., & Marfurt, K. J. (2005). Seismic attributes—A historical perspective. *Geophysics, 70*(5), 3SO-28SO. Direen, N. G., Stagg, H. M. J., Symonds, P. A., & Colwell, J. B. (2008). Architecture of volcanic rifted margins: new insights from the Exmouth – Gascoyne margin, Western Australia. *Australian Journal of Earth Sciences, 55*(3), 341-363. Driscoll, N. W., & Karner, G. D. (1998). Lower crustal extension across the Northern Carnarvon basin, Australia: Evidence for an eastward dipping detachment. *Journal of Geophysical Research: Solid Earth (1978–2012), 103*(B3), 4975-4991. Exon, N., Haq, B., & Von Rad, U. (1992). *Exmouth Plateau revisited: scientific drilling and geological framework.* Paper presented at the Proceedings of the Ocean Drilling Program, Scientific Results.Ferrill, D. A., & Morris, A. P. (2003). Dilational normal faults. *Journal of Structural Geology, 25*(2), 183-196. Ferrill, D. A., Wyrick, D. Y., Morris, A. P., Sims, D. W., & Franklin, N. M. (2004). Dilational fault slip and pit chain formation on Mars. *GSA Today, 14*(10), 4. Ferrill, D. A., Wyrick, D. Y., & Smart, K. J. (2011). Coseismic, dilational-fault and extension-fracture related pit chain formation in Iceland: Analog for pit chains on Mars. *Lithosphere, 3*(2), 133-142. Frumkin, A., & Naor, R. (2019). Formation and modification of pit craters–example from the Golan volcanic plateau, southern Levant. *Zeitschrift für Geomorphologie, 62*(3), 163-181. Gartrell, A., Torres, J., Dixon, M., & Keep, M. (2016). Mesozoic rift onset and its impact on the sequence stratigraphic architecture of the Northern Carnarvon Basin. *The APPEA Journal, 56*(1), 143-158. Gwinner, K., Head, J., Oberst, J., Gillis-Davis, J., Xiao, Z., Strom, R., et al. (2012). Morphology of pit craters on Mercury from stereo-derived topography and implications for pit crater formation. (1659), 1991. Halliday, W. R. (1998). " Pit Craters", lava tubes, and open vertical volcanic conduits in Hawaii: a problem in terminology. *International Journal of Speleology, 27*(1), 113-124. Hocking, R. (1992). Jurassic deposition in the southern and central North West Shelf. *Western Australia: Geological Survey Western Australia Record, 199217*. Hocking, R. M., Moors, H. T., & Van de Graaff, W. E. (1987). *Geology of the carnarvon basin, Western Australia* (Vol. 133): State Print. Division.Horstman, K., & Melosh, H. (1989). Drainage pits in cohesionless materials: Implications for the surface of Phobos. *Journal of Geophysical Research: Solid Earth, 94*(B9), 12433-12441. Hughes, S. S., Nawotniak, S. E. K., Sears, D. W., Borg, C., Garry, W. B., Christiansen, E. H., et al. (2018). Phreatic explosions during basaltic fissure eruptions: Kings Bowl lava field, Snake River Plain, USA. *Journal of Volcanology and Geothermal Research, 351*, 89-104. Ketterman, M., Grützner, C., Urai, J., Reicherter, K., & Mertens, J. (2015). Evolution of a highly dilatant fault zone in the grabens of Canyonlands National Park, Utah, USA–integrating fieldwork, ground-penetrating radar and airborne imagery analysis. *Solid Earth, 6*, 839-855. Kettermann, M., Weismüller, C., von Hagke, C., Reicherter, K., & Urai, J. L. (2019). Large near-surface block rotations at normal faults of the Iceland rift: Evolution of tectonic caves and dilatancy. *Geology, 47*(8), 781-785. Kling, C. L., Byrne, P. K., Atkins, R. M., & Wegmann, K. W. (2021). Tectonic Deformation and Volatile Loss in the Formation of Noctis Labyrinthus,

Mars. *Journal of Geophysical Research: Planets*, e2020JE006555. Korteniemi, J., Raitala, J., Aittola, M., Ivanov, M. A., Kostama, V.-P., Öhman, T., & Hiesinger, H. (2010). Dike indicators in the Hadriaca Patera–Promethei Terra region, Mars. *Earth and Planetary Science Letters, 294*(3), 466-478. Longley, I., Buessenschuett, C., Clydsdale, L., Cubitt, C., Davis, R., Johnson, M., et al. (2002). The North West Shelf of Australia–a Woodside perspective. *The sedimentary basins of Western Australia, 3*, 27-88. Magee, C., Duffy, O. B., Purnell, K., Bell, R. E., Jackson, C. A. L., & Reeve, M. T. (2016). Fault-controlled fluid flow inferred from hydrothermal vents imaged in 3D seismic reflection data, offshore NW Australia. *Basin Research, 28*(3), 299-318. Magee, C., Ernst, R. E., Muirhead, J., Phillips, T., & Jackson, C. A.-L. (2019). Magma Transport Pathways in Large Igneous Provinces: Lessons from Combining Field Observations and Seismic Reflection Data. In R. Srivastava, R. Ernst, & P. Peng (Eds.), *Dyke Swarms of the World: A Modern Perspective* (pp. 45-85): Springer.Magee, C., & Jackson, C.-L. (2020a). Seismic reflection data reveal the 3D structure of the newly discovered Exmouth Dyke Swarm, offshore NW Australia. *Solid Earth, 11*(2), 576-606. Magee, C., & Jackson, C. A.-L. (2020b). Can we relate the surface expression of dike-induced normal faults to subsurface dike geometry? *Geology, 49*. Marfurt, K. J., & Alves, T. M. (2015). Pitfalls and limitations in seismic attribute interpretation of tectonic features. *Interpretation, 3*(1), SB5-SB15. Marshall, N., & Lang, S. (2013). *A new sequence stratigraphic framework for the North West Shelf, Australia.* Paper presented at the The Sedimentary Basins of Western Australia 4: Proceedings PESA Symposium. Perth.Martin, E. S., Kattenhorn, S. A., Collins, G. C., Michaud, R. L., Pappalardo, R. T., & Wyrick, D. Y. (2017). Pit chains on Enceladus signal the recent tectonic dissection of the ancient cratered terrains. *Icarus, 294*, 209-217. Mège, D., Cook, A. C., Garel, E., Lagabrielle, Y., & Cormier, M. H. (2003). Volcanic rifting at Martian grabens. *Journal of Geophysical Research: Planets, 108*(E5). Mège, D., & Masson, P. (1996). A plume tectonics model for the Tharsis province, Mars. *Planetary and Space Science44*(12), 1499-1546. Mège, D., & Masson, P. (1997). *Graben formation and dike emplacement on Earth and other planets.* Paper presented at the Lunar and Planetary Science Conference.Muirhead, J. D., Kattenhorn, S. A., & Le Corvec, N. (2015). Varying styles of magmatic strain accommodation across the East African Rift. *Geochemistry, Geophysics, Geosystems*. Okubo, C. H., & Martel, S. J. (1998). Pit crater formation on Kilauea volcano, Hawaii. *Journal of Volcanology and Geothermal Research, 86*(1), 1-18. Paganoni, M., King, J. J., Foschi, M., Mellor-Jones, K., & Cartwright, J. A. (2019). A natural gas hydrate system on the Exmouth Plateau (NW shelf of Australia) sourced by thermogenic hydrocarbon leakage. *Marine and Petroleum Geology, 99*, 370-392. Partington, M., Aurisch, K., Clark, W., Newlands, I., Phelps, S., Senycia, P., et al. (2003). The hydrocarbon potential of exploration permits WA-299-P and WA-300-P, Carnarvon Basin: a case study. *The APPEA Journal, 43*(1), 339-361. Patterson, C. W., Ernst, R. E., & Samson, C. (2016). Pit Chains Belonging to Radiating Graben-Fissure Systems on Venus: Model for Formation during Lateral Dyke Injection. *Acta Geologica Sinica (English Edition), 90*(s1), 143-144. Paulsen, T. S., & Wilson, T. J. (2010). New crite-

ria for systematic mapping and reliability assessment of monogenetic volcanic vent alignments and elongate volcanic vents for crustal stress analyses. *Tectonophysics, 482*(1), 16-28. Paumard, V., Bourget, J., Payenberg, T., Ainsworth, R. B., George, A. D., Lang, S., et al. (2018). Controls on shelf-margin architecture and sediment partitioning during a syn-rift to post-rift transition: Insights from the Barrow Group (Northern Carnarvon Basin, North West Shelf, Australia). *Earth-Science Reviews, 177*, 643-677. Philpotts, A., & Asher, P. (1994). Magmatic flow-direction indicators in a giant diabase feeder dike, Connecticut. *Geology, 22*(4), 363-366. Philpotts, A. R., & Philpotts, D. E. (2007). Upward and downward flow in a camptonite dike as recorded by deformed vesicles and the anisotropy of magnetic susceptibility (AMS). *Journal of Volcanology and Geothermal Research, 161*(1-2), 81-94. Planke, S., Rasmussen, T., Rey, S. S., & Myklebust, R. (2005). Seismic characteristics and distribution of volcanic intrusions and hydrothermal vent complexes in the Vøring and Møre basins. In A. G. Doré (Ed.), *Petroleum Geology: North-West Europe and Global Perspectives - Proceddings of the 6th Petroleum Geology Conference* (pp. 833-844): Geological Society, London.Poppe, S., Holohan, E. P., Pauwels, E., Cnudde, V., & Kervyn, M. (2015). Sinkholes, pit craters, and small calderas: Analog models of depletion-induced collapse analyzed by computed X-ray microtomography. *Geological Society of America Bulletin, 127*(1-2), 281-296. Reeve, M. T., Jackson, C. A. L., Bell, R. E., Magee, C., & Bastow, I. D. (2016). The stratigraphic record of prebreakup geodynamics: Evidence from the Barrow Delta, offshore Northwest Australia. *Tectonics, 35*(8), 1935-1968. Reeve, M. T., Magee, C., Bastow, I. D., McDermott, C., Jackson, C. A.-L., Bell, R. E., & Prytulak, J. (2021). Nature of the Cuvier Abyssal Plain crust, offshore NW Australia. *Journal of the Geological Society*. Robb, M. S., Taylor, B., & Goodliffe, A. M. (2005). Re-examination of the magnetic lineations of the Gascoyne and Cuvier Abyssal Plains, off NW Australia. *Geophysical Journal International, 163*(1), 42-55. Sauro, F., Pozzobon, R., Massironi, M., De Berardinis, P., Santagata, T., & De Waele, J. (2020). Lava tubes on Earth, Moon and Mars: A review on their size and morphology revealed by comparative planetology. *Earth-Science Reviews, 209*(103288). Schofield, N., Stevenson, C., & Reston, T. (2010). Magma fingers and host rock fluidization in the emplacement of sills. *Geology, 38*(1), 63-66. Scott, E. D., & Wilson, L. (2002). Plinian eruptions and passive collapse events as mechanisms of formation for Martian pit chain craters. *Journal of Geophysical Research: Planets, 107*(E4), 4-1-4-11. Smart, K. J., Wyrick, D. Y., & Ferrill, D. A. (2011). Discrete element modeling of Martian pit crater formation in response to extensional fracturing and dilational normal faulting. *Journal of Geophysical Research: Planets, 116*(E4). Spencer, J. R., & Fanale, F. P. (1990). New models for the origin of Valles Marineris closed depressions. *Journal of Geophysical Research: Solid Earth, 95*(B9), 14301-14313. Stagg, H., Alcock, M., Bernardel, G., Moore, A., Symonds, P., & Exon, N. (2004). *Geological framework of the outer Exmouth Plateau and adjacent ocean basins*: Geoscience Australia.Stagg, H., & Colwell, J. (1994). *The structural foundations of the Northern Carnarvon Basin.* Paper presented at the The sedimentary basins of Western Australia: Proceedings of Petroleum Exploration Society of Aus-

tralia Symposium, Perth.Sun, Q., Jackson, C. A.-L., Magee, C., Mitchell, S. J., & Xie, X. (2019). Extrusion dynamics of deepwater volcanoes revealed by 3-D seismic data. *Solid Earth, 10*(4), 1269-1282. Tanaka, K., & Golombek, M. (1989). *Martian tension fractures and the formation of grabens and collapse features at Valles Marineris.* Paper presented at the Lunar and Planetary Science Conference Proceedings.Tindale, K., Newell, N., Keall, J., & Smith, N. (1998). *Structural evolution and charge history of the Exmouth Sub-basin, northern Carnarvon Basin, Western Australia.* Paper presented at the The Sedimentary Basins of Western Australia 2: Proc. of Petroleum Society Australia Symposium, Perth, WA.Velayatham, T., Holford, S., Bunch, M., King, R., & Magee, C. (2019). *3D Seismic Analysis of Ancient Subsurface Fluid Flow in the Exmouth Plateau, Offshore Western Australia.* Paper presented at the West Australian Basins Symposium, Perth, Western Australia.Velayatham, T., Holford, S. P., & Bunch, M. A. (2018). Ancient fluid flow recorded by remarkably long, buried pockmark trains observed in 3D seismic data, Exmouth Plateau, Northern Carnarvon basin. *Marine and Petroleum Geology, 95*, 303-313. Von Hagke, C., Kettermann, M., Bitsch, N., Bücken, D., Weismüller, C., & Urai, J. L. (2019). The effect of obliquity of slip in normal faults on distribution of open fractures. *Frontiers in Earth Science, 7*(18). Wall, M., Cartwright, J., Davies, R., & McGrandle, A. (2010). 3D seismic imaging of a Tertiary Dyke Swarm in the Southern North Sea, UK. *Basin Research, 22*(2), 181-194. Whitten, J. L., & Martin, E. S. (2019). Icelandic pit chains as planetary analogs: Using morphologic measurements of pit chains to determine regolith thickness. *Journal of Geophysical Research: Planets, 124*(11), 2983-2999. Wyrick, D. (2004). Distribution, morphology, and origins of Martian pit crater chains. *Journal of Geophysical Research, 109*(E6). Wyrick, D., Ferrill, D. A., Morris, A. P., Colton, S. L., & Sims, D. W. (2004). Distribution, morphology, and origins of Martian pit crater chains. *Journal of Geophysical Research, 109*(E6), E06005. Wyrick, D. Y., Morris, A. P., Todt, M. K., & Watson-Morris, M. J. (2015). Physical analogue modelling of Martian dyke-induced deformation. *Geological Society, London, Special Publications, 401*(1), 395-403. Yang, X.-M., & Elders, C. (2016). The Mesozoic structural evolution of the Gorgon Platform, North Carnarvon Basin, Australia. *Australian Journal of Earth Sciences, 63*(6), 755-770.